2018

On The Scattering Of Topographically Modified Semidiurnal Kelvin Waves Into Internal Waves

Tianyi Zhang
University of South Carolina

ON THE SCATTERING OF TOPOGRAPHICALLY MODIFIED SEMIDIURNAL KELVIN WAVES INTO INTERNAL WAVES

by

Tianyi Zhang

Bachelor of Science
University of Pittsburgh, 2014

Bachelor of Science
Sichuan University, 2014

Submitted in Partial Fulfillment of the Requirements

For the Degree of Doctor of Philosophy in

Marine Science

College of Arts and Sciences

University of South Carolina

2018

Accepted by:

Alexander Yankovsky, Major Professor

George Voulgaris, Committee Member

Subrahmanyam Bulusu, Committee Member

Maarten Buijsman, Committee Member

Cheryl L. Addy, Vice Provost and Dean of the Graduate School

ACKNOWLEDGEMENTS

This dissertation would not have been possible without the advice and support of many. First and foremost, I would like to thank my advisor Dr. Alexander Yankovsky who taught me, advised me, and supported my works from the beginning to the final stages of my graduate study. Dr. Yankovsky is not only a great advisor whose inspiration and guidance has been constant throughout my academic career, he is also my mentor in life, helping me overcome hardships and stay in optimum as a graduate student. I will always be grateful for his support and encouragement.

I would like to express my appreciation to my committee members. My warmest thanks to Dr. George Voulgaris for his insightful advice and criticisms and for the time series analysis skills I have learnt from him; to Dr. Subrahmanyam Bulusu for his career advice and for all he taught me about physical oceanography; to Dr. Maarten Buijsman for the careful criticisms and very constructive comments and for the knowledge of global models.

I would also like to thank my friends and colleagues. I spent a wonderful time working with Dr. Yosuke Igeta during his visit. Many thanks to my lab mates: Douglas Cahl, Alejandro Frank, Nahid Hasan, Conor Ofsthun, Zaid Rahman, and Xiaodong Wu, and to Jaehoon Choe for always helping me out with our lab devices.

Finally, I would like to thank my family. My journey in science would not have been imaginable without the support from my parents. And a special thanks to my love Runhua Zhao, who has always been my lighthouse of encouragement.

ABSTRACT

Semidiurnal tides propagate along continental shelves as a Kelvin wave mode. On wide continental shelves, the shelf topography modifies the Kelvin wave mode into a hybrid Kelvin-edge wave (HKEW), with features of a zero mode edge wave. Its free surface structure and alongshore energy flux concentrate on the shelf, and are sensitive to changes in the shelf width. When a propagating HKEW encounters an alongshore change of shelf width, the adjustment of wave structures results in the scattering of the incident wave into other wave modes, including barotropic and baroclinic Poincaré waves radiating offshore. These dynamics are studied using the Regional Ocean Modeling System (ROMS) under barotropic and stratified conditions. The model consists of two alongshore-uniform continental shelves of different widths adjoined through a transition zone. The continental shelf and slope are adjacent to an ocean of a constant depth. The barotropic model shows that when the shelf width changes, the barotropic alongshore energy fluxes diverge on the shelf. This divergence of alongshore energy fluxes leads to a cross-isobath energy flux. The stratified model shows that when the cross-isobath energy flux is offshore, the incident energy scatters into barotropic wave modes. When the energy flux is onshore, more than 10% of the incident energy can scatter into internal wave modes under favorable conditions. This internal tide generation mechanism is relevant to the coastal ocean with strong semidiurnal tides and wide continental shelves, such as the Celtic Sea and the Patagonian Shelf. Analysis of observational data reveals strong internal tide signals near the Patagonian shelf break. Proxy vectors of the baroclinic energy fluxes show that the

internal tide propagation occurs predominantly along the isobaths and is not aligned with the barotropic tide, possibly due the internal wave refraction on the Malvinas Current.

TABLE OF CONTENTS

LIST OF TABLES

LIST OF FIGURES

CHAPTER 1

INTRODUCTION

Ocean tides play an essential role for life on Earth. The frictional dissipation of tidal energy constantly slows down Earth rotation since the formation of Earth, resulting in the length of day and night we know today. Ocean tides also induce mixing in the ocean, reinforcing redistribution of nutrients vital for life in the ocean. As a result of gravitational pull from the Moon, the Sun, and other celestial bodies, ocean tides possess a tremendous amount of energy. The dissipation of tidal energy has long been a subject of oceanographic studies (e.g. Munk and MacDonald 1960; Cartwright and Ray 1991; Egbert and Ray 2003). Early estimations of tidal dissipation are inferred from the celestial bodies. When tidal waves propagate around the earth, the misalignment between the tidal bulges and the pulling celestial bodies (such as the Moon) create a phase lag between the gravitational force and the wave crests. The amount of torque created by the gravitational force towards the tidal bulges can slow down the rotation of earth and accelerate the orbit of the Moon overtime, and the work done by the gravitational force is balanced by the dissipation of tidal energy. From astronomical measurements, Munk and Wunsch (1998) estimated a total amount of 3.5 TW energy dissipation in ocean tides. More detailed tidal dissipation schemes were calculated from the global tidal altimetry data (e.g., Cartwright and Ray 1991). Tidal models (e.g., Schrama and Ray 1994; Kantha el al. 1995; Ray et al. 1996) based on Topex/Poseidon altimetry data estimated around 2.5 TW of tidal energy dissipation being associated with the semidiurnal lunar (M_2) component alone.

The geographic distribution of such amount of tidal energy dissipation has been an ongoing topic in academic discussions. In early studies (e.g. Jeffreys 1921), the main sources of tidal dissipation were considered to be a frictional dissipation in the shallow seas. In shallow water areas such as continental shelves, the barotropic tidal currents dissipate energy through frictional interactions with the ocean bottom. Jeffreys (1921) estimated a total amount of 2.2 TW global M_2 tidal dissipation through bottom friction. Later on during the 1970s, after the study of internal wave generation was initiated, the barotropic to baroclinic energy conversion through the generation of internal tides started to be considered as another major source of tidal energy dissipation (e.g., Baines 1973; Bell 1975). Early internal tide models (e.g., Baines 1982; Sherwin el al. 2002) had shown significant barotropic to baroclinic conversion at the continental shelf areas. Later studies (e.g., Egbert and Ray 2001; Jayne and Laurent 2001; St. Laurent and Garrett 2002; Simmons et al. 2004; Garrett and Kunze 2007 among many others) suggest that internal tide generation is more significant in the deep ocean. Around 1 TW (e.g. Munk and Wunsch's 1998, Buijsman et al. 2015) of tidal dissipation due to the generation of internal tides is attributed to the deep ocean with rough bottom topography.

However, since there have long been records of internal wave generation on continental shelves (e.g. Pingree and New 1989; Gerkema et al. 2004; Glenn et al. 2005; Green ae al. 2010; Lozovatsky et. al. 2015), the shelf areas play an equally important role in the contribution to this tidal dissipation path way. Semidiurnal tides propagate in the form of a Kelvin wave along the continental shelves. As the shelf width widens, the wave becomes dispersive, and the alongshore velocity component change sign with offshore distance (e.g., Ke and Yankovsky 2010). The reversal of the velocity component suggests

that the tidal wave can exhibit a reversal of the alongshore energy flux on the shelf relative to the deeper part of the depth profile. If the wave encounters a variation in shelf width as it propagates alongshore, the energy flux on the shelf can develop an area of convergence or divergence. The convergence or divergence of energy fluxes can be released through a cross-isobath energy flux further offshore, which can potentially lead to the generation of internal tides. This dissertation discusses the possibility of tidal dissipation through internal tide generation on wide continental shelves, where barotropic tides propagate alongshore and are modified by the variable bottom topography.

1.1 INTERNAL TIDE GENERATION

In stratified fluid, external forcing can produce density perturbations to the stratified layers, and produce oscillations similar to surface waves, but typically propagating at a much slower speed and with much larger amplitude. Barotropic tides in the ocean typically have a phase speed in the order of O(100) m/s with amplitudes of O(1) m, whereas baroclinic waves generated by barotropic tides propagates in O(1) m/s with amplitudes of O(10) m. Unlike surface waves, internal waves can propagate both horizontally and vertically, transporting energy and enhancing mixing process in seawater. Internal waves are one of the key driving forces of mixing in the ocean (e.g. Kunze and Toole 1997; Kunze et al. 2002). They also contribute to the redistribution of planktonic life forms and larvae in the ocean. The internal waves are typically generated in the stratified water column with variable bottom topography, such as continental shelves, underwater seamount and ocean ridges. The internal tides are internal waves generated by barotropic tidal forcing in the stratified ocean.

Since studies of internal tides were initiated by theoretical models (e.g. Garrett and Munk 1972, Baines 1973, Bell 1975) and in situ experiments (e.g. Gould et al. 1974, Briscoe 1975), the generation of internal tides has been recognized as an important sink of barotropic tidal energy. Baine's (1982) analytical model estimated a significant amount of barotropic to baroclinic conversion on continental shelves. Kantha and Tierney's model (1997) based on Topex/Poseidon altimetry data estimated a total amount of 0.5 TW dissipation for the first mode internal tides in the global ocean. Munk and Wunsch's (1998) study estimated a 0.9 TW loss of the barotropic tidal energy in the open ocean due to the generation of internal tides. The estimation of tidal dissipation from satellite observations attributes most barotropic to baroclinic conversion to the deep ocean. Egbert and Ray's (2001) Topex/Poseidon model (Figure 1.1a) estimated a substantial amount of M_2 tidal dissipation on the wide continental shelf areas such as the Celtic Sea, the East China Sea, and the Patagonian Shelf. The open ocean also manifested a significant amount of tidal dissipation, which was attributed to the scattering of tidal waves in the East Pacific and Mid-Atlantic ridges. In Simmons' et al. (2004) global baroclinic tide model (Figure 1.1b), the major parts of barotropic to baroclinic conversion were located in deep oceans, where the highest amount of conversion was found in the Scotia Sea. Locations near the wide continental shelves also show barotropic to baroclinic conversion, such as in the Bay of Biscay and the Luzon Strait. However little conversion was found on the Patagonian Shelf. Based on global HYCOM simulations, Buijsman's et al (2016) estimated about 359 GW of barotropic to baroclinic conversion in deep ocean, roughly four times the conversion in coastal regions (95 GW).

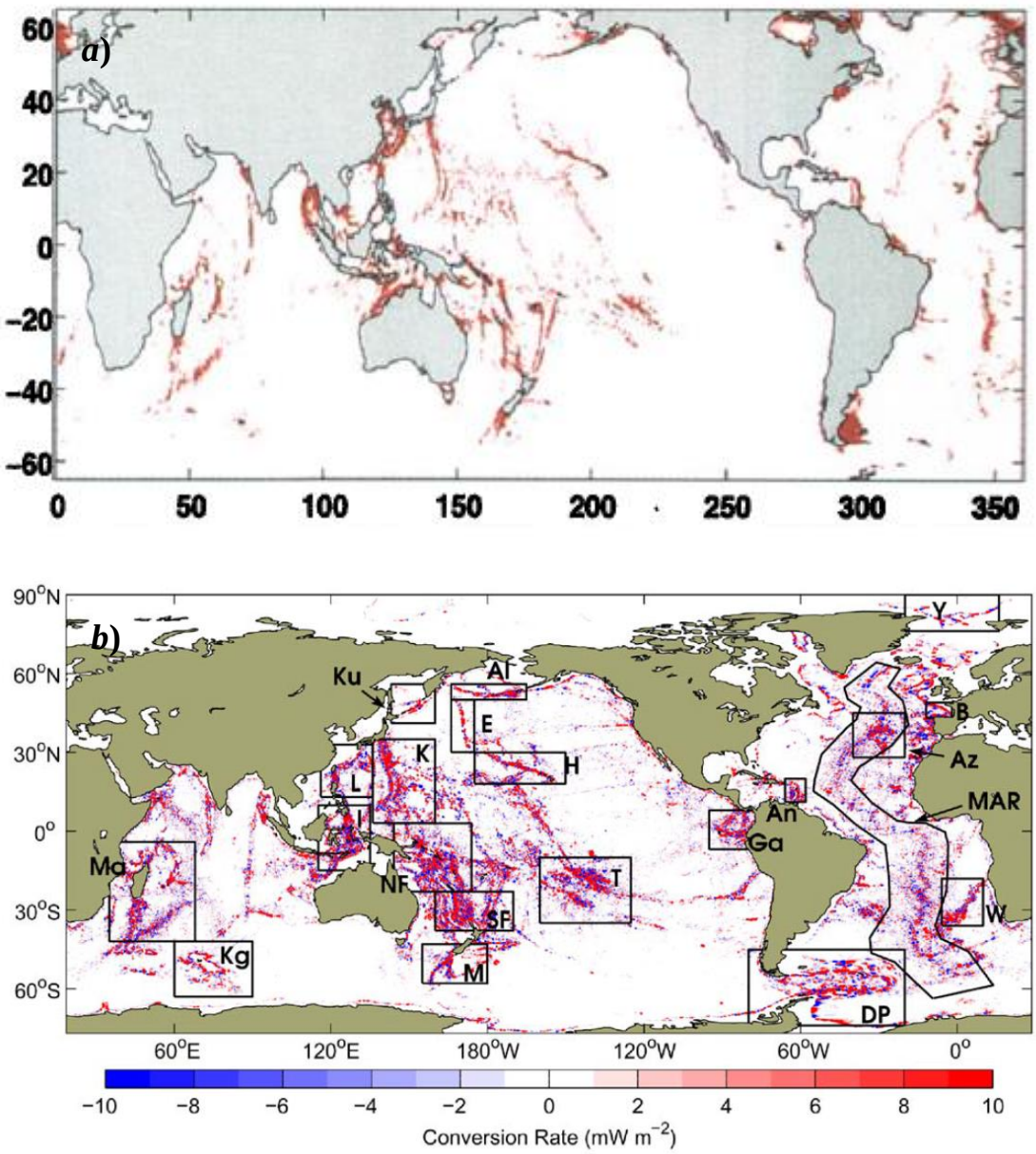

Figure 1.1 (a) Estimation of M_2 tidal dissipation by Egbert and Ray 2001. The estimation for shallow seas and deep oceans was calculated separately. The dissipation due to scattering of baroclinic mode was estimated by an additional linear friction coefficient. (b) Barotropic to Baroclinic conversion combined from regional estimations by Simmons et al 2004.

Internal tides are generated when barotropic tidal currents encounter topographic anomalies. Because tides propagate along the continental shelves, parallel to the isobaths, internal tide generation on the continental shelves is considered to be weaker than in the ocean ridge areas. For example, the Patagonian Shelf is one of the locations with the strongest semidiurnal tides and the most energetic tidal dissipation, but little internal tide generation was found in baroclinic tidal models. Nonetheless, Palma's et al (2004) circulation model showed that while the dominant M_2 tide propagates along the Patagonian shelf, a substantial amount of onshore energy fluxes (6 GW) was found at the northern part of Patagonian shelf (40°S – 44°S), along with a concentrated tidal dissipation (28 GW) in that region (Figure 1.2). This indicates a potential condition for internal tide generation that is not captured by the global baroclinic models.

1.2 HYBRID KELVIN-EDGE WAVES

Semidiurnal tides typically propagate along the continental shelves as Kelvin waves and form amphidromic systems in the ocean basins. When the shelf becomes wide, the propagating Kelvin waves can morph into topographically trapped wave modes (Munk et al. 1956). Consider the linear shallow water equations for a non-viscous fluid of uniform density rotating at a constant angular velocity $f/2$. The water depth changes only with the offshore distance, which allows a periodic wave-like solution with respect to the alongshore coordinate and time. These assumptions yield a well-known boundary problem (e.g., Huthnance, 1975) describing a full set of barotropic trapped modes in the coastal ocean:

$$\frac{d^2\eta}{dy^2} + \frac{1}{h}\frac{dh}{dy}\frac{d\eta}{dy} + \eta\left(\frac{kf}{\omega h}\frac{dh}{dy} - \frac{f^2-\omega^2}{gh} - k^2\right) = 0 \qquad (1.1)$$

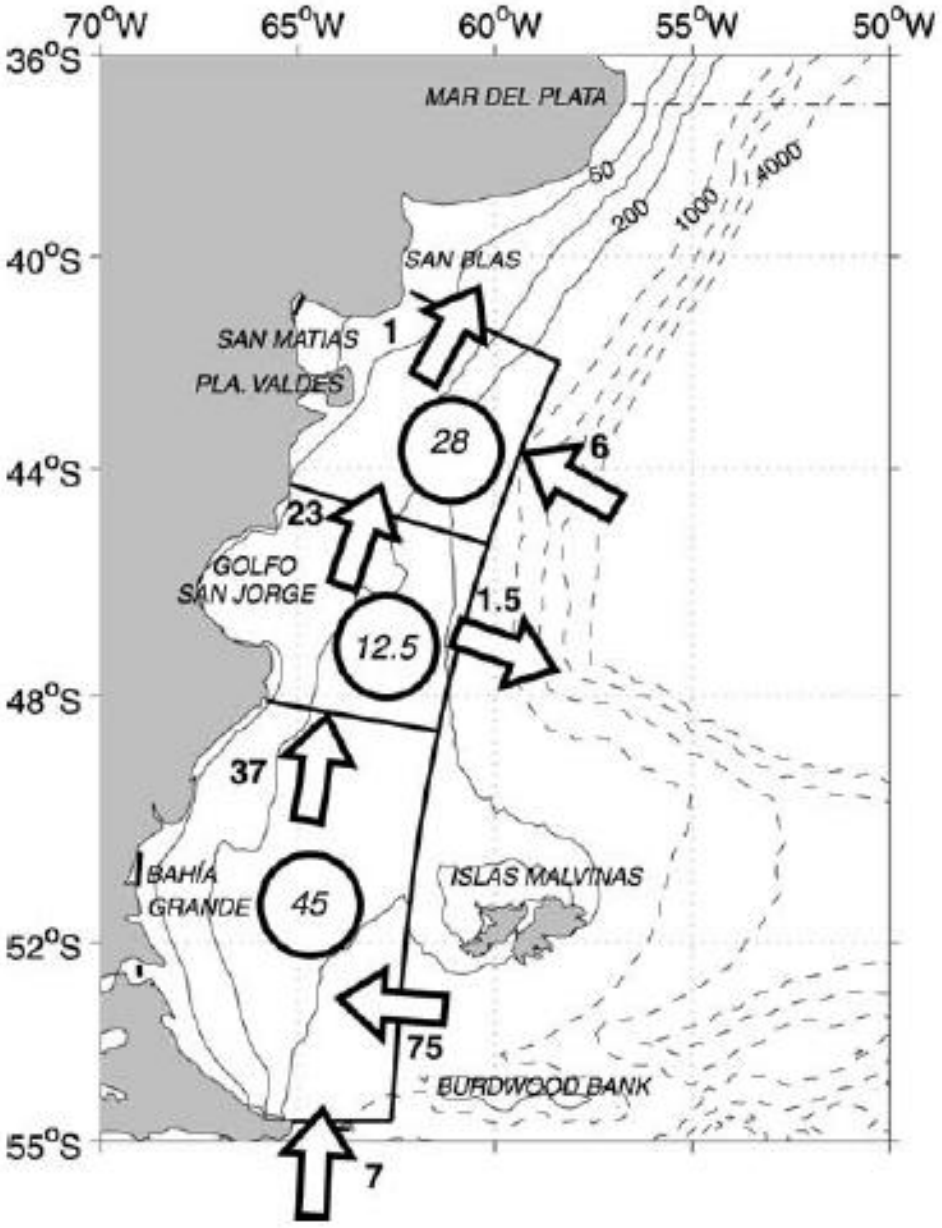

Figure 1.2 Barotropic M_2 energy fluxes at the Patagonian shelf region (from Palma et al. 2004). The arrows show the energy fluxes and the circles show the corresponding tidal dissipation (in GW).

$$v = 0 \quad \text{at} \quad y = 0 \tag{1.2}$$

$$\eta \to 0 \quad \text{as} \quad y \to \infty \tag{1.3}$$

where y is the offshore coordinate, v is the cross-shore velocity component along the y-axis, η is the free surface perturbation from a horizontal plane, h is the water depth, k is the alongshore wavenumber, ω is the wave frequency, and g is the acceleration due to gravity.

This boundary problem was discussed in detail by Huthnance (1975) and Mysak (1980). For non-trapped waves propagating energy offshore the solution in the deep ocean of a constant depth will be oscillatory with respect to the y-coordinate. The fundamental zero mode of the solution is a right-bounded (left bounded) trapped wave mode in the northern (southern) hemisphere. At low wave numbers, the zero mode resembles a Kelvin wave (Figure 1.3) trapped by the coastal wall. At high wave numbers, the zero mode resembles an edge wave. The higher modes of the solution are either left or right bounded and can propagate in both directions. At sufficiently low wave numbers, the wave modes merge into the continuum of Poincare Waves and are no longer trapped. When semidiurnal tides propagate to wide continental shelves as Kelvin waves, as the shelf widens, the tidal wave becomes dispersive; the phase speed decreases and the wave number increases. As wave number increases, the trapped semidiurnal zero mode is no longer a pure Kelvin wave, but exhibits characteristics of a zero mode edge wave. This transition wave mode can be defined as hybrid Kelvin-Edge wave (HKEW) mode (e.g. Yankovsky 2009; Ke and Yankovsky 2010). As the shelf width changes, the group velocity of the HKEW can change from a high group velocity close to the phase speed to a low group velocity when changing from a Kelvin to an edge wave. When group velocities become sufficiently low,

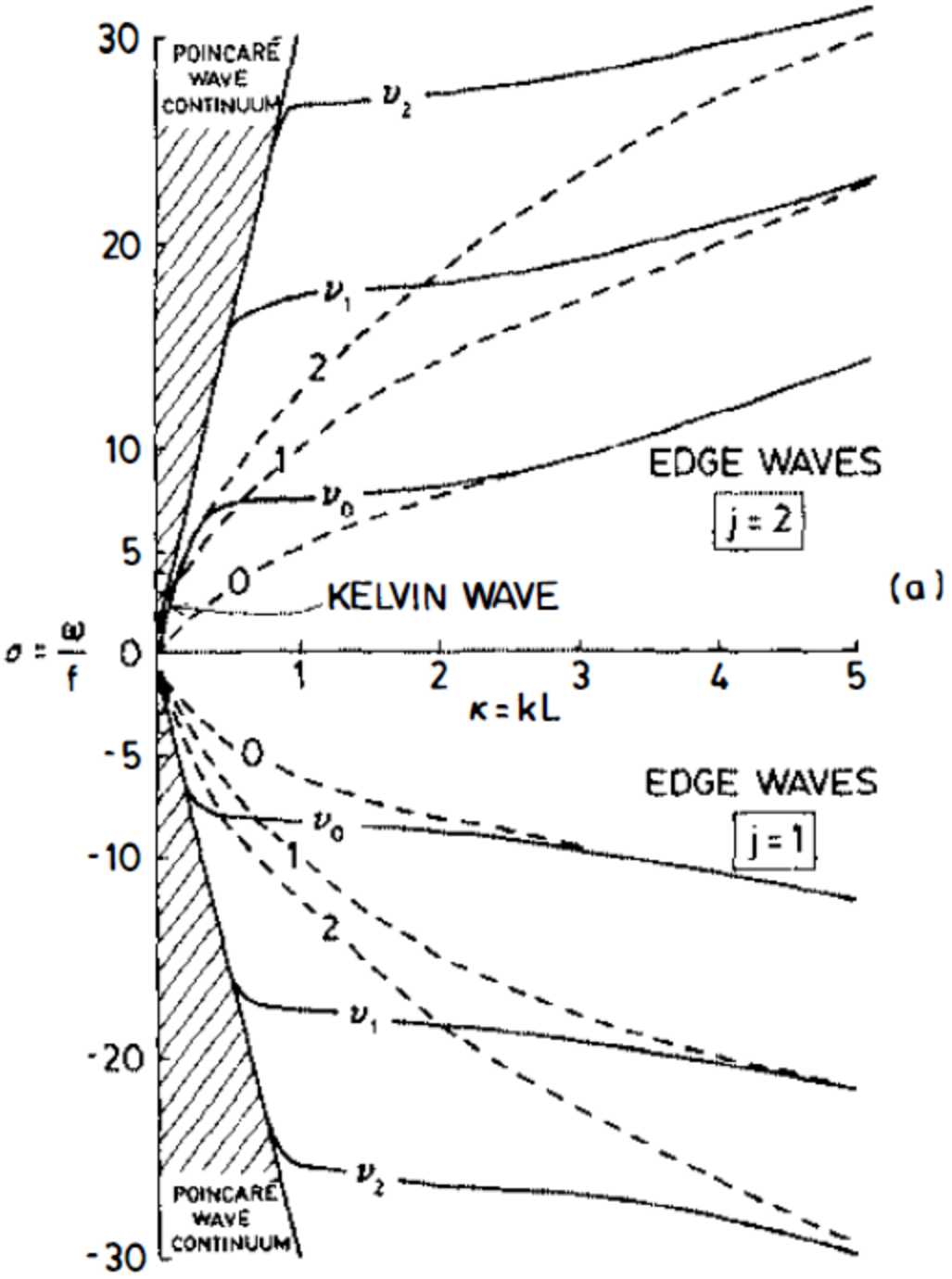

Figure 1.3 An example of fundamental wave modes of the boundary problem (1.1)-(1.3). The results are solved by Mysak (1980) under the topographic condition of a linear continental slope connected to an open ocean with uniform depth.

propagation of the tidal energy become inhibited. This implies that on wide continental shelves, changes in shelf width can have a strong impact on the energy flux of the alongshore propagating tidal waves. In the world Ocean, wide continental shelves can experience a change in shelf widths from 100 km to more than 300 km (e.g. Patagonian Shelf, Western Australian Shelf). The different HKEW structures at the semidiurnal frequency suggest that when the shelf width changes, semidiurnal tidal waves can change from Kelvin wave structures to edge wave structures. Ke and Yankovsky's (2010) computed the HKEW dispersion structure for shelf widths ranging between 100 km and 350 km (Figure 1.4). At semi-diurnal frequency, the fundamental zero mode on a 200 km wide shelf resembles a Kelvin wave with a low wave number, whereas the wave mode on a 300 km wide shelf resembles an edge wave with a high wave number. For each fundamental zero mode of the HKEW, the group velocity decreases during the transformation from the Kelvin wave mode to the edge wave mode. In between the shelf width of 250 km and 300 km, the dispersion curves of the fundamental zero modes have a near-zero group velocity at the semidiurnal frequency. This suggests that when semidiurnal tides propagate along a shelf with width of ~300 km, even a moderate change of shelf width can result in a significant change in the propagating tidal wave mode structure. The occurrence of a near-zero group velocity during the transformation of wave mode structures indicates that the alongshore energy propagation is inhibited at the corresponding shelf width. As a result, the change in shelf width can cause a divergence of the tidal wave energy flux, with compensating cross-isobath energy flux. It is possible that the cross-isobath energy fluxes responding to the changes in shelf width can serve as a barotropic forcing for the internal wave generation in the stratified ocean. Among the wide shelf areas

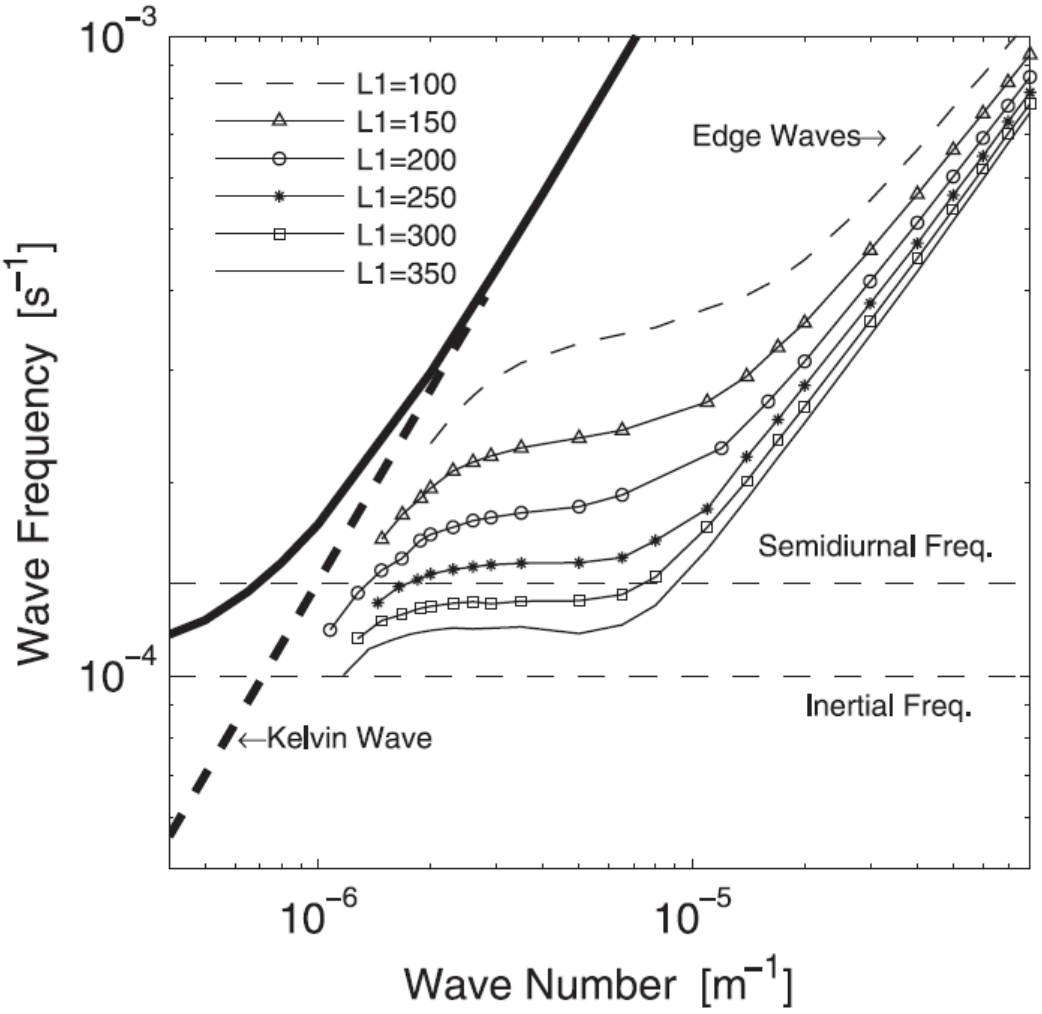

Figure 1.4 From Ke and Yankovsky (2010). Dispersion relation of the zero mode HKEW at different shelf widths.

of the world ocean, both Celtic Sea and the Patagonian Shelf are characterized by strong semidiurnal tides and rapid change in shelf width. The shelf break areas of Western Europe, including the Bay of Biscay, and the Celtic Sea shelf break are considered to be one of the locations with the most energetic internal wave fields (e.g. Pingree and New 1989; Pingree and New 1995; Gerkema et al. 2004; Vlasenko and Stashchuk 2015). In the Patagonian Shelf area, most tidal dissipation is assumed to be due to frictional dissipation, and the barotropic to baroclinic energy conversion was considered to be in the deep ocean by global baroclinic models. Satellite studies (e.g. Jackson 2007, Magalhães and Silva 2017) did find internal waves in the region, but whether the internal wave fields are of tidal origin remains unclear.

1.3 INTERNAL WAVE MODES IN A CONTINUOUSLY STRATIFIED FLUID

Internal waves can propagate along the interface of two homogeneous layers or in a continuously stratified fluid. We consider the internal waves in a continuously stratified fluid. The linearized equations of motion under the Boussinesq approximation is characterized by:

$$\rho_0 \left(\frac{\partial u}{\partial t} - fv\right) = -\frac{\partial p}{\partial x} \tag{1.4}$$

$$\rho_0 \left(\frac{\partial v}{\partial t} + fu\right) = -\frac{\partial p}{\partial y} \tag{1.5}$$

$$\rho_0 \frac{\partial w}{\partial t} + \rho' \mathrm{g} = -\frac{\partial p}{\partial z}\,, \tag{1.6}$$

where $\rho_0(z)$ is the background density and ρ' is the density perturbation; p is the pressure; u, v, and w are the velocity components along the standard orthogonal coordinates x, y, and z, respectively.

The continuity equation is:

$$\frac{\partial u}{\partial x} + \frac{\partial v}{\partial y} + \frac{\partial w}{\partial z} = 0 \tag{1.7}$$

The buoyancy $b = \frac{\rho' g}{\rho_0}$ and the buoyancy frequency $N^2 = -\frac{g}{\rho_0}\frac{\partial \rho_0}{\partial z}$ satisfy

$$\frac{\partial b}{\partial t} - wN^2 = 0 \tag{1.8}$$

Solving (1.4)-(1.8) for *w* yields:

$$\frac{\partial^2}{\partial t^2}\nabla^2 w + f^2\frac{\partial^2 w}{\partial z^2} + N^2\nabla_h^2 w = 0 \tag{1.9}$$

We seek the solution in the form of normal vertical modes propagating horizontally in the unbounded ocean:

$$w = W(z)e^{i(kx-\omega t)} \ , \tag{1.10}$$

where *k* is the wavenumber along the horizontal plane; and $W(z)$ satisfies:

$$\frac{d^2 W}{dz^2} + k^2\left(\frac{N^2-f^2}{\omega^2-f^2} - 1\right)W = 0 \ , \tag{1.11}$$

with boundary conditions

$$W = 0, z = -D, 0 \tag{1.12}$$

The eigenfunctions for *W* are sine functions for constant *N*:

$$W = sin\left(\frac{j\pi z}{D}\right), j = 1, 2, 3 \ldots \tag{1.13}$$

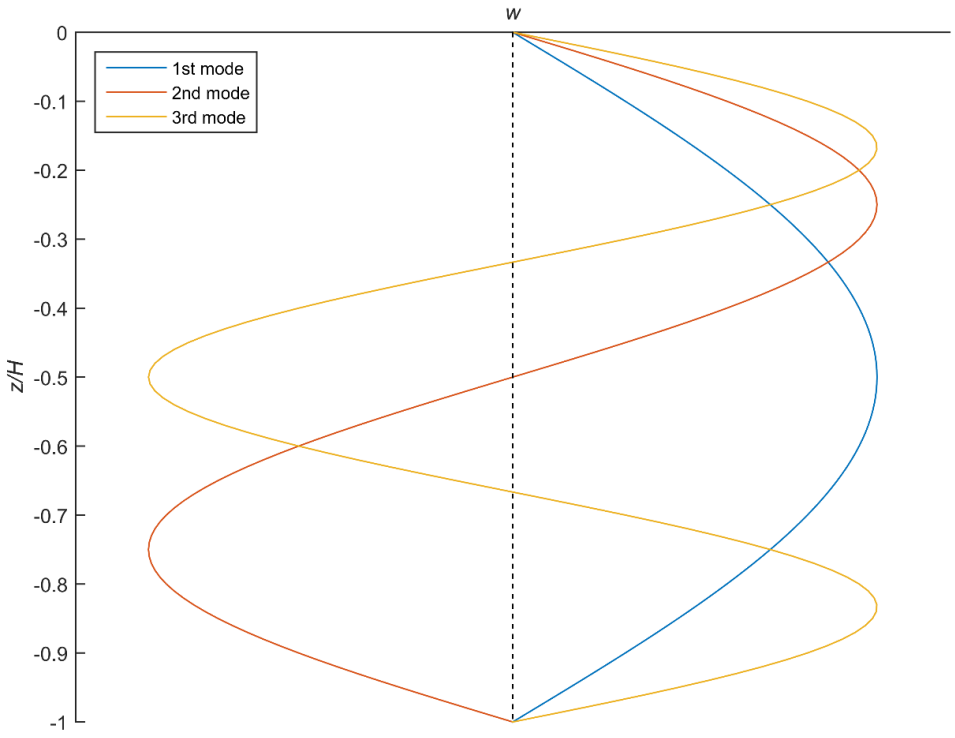

Figure 1.5 The vertical mode structures *w* of internal wave modes 1-3 for a constant buoyancy frequency.

An example of the vertical profile for W is shown in Figure 1.5. The maximum of w for each internal wave mode occurs at a different depth. This suggest that different matches between the barotropic forcing and the internal wave mode structures can result in a different internal wave field

1.4 OBJECTIVES AND DISSERTATION LAYOUT

The possible mechanism for internal tide generation in the wide continental shelf areas is discussed in this dissertation. The main objective of this research is to use numerical models and in situ data analysis to investigate the barotropic tidal energy fluxes on wide continental shelves and the associated internal wave generation. The specific objectives include:

1. Simulating the dynamics of a HKEW propagating along wide continental shelves with variable shelf widths using barotropic models, and evaluating favorable conditions for strong cross-isobath energy fluxes that can indicate important conditions for the internal tide generation in stratified models.

2. Investigating the possibility for internal tide generation in wide shelf areas using stratified models, estimating the consequential baroclinic energy fluxes and barotropic to baroclinic energy conversion.

3. Analyzing in situ data for observational evidence of the internal tide generation on the Patagonian Shelf, and proposing a possible explanation for why global baroclinic models do not show strong offshore internal wave radiation at the Patagonian shelf break.

The following parts of this dissertation are organized as follows:

Chapter 2 introduces the numerical modeling methods for barotropic and baroclinic studies and describes the general model set up for this research. Then it presents the numerical methods for calculating the HKEW mode structure. Finally, it presents the energy diagnostics used for evaluating the model output.

Chapter 3 presents the numerical model study under barotropic conditions. The numerical simulations are configured with a linear continental slope transiting from one shelf width to a wider or a narrower shelf width. The theoretical structures of propagating semidiurnal waves are compared, and then the barotropic responses are shown for each model run. Finally, the strength of scattering is parameterized by the topographical conditions and the barotropic energy flux divergence.

Chapter 4 presents the numerical study under baroclinic conditions. This chapter adds the stratified conditions to the model simulations. The barotropic responses are compared to the model results from the previous chapter. Then, barotropic to baroclinic energy conversions and a normalized baroclinic energy radiation are used to evaluate the intensity of internal wave radiation. Finally, the internal wave fields are compared for each model run.

Chapter 5 presents the internal tide study on the Patagonian Shelf based on the observational data analysis. A possible explanation for the lack of offshore radiation is explored through analyzing the data from two moorings deployed along the Patagonian shelf break. The internal tide propagation is delineated by estimating a proxy for the

baroclinic energy flux. It is concluded that the presence of energetic western boundary current blocks the offshore radiation of internal tides.

Chapter 6 gives a summary and discussion of this research.

.

CHAPTER 2

NUMERICAL METHODS

The previous chapter introduced a possible mechanism of the barotropic tidal waves scattering into other wave modes including internal wave modes. A numerical simulation is conducted to study this mechanism. In this chapter, the numerical modeling methods and model configuration are described for all studies included in this dissertation. The model simulations include a set of model runs with uniform density (barotropic model) and a set of model runs under stratified condition (stratified model). The numerical methods for calculating HKEW and internal wave theoretical structures are introduced in the following section. And finally, energy equations are introduced in the last section.

2.1 NUMERICAL SIMULATIONS FOR INTERNAL TIDE GENERATION

Early studies of internal tides used two-dimensional analytical models (e.g. Baines 1982; Sjöberg and Stigebrandt 1992; Morozov 1995) to estimate the baroclinic energy fluxes generated from the barotropic forcing. These analytical models simplify the bottom topography of the global ocean and are unable to resolve three-dimensional irregularities of the ocean bottom. Later studies use satellite altimetry data (e.g. Schrama and Ray 1994; Kantha el al. 1995; Ray et al. 1996) to analyze the global baroclinic energy distribution, however, the satellite data only allow to estimate internal waves with strong sea surface signatures. In the areas with complex bottom topography, higher internal wave modes or bottom trapped internal waves cannot be resolved from the satellite altimetry data. The

three-dimensional complexity of the internal tide generation can be resolved by numerical models, including global realistic models such as the Hybrid Coordinate Ocean Model (HYCOM, Bleck 2002; Chassignet et al. 2003; Halliwell 2004), and regional models such as the MIT Ocean General Circulation Model (MITgcm, Marshal et al. 1997) and the Regional Ocean Modeling System (ROMS, Song and Haidvogel 1994; Song and Wright 1998; Shchepetkin and McWilliams 2003, 2005). Depending on the internal wave modes, semidiurnal internal tides on continental shelves can have a wave length ranging from O(10) km to O(100) km, which is much larger than the scale of water depth. Because of this, the fluid acceleration is much more pronounced in the horizontal direction, resulting from the wave amplitude. The vertical acceleration from nonhydrostatic pressure is comparatively small. The nonhydrostatic pressure becomes important only when the internal wave length becomes comparable to the water depth. Thus, most internal tide models are hydrostatic models, such as the Regional Ocean Modeling System (ROMS, e.g. Moore et al. 2004; Di Lorenzo et al. 2006; Buijsman et al 2011; Osborne et al. 2011) used in this study.

2.2 ROMS MODEL SETUP

The HKEW cross-shelf structure at semidiurnal frequency depends on the width of the shelf. This study simulates the scattering effect of alongshore propagating semidiurnal tides due to the changes in the shelf width. The simulations include a set of barotropic model runs presented in the next chapter, followed by a set of stratified model runs in the fourth chapter. Both barotropic and stratified models have a domain with a 2000 × 2000 km square basin and a closed southern boundary representing a coastline. The *x*-coordinate points eastward (downstream direction), the *y*-coordinate points northward (offshore

direction), and the unperturbed free surface is at z=0. For the barotropic model, the horizontal resolution is 5 km in both directions, and 10 *S*-coordinate grid cells are applied in the vertical. For the stratified model, the horizontal resolution is 4 km in both direction, and the vertical resolution is 25 *S*-coordinate grid cells. A higher resolution is also applied for baroclinic conditions when necessary, which will be discussed in the following chapters.

The model depth profile *h(y)* comprises two piecewise-constant slopes (representing areas of a continental shelf and slope) adjacent to an open ocean of a constant depth (Figure 2.1). For the standard configuration, the bottom topography metrics are: the coastal depth h_1 = 5 m, the shelf break depth h_2 = 100 m, and the open ocean depth h_3 = 2000 m. For the barotropic model, the continental slope width L_2 = 100 km. For the stratified model, three continental slope widths are used, L_2 = 50 km, 75 km, and 100 km. In the barotropic model, the shelf width L_1 = 150 km, 250 km, and 300 km. In the stratified model, the shelf width L_1 = 150 km and 300 km. The bottom topography is smoothed over three grid points at the locations where the bottom slope has discontinuities (y = L_1 and y = L_1+ L_2). The selection of depth profiles in this study represents areas of wide continental shelves in the World Ocean where the existence of topographically-modified Kelvin waves is expected. Examples of these continental shelves with strong semidiurnal tides include the southwestern and northwestern shelves in the Atlantic, the Bay of Biscay and the Celtic Sea off the European margin, the East- and South China Seas, and the northern shelf of Australia. Of some relevance is also the Arctic shelf, although for the most part the M_2 frequency there belongs to the subinetrial band. The specified deep ocean depth of 2 km is

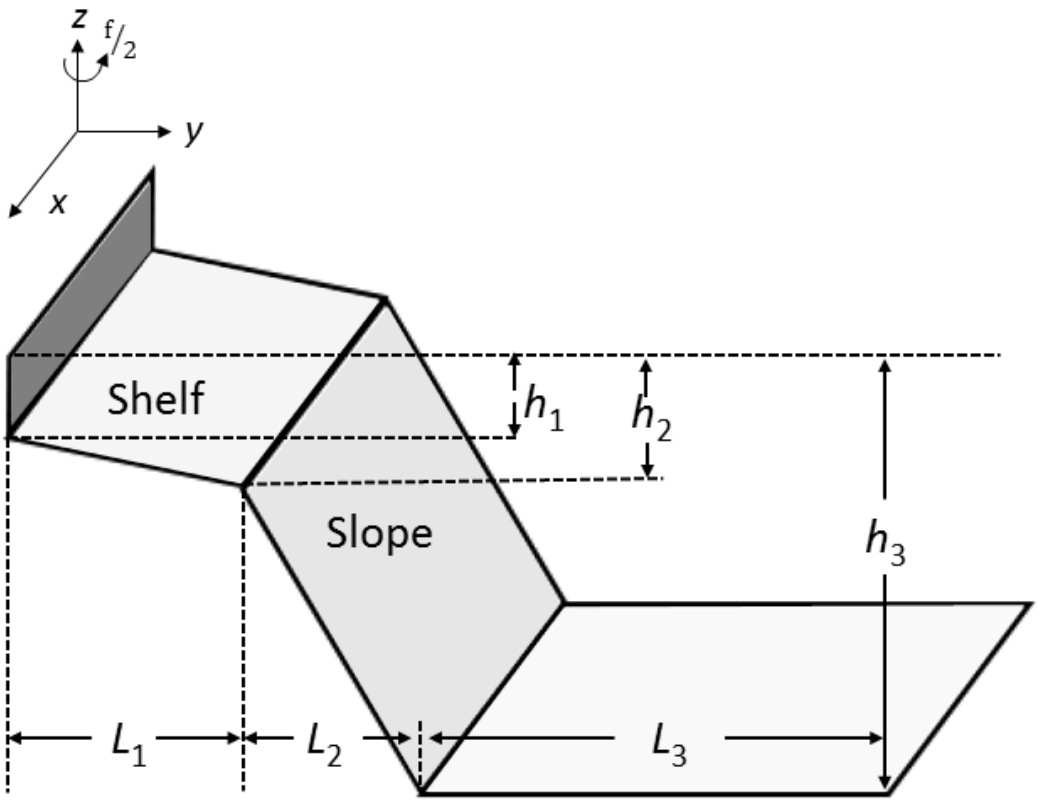

Figure 2.1 The depth profile used in ROMS models and computations of the boundary problems.

less than the actual open ocean depth in the examples above. This somewhat reduced value of h_3 is needed in order to facilitate numerical calculations in the next section and has little qualitative impact on the processes studied, as long as the shelfbreak depth h_2 remains a small fraction of h_3. To further prove it, examples of shelf topography with h_3 set to 4000 m will be presented in the next chapters.

The model geometry (Figure 2.2) comprises three segments: two continental shelves of constant but different widths (referred to as upstream and downstream) adjoined through a 150 km-long transition zone (referred to as a scattering region), where the shelf width smoothly translates from its upstream to downstream value. The transition from upstream to downstream shelf width is defined in two different ways: by coastline when the continental slope isobaths remain straight while the coastline changes its orientation, and by slope when the coastline remains straight while both the shelfbreak and the continental slope isobaths deviate from the alongshore direction. When the shelf width changes by the coastline, the area of the model domain between the coastline and y=0 is masked as land. Both the narrowing (when L_1 decreases downstream) and the widening (when L_1 increases downstream) shelf configurations are applied. The two-slope topography is retained in the scattering region, where the depth changes linearly between its coastal wall h_1 and shelfbreak h_2 values, and then between h_2 and h_3 over the continental slope. Within the scattering region the shelf width is defined as:

$$L_1(x) = L_{1U} + \frac{L_{1D}-L_{1U}}{2}\left\{1 - cos\left[\frac{\pi(x-X_U)}{X_D-X_U}\right]\right\}, \quad (2.1)$$

where subscripts U and D refer to the upstream and downstream shelves, respectively, and X_U and X_D are the alongshore coordinates of the scattering region edges. X_U varies between

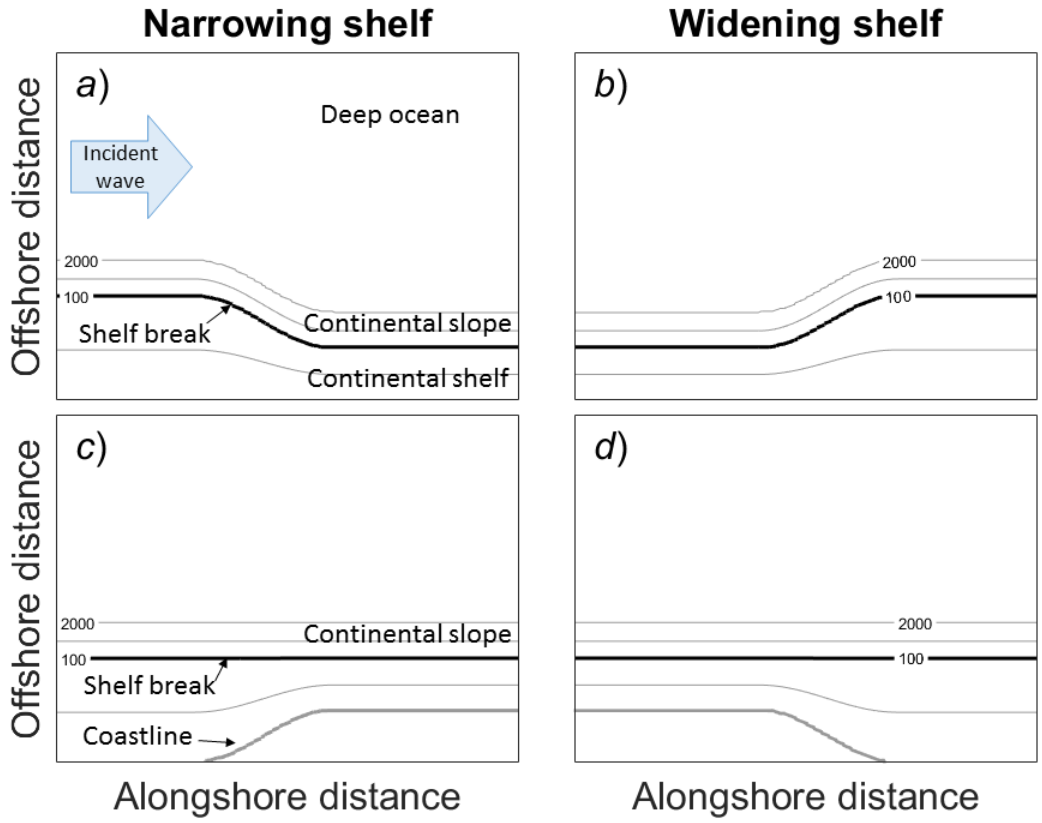

Figure 2.2 Schematic of the model topography with the shelf width varying by a slope (a, b) and by a coastline (c, d). Left/right column is the narrowing/widening shelf.

different model runs from 300 to 850 km depending on the properties of the modelled wave field with the objective of minimizing: (i) the interference of the scattered wave field with the upstream (western) boundary, and (ii) the spurious reflection of the wave signal from the offshore (northern) and downstream (eastern) boundaries. In order to extend the parameter range of the numerical experiments, one additional barotropic model run is performed for a widening shelf (L_1 increases from 150 to 250 km) over a longer scattering region of 200 km, and one additional stratified model run is performed over a shorter scattering region of 100 km. Also, model runs of a widening shelf with h_3=4000 m are presented. For the barotropic model, the barotropic time step is set to 15 s and 900 s for the baroclinic time step. For the stratified model, the barotropic time step is set to 5 s and 300 s for the baroclinic time step.

In the barotropic model, the density ρ is constant (set to 1025 kg m^{-3}). In the stratified model, the density is configured by the linear equation of state:

$$\rho = \rho(T,S) = \rho_0 - \rho_0 K_t (T - T_0) + \rho_0 K_s (S - S_0), \qquad (2.2)$$

where ρ_0, T_0, and S_0 are the background density, temperature and salinity respectively, K_t is the thermal expansion coefficient, and K_s is the saline contraction coefficient. The density profiles are configured with both constant and surface-intensified stratification, including a linear density change from surface to bottom by 2 kg/m^3 (this density profile is referred to as *l2*) for h_3=2000 m and by 4 kg/m^3 (referred to as *l4*) for h_3=4000 m, corresponding to a constant buoyancy frequency N=3.09 × 10^{-3} s^{-1}; and a linear density change of 6 kg/m^3 (referred to as *l6*) for h_3=2000 m, corresponding to N=5.36 × 10^{-3} s^{-1}. The density profile with surface-intensified stratification is defined as:

$$\rho(z) = 1026 - \Delta\rho_1 \frac{z+h_3}{h_3}, \quad z < h_{pycn}$$

$$\rho(z) = 1026 - \Delta\rho_1 \frac{z+h_3}{h_3} + \Delta\rho_2 \left[cos\left(\pi \frac{z+h_{pycn}}{2h_{pycn}}\right) - 1\right], \quad z > h_{pycn} \qquad (2.3)$$

where h_{pycn} is the depth of the pycnocline. For h_3=2000 m, h_{pycn}=600 m, $\Delta\rho_1$=0.5 kg/m^3, and $\Delta\rho_2$=1.5 kg/m^3, resulting in a total change of 2 kg/m^3 (referred to as *s2*) from surface to bottom. For h_3=4000 m, h_{pycn}=1000 m, $\Delta\rho_1$=2 kg/m^3, and $\Delta\rho_2$=1 kg/m^3, resulting in a total change of 3 kg/m^3 (referred to as *s3*) from surface to bottom.

The southern boundary in the model is a slippery wall of a constant depth h_1. At the western boundary, the incident wave in the form of a semidiurnal fundamental zero mode is specified. The free surface structure is obtained from solving the boundary problem (1.1)-(1.3); it fluctuates over a 12-hr period starting from zero at the initial time (as a *sine* function). A corresponding velocity normal to the boundary is derived from the simplified momentum balance between the inertia, the Coriolis force, and the pressure gradient force. At the northern boundary, free surface perturbations are radiated at the long gravity wave speed (Chapman 1985), while the Orlanski-type radiation condition (Orlanski 1976) is applied to both normal and tangential velocity components. At the eastern boundary, all field variables are radiated by using the Orlanski radiation condition.

Each model starts from rest and continues for 144 hr in barotropic cases and 200 hr in baroclinic cases. For the stratified model and the shelf narrowing from 250 km to 150 km case, as well as for h_3=4000 m in the barotropic model, the incident wave amplitude is ramped up linearly over 3 wave periods to its nominal value. The numerical model output is saved at 1-hr time intervals. The prescribed η amplitude in the incident wave at the coast

is 0.08 m for widening shelves and 0.2 m for narrowing shelves. For selected incident wave amplitudes, the maximum free surface displacement at the coast within the numerical domain remains an order of magnitude smaller than water depth h_1 at the coastal wall.

The vertical diffusion and viscosity in this model are parameterized by the Mellor-Yamada level 2.5 turbulent closure scheme (Mellor and Yamada 1982), where the background vertical mixing coefficient is set to 1×10^{-5} m^2/s for momentum and 1×10^{-6} m^2/s for density. The bottom drag coefficient is set to 2×10^{-3} for the standard configuration, and 5×10^{-4} to represent simulations with low friction. The Coriolis parameter f is set to 10^{-4} s^{-1}. No horizontal eddy viscosity is specified in the model, although the horizontal momentum advection is approximated with the third-order upstream scheme, which causes some lateral biharmonic numerical damping (e.g., Haidvogel and Beckmann, 1999).

2.2 COMPUTATIONAL METHODS TO OBTAIN THEORETICAL STRUCTURES

2.3.1 HKEW modes

In numerical experiments, the incident wave structure specified as a boundary condition for η is obtained by solving the boundary problem (1.1)-(1.3) for the depth profile shown in Figure 2.1. Brink and Chapman (1985) solved the boundary problems by resonance iterations. The program searches for the solution of (1.1) based on a given initial value of the wave number k and wave frequency ω. The program yields a solution for the fundamental modes of HKEW only when the initial pairs of k and ω are close to the real value, otherwise, the program will yield a solution for other wave modes.

Since the iteration program is not demanding in computing power, one way to accelerate the process of calculating an entire dispersion diagram for a fundamental wave

mode is to generate a large dataset composed of all wave mode solutions within a range of frequency, and train supervised machine learning models to identify the wave modes. For example, using a bash script for batch processing, the iteration program can generate 1000 solutions with different possible pairs of k and ω within the frequency range of $\omega = 10^{-4}$ s^{-1} and 10^{-3} s^{-1}. The solutions can be a fundamental zero mode, first mode, second mode, or other wave modes. The wave modes can be identified by machine learning models (e.g., a Gaussian radial basis function (RBF) kernel model (Schölkopf et al. 2004); or a Random Forest model (Breiman 2001)) based on the free surface structure in the solutions. The models classify wave modes based on features such as the number of zero-crossing in the free surface structure η, the number of zero-crossing in $\frac{d\eta}{dy}$, the shelf width, and the occurrence of irregularities in the free surface structure.

2.3.2 Internal wave modes

The internal wave modes are computed from the governing equations in Chapter 1. Rewrite the equation (1.11) as:

$$\frac{d^2w}{dz^2} + k^2\left(\frac{N^2-f^2}{\omega^2-f^2}\right)w = k^2 w \ , \tag{2.4}$$

with the same boundary condition in (1.15).

Using the dispersion relation

$$\omega^2 = C^2k^2 + f^2 \ , \tag{2.5}$$

(2.4) can be rewritten in the form of

$$\frac{d^2w}{dz^2} + \left(\frac{N^2-f^2}{C^2}\right)w = k^2 w \tag{2.6}$$

Approximating the derivatives with finite differences discretized over Δz yields a standard form of matrix eigenvalue problem

$$\boldsymbol{AX} = k^2\boldsymbol{X} \tag{2.7}$$

where $\boldsymbol{X}$ is a column vector composed of $w_m\,(m = 1, 2, 3, \ldots, N)$, indicating the vertical velocity at each vertical grids. N is the total number of vertical grid points. $\boldsymbol{A}$ is an $N \times N$ tridiagonal matrix:

$$\begin{bmatrix} a_{11} & a_{12} & 0 & \cdots & 0 \\ a_{21} & a_{22} & a_{23} & & \vdots \\ 0 & a_{32} & a_{33} & \cdots & \\ \vdots & & & \ddots & \\ 0 & & & & a_{NN} \end{bmatrix}$$

From (2.6), each w_m satisfies

$$a_{m,m-1}w_{m-1} + a_{m,m}w_m + a_{m,m+1}w_{m+1} = {k_m}^2 w_m \tag{2.8}$$

where $a_{m,m-1} = \frac{1}{\Delta z^2}$, $a_{m,m} = \frac{N_m^2 - f^2}{C^2} - \frac{2}{\Delta z^2}$, and $a_{m,m+1} = \frac{1}{\Delta z^2}$.

The wave number K_h can be obtained from the eigenvalue of the matrix $\boldsymbol{A}$.

For the stratified model runs, (2.4) is approximated assuming hydrostatic condition:

$$\frac{d^2w}{dz^2} + k^2\left(\frac{N^2}{\omega^2 - f^2}\right)w = 0 \tag{2.9}$$

2.3 ENERGY DIAGNOSTICS

In hydrostatic model, the density $\rho(x, y, z, t)$ consist of a constant term ρ_0, a background density term $\rho_b(z)$, and perturbation term $\rho'(x, y, z, t)$, that is

$$\rho(x,y,z,t) = \rho_0 + \rho_b(z) + \rho'(x,y,z,t) \tag{2.10}$$

The horizontal velocity $\boldsymbol{u}_H$ consist of a barotropic term $\boldsymbol{U}_H$ and a baroclinic term $\boldsymbol{u}'_H$, that is

$$\boldsymbol{u}_H = \boldsymbol{U}_H + \boldsymbol{u}'_H \tag{2.11}$$

The horizontal kinetic energy E_{hk} consists of barotropic kinetic energy E_{hk0}, baroclinic kinetic energy E'_{hk}, and a cross term E'_{hk0} . E_{hk} is defined as

$$\begin{aligned} E_{hk} &= \tfrac{1}{2}\rho_0 \boldsymbol{u}_H \cdot \boldsymbol{u}_H \\ &= E_{hk0} + E'_{hk} + E'_{hk0}\,, \end{aligned} \tag{2.12}$$

where

$$E_{hk0} = \tfrac{1}{2}\rho_0 \boldsymbol{U}_H \cdot \boldsymbol{U}_H = \tfrac{1}{2}\rho_0 (U^2 + V^2) \tag{2.13}$$

$$E'_{hk} = \tfrac{1}{2}\rho_0 \boldsymbol{u}'_H \cdot \boldsymbol{u}'_H = \tfrac{1}{2}\rho_0 (u'^2 + v'^2) \tag{2.14}$$

$$E'_{hk0} = \rho_0 \boldsymbol{U}_H \cdot \boldsymbol{u}'_H = \rho_0 (Uu' + Vv') \tag{2.15}$$

In internal wave fields not all potential energy can be transferred into kinetic energy. The available potential energy is defined as

$$E_{ap} = \rho' g z \tag{2.16}$$

The barotropic to baroclinic energy conversion is defined as

$$E_c = \int_{-d}^{\eta} \rho' g W dz = -\int_{-d}^{\eta} \rho'\, g \nabla_H [(z+d)\boldsymbol{U}_H] dz \tag{2.17}$$

The barotropic energy flux is defined as

$$\boldsymbol{F} = g\rho\eta d\boldsymbol{U}_H \tag{2.18}$$

Thus the energy balance is

$$\frac{\partial}{\partial t}\left(E_{hk} + E_{ap}\right) + E_c + \nabla\boldsymbol{F} + E_{0d} = 0, \tag{2.19}$$

where E_d is the barotropic dissipation term.

The baroclinic energy flux is defined as

$$\boldsymbol{F}'(z) = \boldsymbol{u}'_H(z)p'(z), \tag{2.20}$$

where p' is the pressure perturbation defined as

$$p'(z) = \int_z^\eta g[\rho(z) - \rho_0(z-\eta)]dz \tag{2.21}$$

To calculate the baroclinic energy fluxes in the model results, the energy flux $\boldsymbol{F}'(z)$ will be integrated throughout the water column to produce the total baroclinic energy flux

$$\boldsymbol{F}' = \int_{-H}^{\eta} \boldsymbol{F}(z)dz \tag{2.22}$$

Thus the energy balance becomes

$$\frac{\partial}{\partial t}\left(E_{hk} + E_{ap}\right) + \nabla\boldsymbol{F}' + \nabla\boldsymbol{F} + E_d = 0, \tag{2.23}$$

where the dissipation term E_d includes both barotropic and baroclinic dissipation.

Assuming the model solution is periodic such that the energy flux divergence averaged over a tidal period is balanced by dissipation, the energy dissipation then can be

diagnosed through the convergence and divergence of the barotropic and baroclinic energy fluxes. For the barotropic model, the barotropic energy flux $\boldsymbol{F}$ is used in energy diagnostics. For the stratified model, both $\boldsymbol{F}$ and the baroclinic energy flux $\boldsymbol{F'}$ is used in energy diagnostics.

.

CHAPTER 3

MODELING THE SCATTERING OF SEMIDIURNAL HKEW UNDER BAROTROPIC CONDITIONS[1]

This chapter focuses on modeling the scattering of the semidiurnal HKEW under barotropic conditions, and investigating the strength of scattering through the energy flux adjustments. The dispersion relations of the HKEW and the free surface structures of the fundamental zero modes are calculated based on the configuration described in Chapter 2. ROMS simulations of the semidiurnal zero mode HKEW scattering is configured and conducted under barotropic conditions. For each shelf width, a zero wave mode has its distinctive cross-shelf structure of the alongshore energy flux component. As the incident wave encounters a variable shelf width, the alongshore energy flux converges (diverges) on the shelf resulting in an offshore (onshore) energy flux over the continental slope. Numerical experiments presented in this chapter demonstrated that for a strongly convergent alongshore energy flux, the incident wave mode scatters into radiating Poincaré waves. On sufficiently wide shelves, a strong across-isobath energy flux comparable with the incident wave energy flux can be triggered even by relatively modest changes of shelf width. An energy flux divergence parameter D_e is defined, which scales with magnitude and direction of the energy flux across the continental slope. More than 50% of the incident energy flux scatters into modes radiating offshore when D_e is -1 or less.

[1]This has been published in substantial part as "On the nature of cross-isobath energy fluxes in topographically modified barotropic semidiurnal Kelvin waves" by T. Zhang & A. E. Yankovsky in *J. Geophys. Res. Oceans*, 121, 3058–3074

3.1 DISPERSION RELATIONS AND WAVE STRUCTURES OF THE HKEW

The wave structures and the dispersion relation for the depth profile described in Chapter 2 (Figure 2.2) is obtained from the boundary problems in Chapter 1 (1.1)-(1.3). The shelf width L_1=150 km, 250 km, and 300 km is configured in the barotropic model. The resulting dispersion diagram for all three shelf widths shows the lowest, zero and first, superinertial modes (Figure 3.1a). Similar to the solutions discussed in Chapter 1 (Figure 1.3), the Kelvin wave propagates along the coastline in one direction (hereinafter, referred to as the downstream direction), whereas the edge waves can propagate both downstream and upstream. The diagram includes both wave modes with positive wavenumbers k propagating in the Kelvin wave direction and modes with negative k propagating in the opposite, upstream direction relative to the coastline. The most important result is that even for the wide shelves considered here, only a zero mode propagating downstream is present at a semidiurnal frequency. The upstream-propagating zero mode (an edge wave) merges with the continuum of Poincaré waves (non-trapped inertial-gravity waves) and consequently becomes "leaky" at frequencies higher than the semidiurnal frequency. It should be noted here that with the exception of the fundamental Kelvin wave-like mode, all other superinertial trapped modes exhibit a low frequency cut-off and radiate ('leak') their energy offshore. This happens because for sufficiently large spatial scales, the wave refraction over continental shelf breaks down and the wave energy is no longer trapped over the variable depth (e.g. Mysak 1980). This low-frequency cut-off occurs at higher frequencies/wavenumbers either for narrower shelves when the mode number is fixed or for higher wave modes when the shelf width is fixed. For reference, dispersion curves of the first downstream-propagating wave mode for shelf widths of 250 km and 300 km is

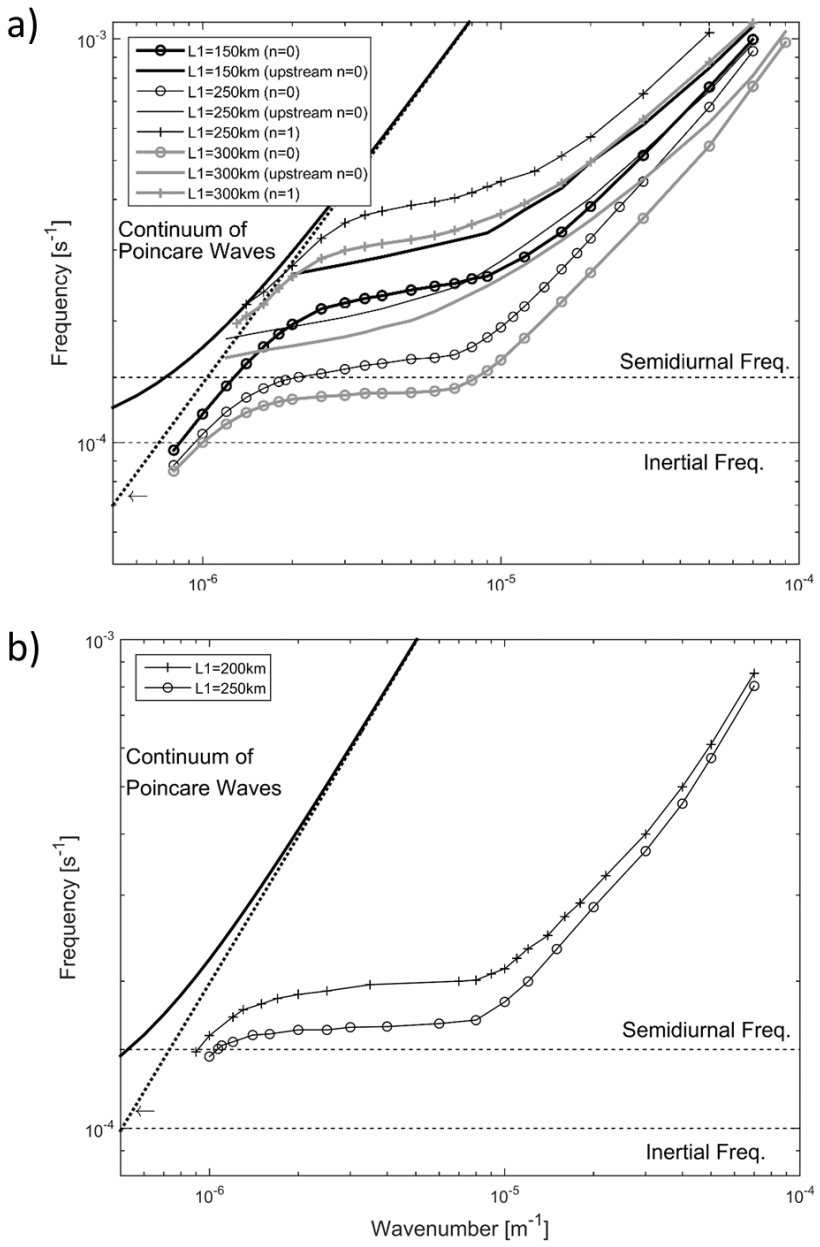

Figure 3.1 Dispersion diagrams for: (a) the three different shelf widths and h_3 = 2000 m, where n is the mode number and upstream refers to the upstream-propagating mode; (b) downstream-propagating zero modes for h_3 = 4000 m.

also shown in Figure 3.1a. Both modes merge with the continuum of radiating waves well above the semidiurnal frequency. The dispersion diagram (Figure 3.1) confirms the conclusion of Ke and Yankovsky (2010) that for a wide range of parameters representing realistic conditions of oceanic margins, only the fundamental zero mode (Kelvin wave-like) can exist as a trapped wave at a semidiurnal frequency.

Next, we will consider how closely the semidiurnal zero mode resembles the analytical Kelvin wave solution for different shelf widths. For L_1 = 150 km, the semidiurnal zero mode has a phase speed $C = \frac{\omega}{k}$ close to the open ocean gravity wave phase speed $\sqrt{gh_3}$, and the wave mode is almost non-dispersive. That is, the wave is only weakly affected by the presence of shelf topography and resembles a Kelvin wave solution. On the 250 km-wide shelf, the zero mode phase speed departs from its open ocean value and the wave becomes dispersive, its group velocity $C_g = \frac{\partial \omega}{\partial k}$ is much lower that the phase speed. Finally, for L_1=300 km, at a semidiurnal frequency C is further reduced but C_g increases again, and this branch of the dispersion curve gradually translates into an edge wave mode at higher frequencies, where effects of earth's rotation become insignificant and the dispersion curves of upstream-propagating and downstream-propagating zero modes nearly overlap in Figure 3.1a. Semidiurnal waves on 250 km and 300 km wide shelves can be defined as HKEW (e.g. Yankovsky 2009; Ke and Yankovsky 2010).

When h_3 is increased (while other metrics of the depth profile are kept the same), the phase speed of the Kelvin wave mode at low frequencies increases as well, while the higher frequency, edge wave branch of the fundamental mode is little affected. Consequently, the part of the dispersion curve with a near-zero C_g extends over a wider

range of wavenumbers as the depth of the open ocean increases. This tendency was described by Ke and Yankovsky (2010, their Figure 3) and is illustrated here for the case of h_3 = 4000 m (Figure 3.1b). In particular, the dispersion curve for L_1 = 250 km exhibits a broad range of k (~1.5-8×10^{-6} m^{-1}) with a near-zero C_g, while for h_3 = 2000 m, the same mode over the same shelf width (Fig. 2, upper panel) has a near-zero Cg at k ≈ 4.5×10^{-6} m^{-1}. For both values of h_3, the frequency of the zero mode with the lowest C_g is approximately the same.

The structure of a semidiurnal zero mode changes with increasing shelf width: the most obvious effect is that the wave becomes more confined near the coast as the shelf width increases (Figure 3.2). For L_1 = 150 km, the free surface perturbation η extends beyond y = 2000 km (that is, beyond the computational domain). Since the shelf width is only a small fraction of the wave's offshore extension, its effect on the wave propagation (wave phase speed) is also small. For L_1 = 250 km, η still extends far offshore, but its amplitude is strongly reduced outside of the variable depth area, and the influence of the shelf on wave properties becomes more significant. Finally, wave perturbation is confined almost entirely over the shelf and slope topography for L_1=300 km, and in this regard the wave structure resembles an edge wave more than a Kelvin wave.

For all three shelf widths, η decreases monotonically with the offshore distance retaining its zero-mode structure (no zero crossings – see Figure 3.2, top panel). This is not so for the alongshore velocity component u. For each case, velocity changes sign twice: positive at the coast, negative farther offshore and positive again in the open ocean of a constant depth. The relative extent of each segment changes widely with the shelf width, for instance, for L_1 = 150 km, u is mostly negative on the shelf, while for L_1 = 300 km, u is

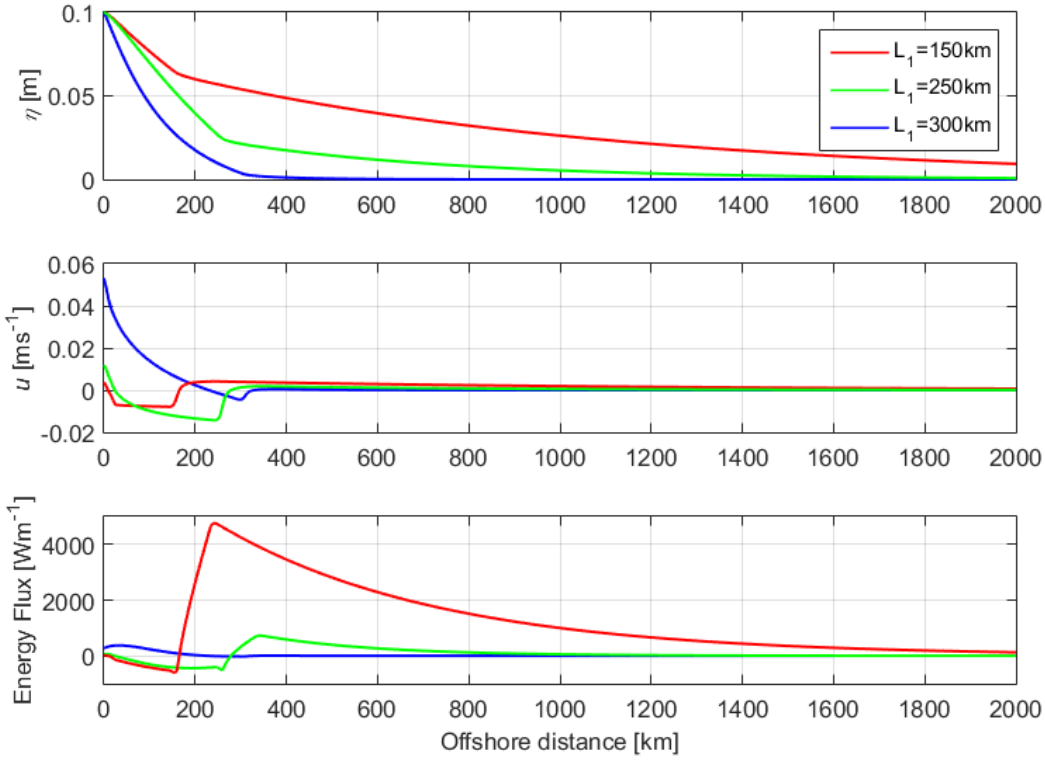

Figure 3.2 Cross-shore wave structure of the zero downstream-propagating semidiurnal mode: (top) free surface, (middle) alongshore velocity, and (bottom) energy flux. Wave parameters are: $\omega = 1.458\times10^{-4}$ s^{-1}, $k = 1.28\times10^{-6}$ m^{-1} ($L_1 = 150$ km); $\omega = 1.457\times10^{-4}$ s^{-1}, $k = 2.1\times10^{-6}$ m^{-1} ($L_1 = 250$ km); $\omega = 1.455\times10^{-4}$ s^{-1}, $k = 8.37\times10^{-6}$ m^{-1} ($L_1 = 300$ km).

mostly positive in the same region (Figure 3.2, middle panel). Also, velocity amplitude on the shelf increases with the shelf width for a fixed amplitude of η (0.1 m at the coast in this case).

The barotropic energy flux $\boldsymbol{F}$ is defined in Chapter 2 (2.18). The offshore structure of the alongshore energy flux amplitude is presented in Figure 3.2 (bottom panel), where its positive values correspond to the downstream direction (also the direction of wave propagation). The instantaneous energy flux oscillates between the amplitude value and zero at the frequency of 2ω. The largest total energy flux (integrated across the numerical domain) for a constant free surface amplitude at the coast corresponds to the depth profile with the narrowest shelf and its maximum occurs at the foot of the continental slope ($y \approx$ 250 km). Energy flux on the shelf is negative for this case, but its contribution into the total energy flux is small. The smallest total energy flux corresponds to the widest shelf; it is confined over the variable depth and is positive on the shelf. For L_1 = 250 km (intermediate case), the positive (inshore) and negative (farther offshore) values of energy flux are comparable and nearly balance each other for the total energy flux. It should be remembered here that this semidiurnal wave mode also has the lowest C_g (which characterizes the alongshore energy propagation) among the three cases considered.

If we now assume that shelf topography does not remain uniform but varies alongshore, two important conclusions about the semidiurnal zero mode adjustment to such changes in shelf width can be deduced from the offshore energy flux structure. First, when the wave propagates from a narrower to wider shelf, the principle of energy flux conservation will require wave amplitude amplification (both in u and η). The opposite is

true for the wave propagation from a wider to narrower shelf. Second, the alongshore energy flux divergence or convergence should occur over the shelf and slope topography depending on the change of the shelf energy flux sign in the direction of wave propagation. For instance, if the wave propagates from a 150 to 250 km wide shelf, strong energy flux convergence should occur at y = 150-250 km, and this convergence can possibly be released through offshore energy flux over the continental slope.

3.2 NUMERICAL EXPERIMENT RESULTS

Since topographically modified Kelvin waves are dispersive and the magnitude of their C_g can be much lower than their corresponding C, it takes several wave periods for the incident wave energy to propagate through the model domain. In most of the cases considered, the group velocity decreases when the zero mode incident wave encounters the scattering region topography, which follows from the dispersion diagram shown in Figure 3.1. Since the alongshore energy flux can be defined as a product of group velocity and the wave energy density (e.g. Huthnance 1975), a decrease of C_g causes energy flux convergence across the whole domain, which further delays the establishment of a periodic (or near periodic) regime in the model domain. On the other hand, due to a very low dissipation in the model and not perfectly transparent open boundaries, the perturbations at the downstream and offshore boundaries start growing at long time intervals and spreading into the model domain. Due to these constrains in our numerical experiments, we select a 36-hr time interval in each model run when the alongshore and cross-shore energy fluxes in the vicinity of the scattering region are nearly balanced, while the energy reflection into a model domain at the downstream and offshore boundaries is minimal. The

adverse effect of long wave energy reflection by deep ocean open boundaries on the solution in the shallow part of model domain increases with the increase of h_3.

The selected 36-hr time interval is averaged into a 12-hr solution, which represents one wave period. This numerical wave solution is assumed periodic and is analyzed below for each model geometry. Typically, the 36-hr averaging interval starts relatively late in each model run, after 80 to 100 hr. One notable exception is the narrowing shelf from 250 to 150 km, when C_g increases as the incident wave encounters the scattering region. For this shelf configuration (narrowing both by the coastline and by the slope), the near-periodic solution in the model domain is established relatively early (30-40 hr) but at later times the numerical solution deteriorates due to the energy reflection from open boundaries.

The first pair of numerical experiments represents a widening shelf width when L_1 changes from 150 to 250 km (Figure 3.3). Phase propagation over a shelf with uniform width (upstream and downstream segments of model topography) is in good agreement with the zero mode theoretical phase speed estimation (shown as black lines in Figures 3.3a and 3.3b), suggesting absence of additional wave modes. However, within the scattering region the phase propagation is distorted, more so in the case when the shelf widens by coastline (Figure 3.3b). This phase distortion has a local character and does not continue downstream. The wave amplitude gradually increases from the upstream to downstream segment of the model domain. This amplitude amplification follows from the results discussed in the previous section: conservation of the total alongshore energy flux requires a higher wave amplitude on a wider shelf. Indeed, the alongshore energy flux averaged over the wave period concentrates closer to the coast in the downstream segment

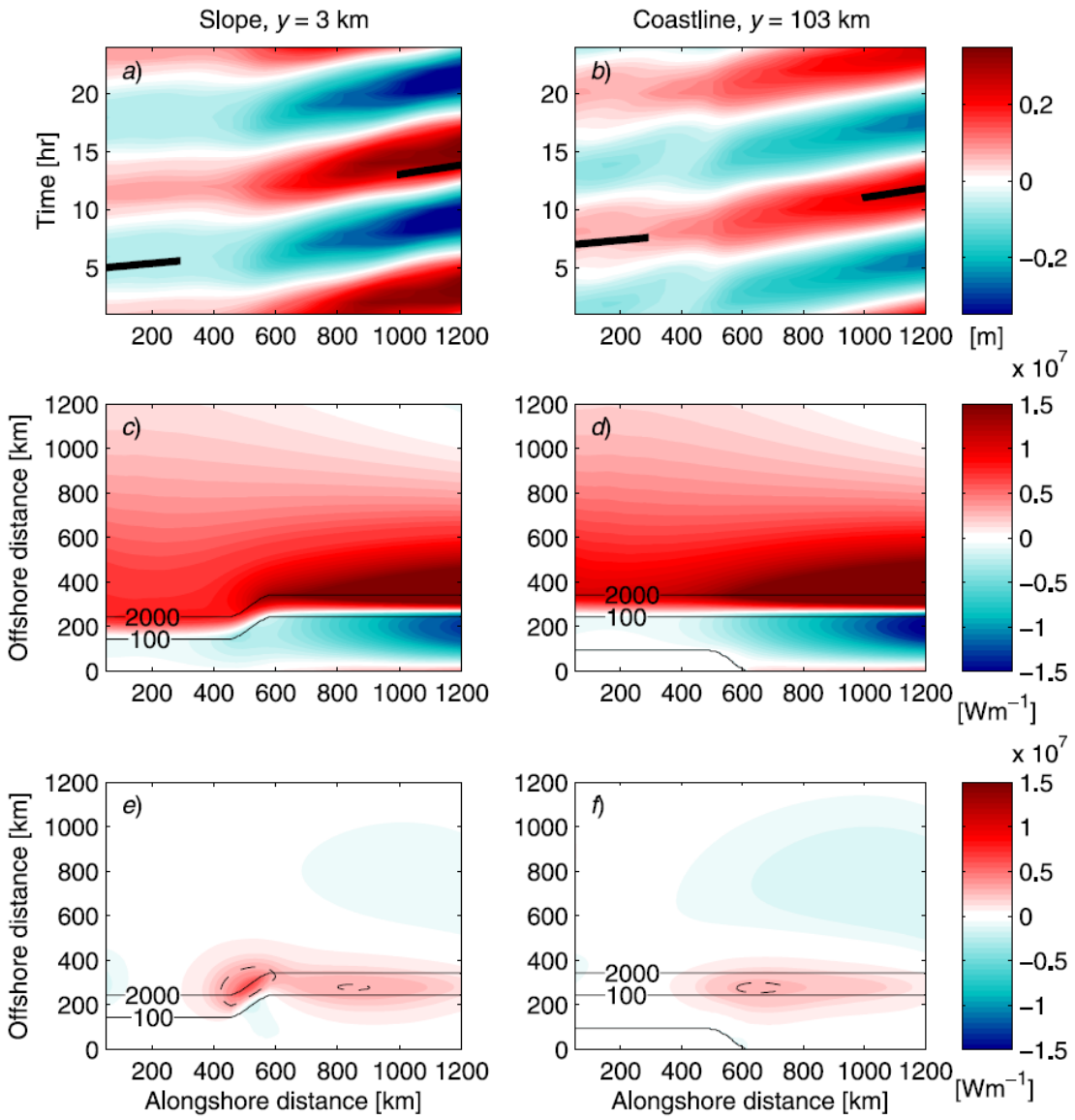

Figure 3.3 Numerical solution for the shelf width widening from 150 to 250 km by slope (left column) and by coastline (right column) averaged over 36 hr for a 12-hr wave period: temporal (shown over two wave periods) and alongshore free surface evolution at (a) y=3 km and (b) y=103 km, bold black line represents a theoretical phase speed of the semidiurnal zero mode (113.9 ms^{-1} for L_1=150 km and 69.4 ms^{-1} for L_1=250 km); alongshore component of the wave period-averaged energy flux (c, d); offshore component of the wave period-averaged energy flux (e, f). Energy flux contour shown as a dotted line is 0.3×10^7 Wm^{-1}.

with the wider shelf, and its absolute values increase (Figures 3.3c and 3.3d). On the shelf, the energy flux is negative but its magnitude increases over a wider shelf, in agreement with modal structures (Figure 3.2). This adjustment creates energy flux convergence on the shelf within the scattering region, which is released through the offshore energy flux at the shelf break and over the continental slope. Farther offshore in the downstream segment of the model domain ($400 < y < 1000$ km), the cross-shore energy flux is weakly negative (onshore) due to the compression of a modal structure closer to the coast on the wider shelf (Figures 3.3e and 3.3f).

Numerical experiments with a shelf narrowing from 250 to 150 km (Figure 3.4) can be viewed as mirror images of the previous cases, although the distortion of phase propagation (Figures 3.4a and 3.4b) in the scattering region is stronger than for the widening shelf. This result is somewhat surprising because a zero mode over the shelf with L_1=150 km has a higher phase speed and group velocity at the semidiurnal frequency compared to L_1=250 km (see dispersion diagram in Figure 3.1). The alongshore energy flux (Figures 3.4c and 3.4d) on the shelf now exhibits divergence, which is compensated by the onshore energy flux over the continental slope with its maximum values in the scattering region. In the upstream segment of the model domain, there is also a positive alongshore energy flux very near the coast, which is interrupted in the scattering region and produces the offshore energy flux there between the coastline and the shelfbreak (Figures 3.4e and 3.4f).

In the next pair of numerical experiments, the shelf widens from 250 to 300 km (Figure 3.5). The relative increase of the shelf width (which is 20%) in these cases is much smaller than in the first pair, when L_1 changes from 150 to 250 km (that is, by 67%). However, the

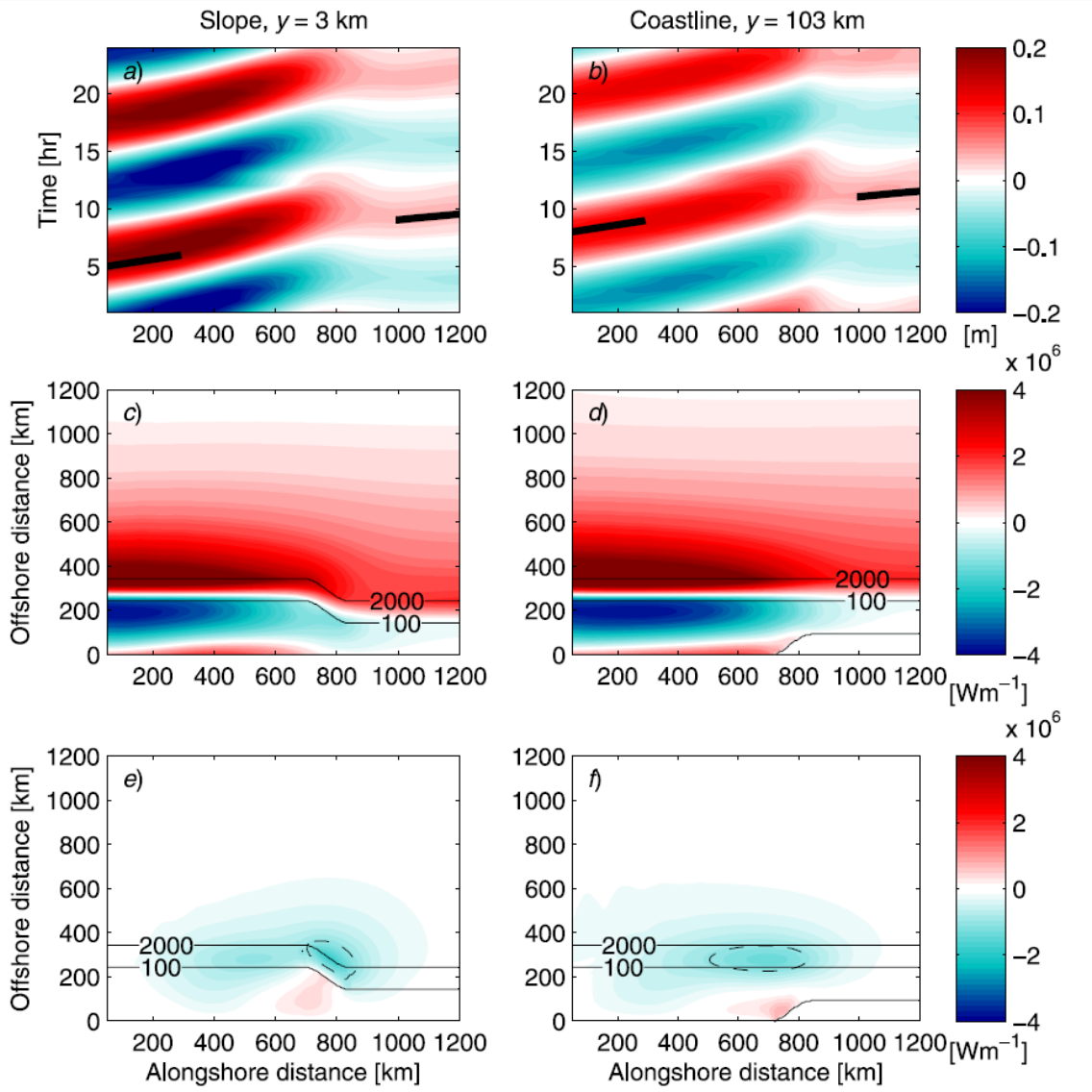

Figure 3.4 Same as in Figure 3.3 but for the shelf width narrowing from 250 to 150 km. Energy flux contour shown as a dotted line is -1×10^{6} Wm^{-1}.

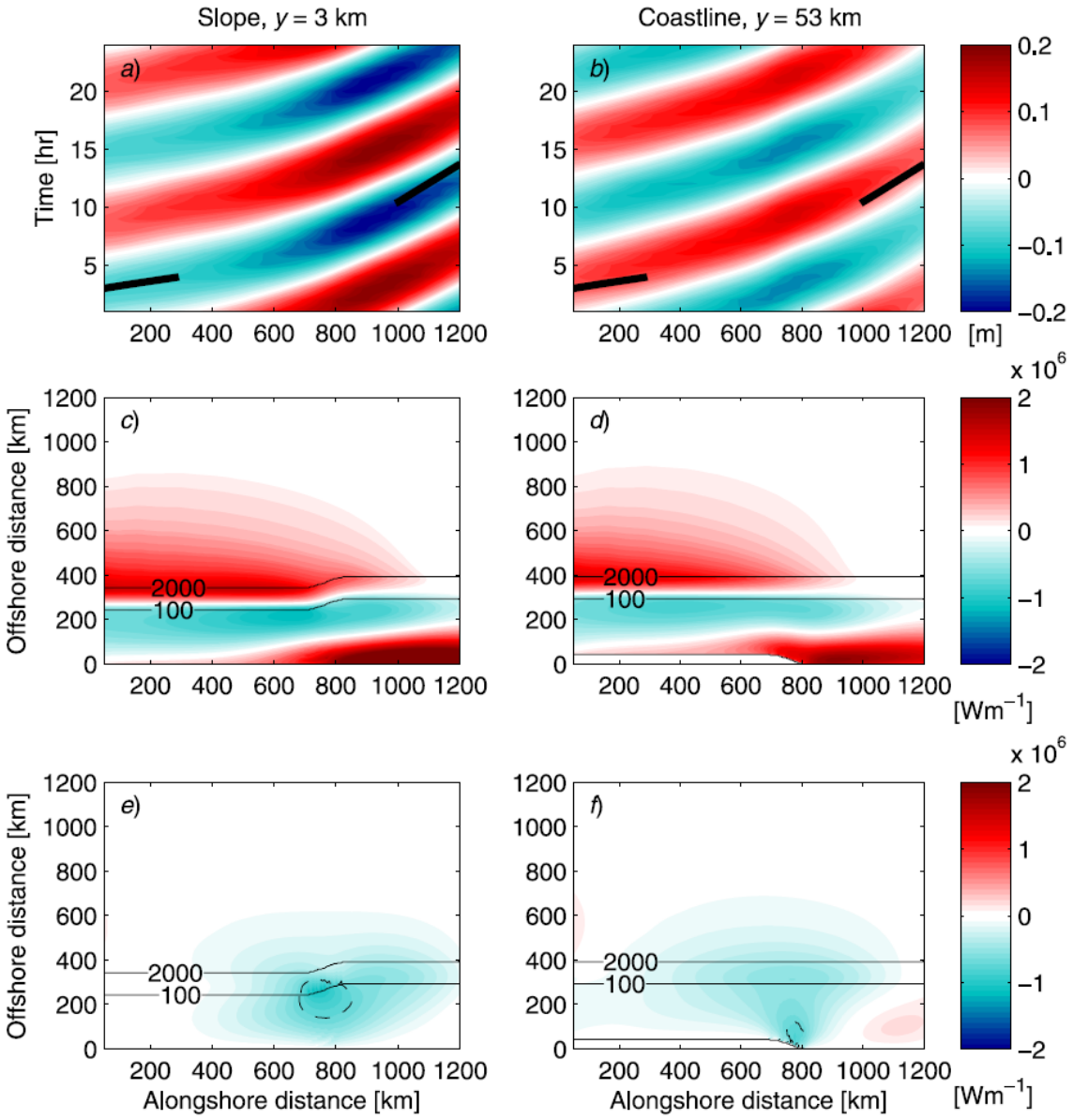

Figure 3.5 Same as in Figure 3.3 but for the shelf width widening from 250 to 300 km. The zero mode phase speed for L_1=300 km is 17.4 ms^{-1}. Energy flux contour shown as a dotted line is -0.7×10^6 Wm^{-1}.

group velocity of the semidiurnal zero mode attains a near-zero value for the shelf width between 250 and 300 km, which is evident from dispersion diagram in Figure 3.1a: for L_1 = 300 km, $C_g \approx 0$ is just below the semidiurnal frequency and the frequency of the minimal C_g increases with the decreasing shelf width. The zero group velocity can inhibit the alongshore propagation of the HKEW mode as described by Ke and Yankovsky (2010).

Phase propagation along the coast (Figures 3.5a and 3.5b) still shows a good agreement with the zero mode theoretical phase speed in the downstream segment of the model domain, indicating a relatively weak scattering into other propagating modes. However, the wave amplitude reaches its maximum value in the vicinity of the scattering region and not in the downstream segment. Hence, we infer that the evanescent component of the wave field responsible for this amplitude modulation is now larger than in previous cases.

It follows from the evaluation of alongshore energy flux structures (Figure 3.2) that the alongshore energy flux on the shelf should be divergent in the scattering region: the shelf energy flux is positive for L_1 = 300 km (downstream segment) and is negative for L_1 = 250 km (upstream segment). Numerical experiments confirm this pattern (Figures 3.5c and 3.5d); the alongshore divergence is compensated by the onshore energy flux across the continental shelf and slope in the vicinity of the scattering region. The magnitude of this onshore energy flux is now comparable with the alongshore energy flux on the shelf in the incident wave (Figures 3.5e and 3.5f).

The strongest scattering among the all cases presented occurs on the shelf narrowing from 300 to 250 km (Figure 3.6). The phase speed downstream of the scattering region clearly departs from its theoretical value, especially when the shelf narrows by

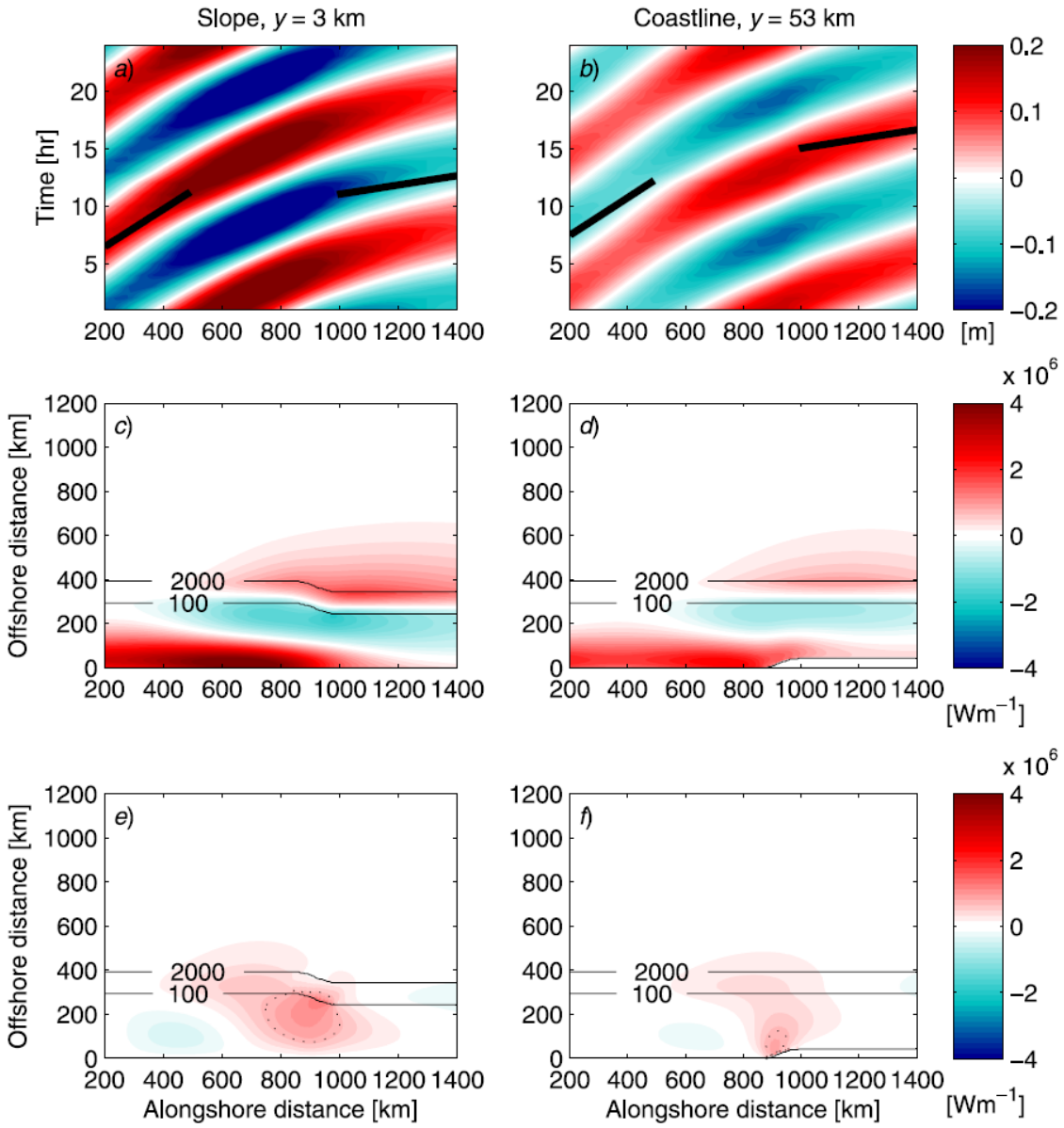

Figure 3.6 Same as in Figure 3.3 but for the shelf width narrowing from 300 to 250 km. Energy flux contour shown as a dotted line is 0.7×10^{6} Wm^{-1}.

coastline (Figure 3.6b), which indicates the presence of propagating modes other than the incident one (e.g. Wang 1980). The wave amplitude is modulated, reaching a maximum upstream of (Figure 3.6a) or at (Figure 3.6b) the scattering region. If only the incident mode were present, its amplitude would continuously decrease from the upstream to the downstream segment following the offshore spreading of the wave structure. The alongshore energy flux on the shelf is now convergent within the scattering region (Figures 3.6c and 3.6d) which produces a compensating energy flux offshore. The magnitude of this offshore energy flux is comparable to the alongshore energy flux on the shelf in the downstream segment (Figure 3.6c-3.6f).

We delineate the scattered wave field in the upstream segment (L_1=300 km) of the model domain in the two latter model runs as follows. We subtract the "instantaneous" modelled free surface field at the given time t^* of the averaged 12-hr wave cycle by the incident zero mode wave field with the same phase:

$$\eta_{res} = \eta_{model} - \eta_{ins} sin[kx - \omega(t^* + t_a)] \,, \tag{3.1}$$

where η_{ins} is the wave structure specified at the upstream boundary, t_a is the time when the 36-hr averaging starts, and the wave number *k* corresponds to the semidiurnal frequency in the dispersion diagram from Figure 3.1. The scattered wave field η_{res} for two time moments separated by a quarter of the wave period is shown in Figure 3.7. Wave perturbations radiating offshore from the continental shelf and slope are evident, especially for the narrowing by slope case (left panels in Figure 3.7). Indeed, the radiation in the narrowing by coastline case appears to occur at downstream of the scattering region (right panels in Figure 3.6): the phase speed is more distorted there and the alongshore energy flux structure in the downstream segment does not fit well the theoretical zero mode energy

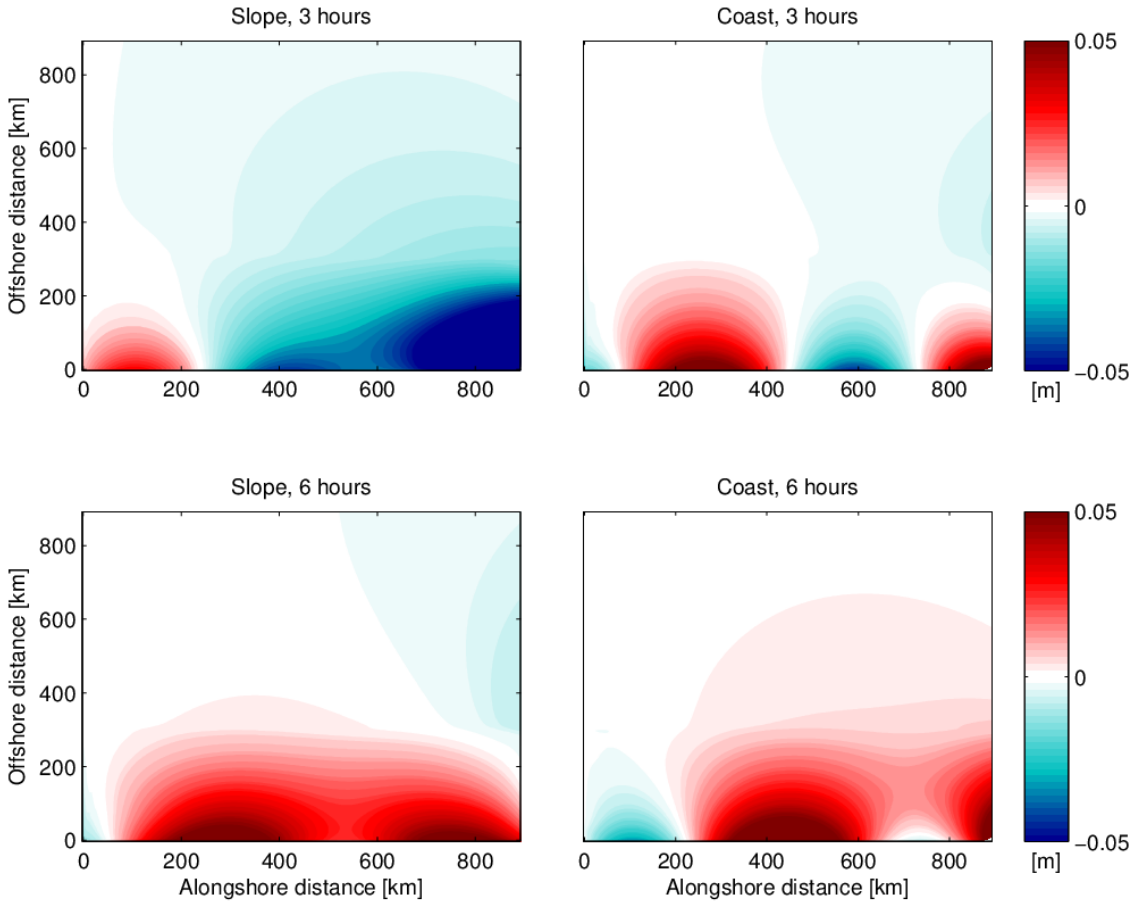

Figure 3.7 Instantaneous scattered wave filed (free surface perturbation), 3 hr (top) and 6 hr (bottom) for the averaged 12-hr wave cycle in the upstream segment of the model domain for the shelf narrowing from 300 to 250 km by slope (left column) and by coastline (right column).

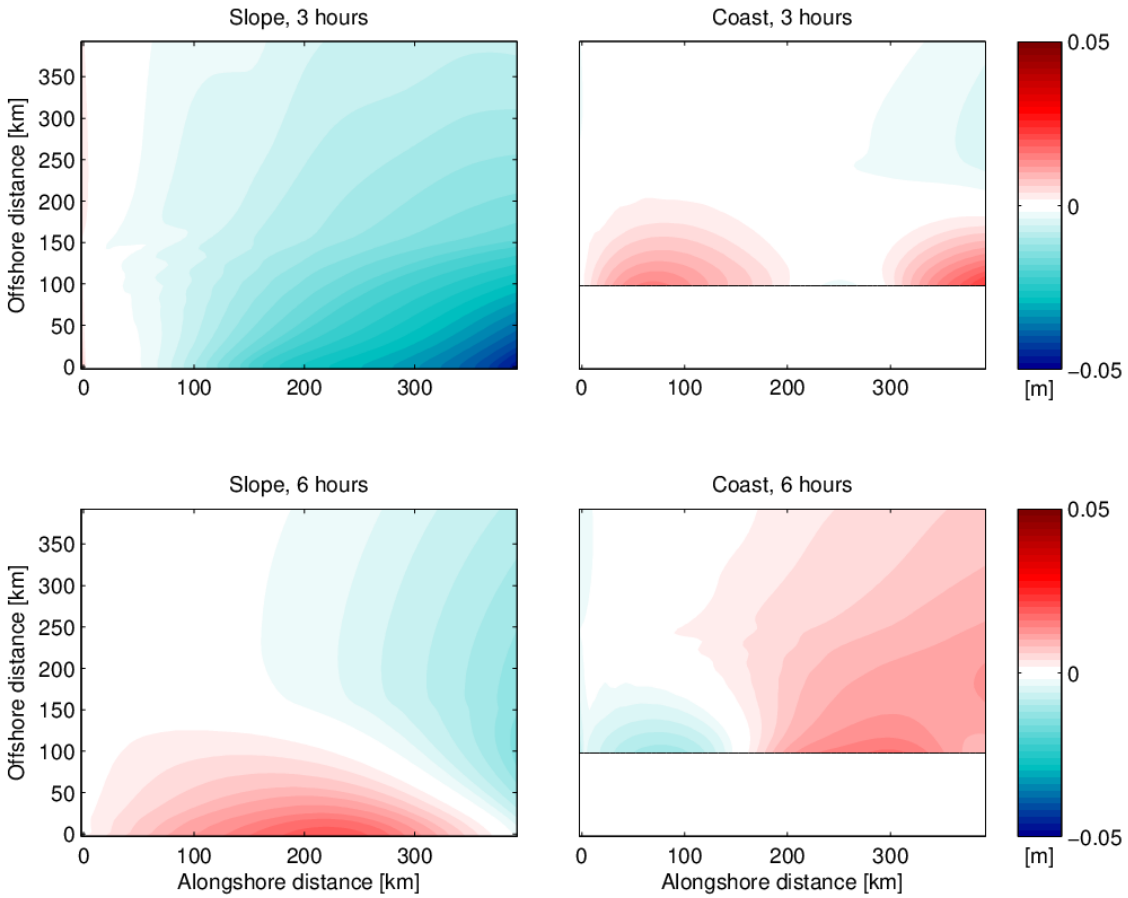

Figure 3.8 Same as in Figure 3.7 but for the shelf width widening from 150 to 250 km.

flux structure. Scattered wave fields of opposite phases (that is, separated by a 6-hr time interval) are not perfect mirror images (not shown), possibly because of some weak nonlinearity of the wave field resulting in the presence of multiple wave harmonics (sometimes referred to as overtides). The wave perturbation upstream on the shelf widening from 150 km to 250 km is also strong (Figure 3.8), indicating a scattered wave field existing upstream the scattering region.

In the last two numerical examples considered here, the deeper open ocean is specified (h_3 = 4000 m), and the shelf widens from 200 to 250 km over a 150 km alongshore distance (Figure 3.9). The results are qualitatively similar to the cases shown in Figure 3.3: the phase propagation is perturbed in the vicinity of the scattering region but otherwise follows the theoretical values of the zero mode both in upstream and downstream segments, and the alongshore energy flux is convergent on the shelf resulting in the offshore energy flux across the slope. The energy flux convergence follows from dispersion curves of the zero mode (Figure 3.1b): a semidiurnal wave has a lower C_g over a 250 km wide shelf compared to a 200 km wide shelf; as well as from the theoretical energy flux structure of semidiurnal waves over given depth profiles (not shown).

We quantify the adjustment and scattering of the incident modified Kelvin wave over the variable shelf width by introducing two non-dimensional parameters: the topographic energy flux divergence parameter D_e and the energy scattering coefficient S_e. D_e is defined based on the theoretical structure of the semidiurnal zero mode (Figure 3.2) as well as on the numerical model geometry (Figure 2.2):

$$D_e = \frac{\int_{coast}^{W} F_x^D dy - \int_{coast}^{W} F_x^U dy}{\int_{y=0}^{L} F_x dy} \frac{W}{X_D - X_U}, \tag{3.2}$$

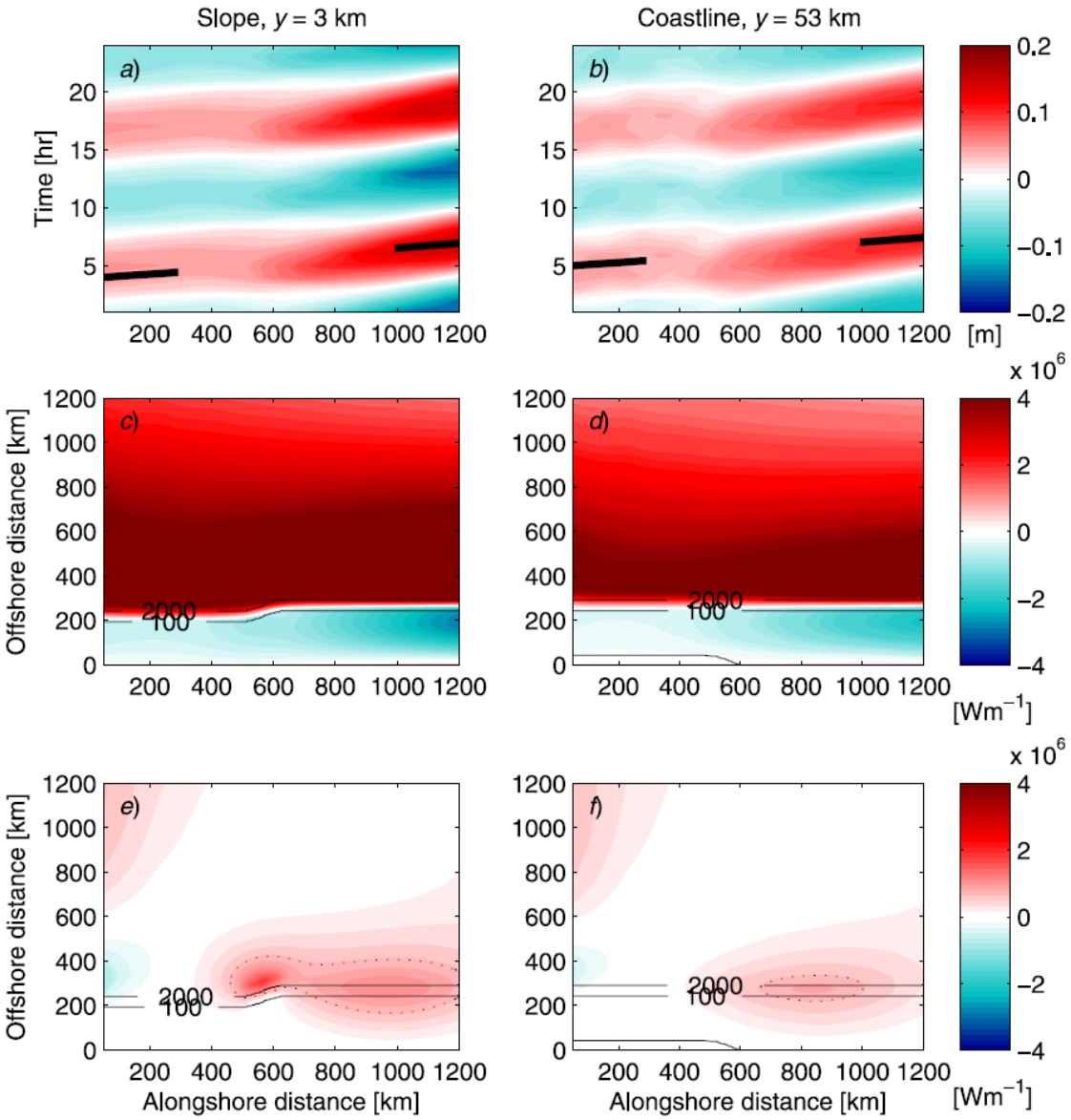

Figure 3.9 Same as in Figure 5 but for the shelf width widening from 200 to 250 km and h_3 = 4000 m. A theoretical phase speed of the semidiurnal zero mode is 159.6 ms^{-1} for L_1=200 km and 145.4 ms^{-1} for L_1=250 km; energy flux contour shown as a dotted line is 0.7×10^6 Wm^{-1}.

where F_x is the x component of the zero mode energy flux (2.3.45), W is the offshore extension of the wider continental shelf and slope topography (regardless of whether the shelf narrows or widens), indices D and U in the energy flux expression refer to the downstream and upstream depth profiles, respectively, and *coast* refers to the y coordinate of the coastline (which is not always zero when the shelf width changes by the coastline). The second term in (3.2) is the offshore/alongshore aspect ratio of the scattering region.

The energy fluxes for upstream and downstream depth profiles are normalized such that their integrals across the whole computational domain L are the same. This parameter shows the alongshore energy flux divergence over the variable topography as a fraction of the total alongshore energy flux in the zero mode normalized by the depth profile length scale W. It is expected that the magnitude of the cross-isobath energy flux should be proportional to D_e. It should also be noted that D_e has the same magnitude and opposite sign for symmetric changes of the shelf width (for example, widening vs. narrowing by continental slope) but it yields different values for the same change of the shelf width occurring by the coastline vs. the continental slope.

The second parameter is the scattering coefficient defined as a fraction of the incident wave energy flux radiated offshore as the incident wave mode propagates downstream past the scattering region:

$$S_e = \frac{\int_{coast}^{L} F_{x=300}\,dy - \int_{coast}^{L} F_{x=1200}\,dy}{\int_{coast}^{L} F_{x=300}\,dy}, \tag{3.3}$$

where the alongshore energy fluxes F_x are estimated at two cross-shore transects, at x = 300 km and x = 1200 km.

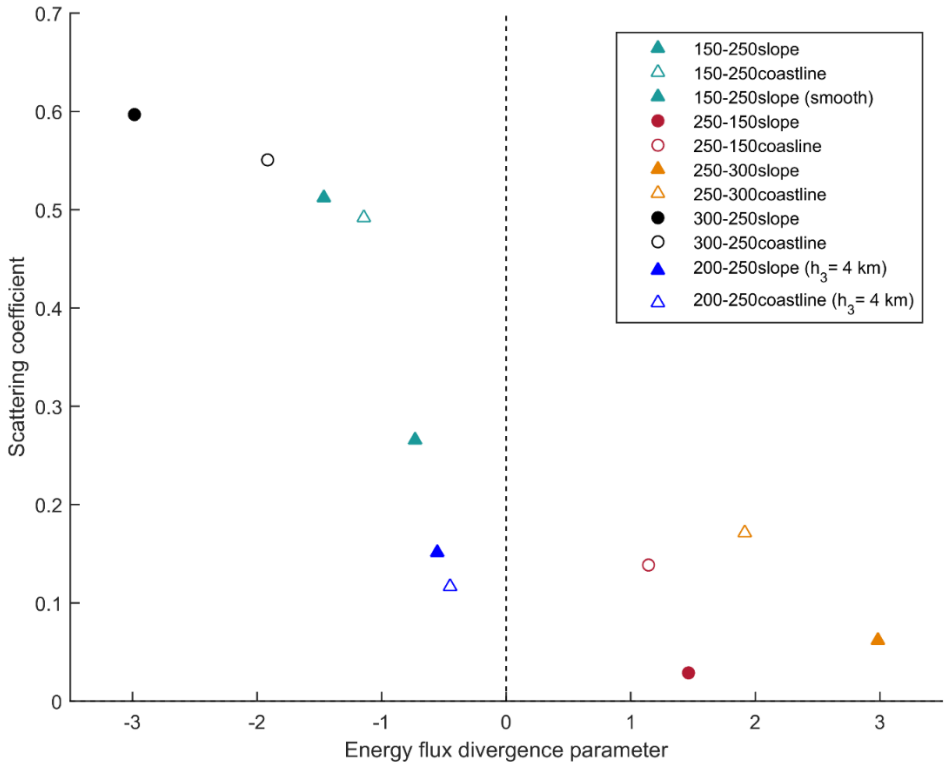

Figure 3.10 Scatterplot showing the scattering coefficient S_e as a function of the topographic energy flux divergence parameter D_e for all model runs; "smooth" in the legend refers to the 200 km long scattering region.

Figure 3.10 shows a scatterplot of S_e as a function of D_e for all model runs performed. When D_e is positive, the alongshore energy flux on the shelf is divergent and the compensating cross-isobath energy flux is toward the coast. In this situation there is relatively little scattering into radiating Poincaré waves, approximately 10-15% of the incident energy flux even if D_e exceeds 1. For the negative values of D_e (convergent alongshore energy flux), the situation changes drastically and S_e rapidly increases with the magnitude of D_e. When D_e becomes less than -1, approximately 50% or more of the incident wave energy flux radiates offshore.

Apart from the strength of scattering, the energy flux divergence parameter appears to capture well the generation of cross-isobath energy fluxes in the vicinity of the scattering region. For instance, cases with 250-300 km shelves have higher absolute values of D_e, and the cross-isobath energy fluxes in these cases are also higher (when compared against the corresponding alongshore energy flux) than for shelf width changes of 150-250 km. Also, for 250-300 km shelves, a higher absolute value of D_e corresponds to the shelf width changing by the slope, and these cases (both widening and narrowing shelf) indeed have stronger cross-isobath energy fluxes over the slope compared to the corresponding cases with the shelf width changing by the coastline. The two model runs with h_3 = 4000 m represent a relatively modest topographic irregularity (in terms of D_e), but their scattering coefficients (Figure 3.10 in blue) are well aligned with other cases, where h_3 = 2000 m is utilized.

3.3 DISCUSSION AND CONCLUSIONS

Properties of a barotropic semidiurnal Kelvin wave are modified on wide continental shelves such that the energy flux on the shelf can reverse relative to the phase

propagation and that the wave structure becomes progressively more confined over the shelf and slope topography as the shelf width increases. When a modified semidiurnal Kelvin wave encounters a narrowing or widening continental shelf, a cross-isobath energy flux over the shelf break and continental slope is generated. This cross-isobath energy flux can be deduced from the comparison of shelf energy flux structures in the fundamental zero mode upstream and downstream of the variable shelf width. The type of shelf width change by itself (narrowing vs. widening shelf) cannot define unambiguously the direction of cross-isobath energy flux (onshore vs. offshore). For instance, when the shelf narrows from 250 to 150-km wide, the cross-isobath energy flux is onshore, while for 300 to 250 km shelf width transition, the energy flux is offshore. On the other hand, linking energy flux modal structures (Fig. 3) for upstream and downstream depth profiles can predict whether the alongshore energy flux will be convergent or divergent over a shelf with variable width.

The magnitude of the cross-isobath energy flux referenced to the incident wave energy flux is not simply proportional to the magnitude of topographic irregularities, e.g., shelf widths of 250-300 km produce relatively stronger cross-isobath energy fluxes than stronger shelf width changes of 150-250 km. This feature can be explained by the incident wave scattering into other wave modes. The scattered wave field has two components: evanescent and propagating. The evanescent part is trapped at the scattering region and decays both downstream and upstream. It is evident in the wave amplitude and phase speed modulation in the vicinity of the scattering region. In some cases, propagating modes radiating energy offshore are also generated. This offshore energy radiation is consistent with the analytical solution by Pinsent (1972), who showed that a Kelvin wave leaks energy

offshore (through Poincaré waves) when it encounters coastline irregularities. The presence of Poincaré waves in our cases is evident in the departure of phase speed from its theoretical value for the fundamental zero mode in the downstream segment of the model domain (e.g., narrowing shelf from 300 to 250 km), and in the decrease of the alongshore energy flux integrated across the entire numerical domain.

The magnitude of the cross-isobath energy flux in the vicinity of the scattering region depends on the alongshore energy flux divergence on the shelf. Relatively stronger cross-isobath energy fluxes (when compared to the incident energy flux) observed between 250 and 300 km wide shelves are most likely related to the near-zero C_g occurring in the scattering region. Zero group velocity implies that in the cross-shore wave structure, the downstream (in the direction of phase propagation) and the upstream energy flux components are equal so that their cross-shore integral is zero. Hence, a near zero group velocity can be a good indicator of strongly convergent (divergent) alongshore energy flux on the shelf in the scattering region, when the downstream energy flux branch shifts offshore (onshore) between the upstream and downstream segments of shelf topography.

Propagation of the modified semidiurnal Kelvin wave on wide shelves when it is transformed into an HKEW mode can contribute to internal tide generation over the continental slope. Internal waves can be generated directly by cross-isobath currents associated with offshore/onshore energy fluxes discussed in this study. Also, the HKEW mode scattering into radiating (non-trapped) modes can be more efficient when the water column is stratified and the internal wave modes are also present. Due to their lower phase speed and smaller spatial scales, internal waves can be more readily available to provide an adjustment of the incident HKEW mode to topographic irregularities with an alongshore

spatial scale of O(100 km). Indeed, Pinsent (1972) found that the strongest scattering of the incident Kelvin wave into Poincaré modes occurs when the wavelength of radiating waves is comparable with the length of coastline features. Energy exchange between the internal wave modes crossing the continental slope and the edge waves trapped on the shelf was studied by Chapman (1984), although in that case the energy transfer occurred from a baroclinic to barotropic mode.

This chapter focus on the barotropic response of the semidiurnal tides, which is the most energetic tidal species in the World Ocean. In a striking contrast to the analytical solution, the real-ocean barotropic semidiurnal Kelvin waves can induce strong cross-isobath energy fluxes when they are modified by continental shelf topography. On wide shelves the zero mode wave structure at semidiurnal frequency is confined within the area of variable depth with only a small extension into the open ocean of a constant depth. Consequently, the alongshore energy flux becomes highly sensitive to the shelf geometry and has to adjust to the shelf width as it changes alongshore. This adjustment results in the divergent alongshore energy flux on the shelf with compensating cross-isobath energy fluxes farther offshore, across the shelf break and continental slope. Once the shelf width is sufficiently large to convert a Kelvin wave into the HKEW mode, even modest changes of the shelf width can trigger substantial cross-isobath energy fluxes comparable to the shelf energy flux in the incident wave.

In addition to the zero mode adjustment, cross-isobath energy fluxes can be triggered by the incident wave mode scattering into other wave modes available at a semi-diurnal frequency. Dispersion characteristics of the zero mode determine the strength of scattering. Particularly favorable conditions for the wave scattering into radiating offshore

modes occur when the energy flux divergence parameter D_e is -1 or less. However, there is a clear mismatch between the spatial scales of barotropic Poincaré waves (thousands of km) and topographic irregularities (tens to hundreds of km). Under stratified conditions, the full set of long wave modes is complemented by baroclinic Poincaré waves with much smaller spatial scales comparable to the length scales of alongshore topographic irregularities. This indicates a possibility of intense scattering of the barotropic semidiurnal zero mode during the adjustment to the variable shelf width under stratified flow conditions, which is investigated in the next chapter.

.

CHAPTER 4

MODELING THE INTERNAL WAVE GENERATION BY THE SCATTERING OF HKEW

The barotropic model in the previous chapter shows that when a zero mode HKEW encounters a change in shelf width, the corresponding adjustment of its wave structure can lead to the substantial cross-isobath energy flux. Potentially this can result in generation of internal waves. This chapter focuses on numerical models of the HKEW over wide continental shelves in stratified water. A normalized baroclinic energy flux is calculated for each model run to compare the intensity of baroclinic radiation from the scattering region in different model runs. Model results show that the internal wave radiation can occur when there is a divergence in the alongshore barotropic energy fluxes on the shelf. A convergence in the alongshore barotropic energy fluxes produces less baroclinic energy radiation, possibly due to existence of strong barotropic radiation reported in the previous chapter. Comparisons between each model run show that the structure of internal wave fields depends on the relation between internal wave mode structures and barotropic forcing. The strength of the internal wave generation depends on several factors, including the internal wave modes available for scattering, the matching between the internal wave mode structure and the barotropic forcing, and the steepness of the shelf slope downstream the scattering region. Under favorable conditions, more than 10% of the incident barotropic energy can be scattered to baroclinic energy radiation.

4.1 DISPERSION RELATIONS AND INTERNAL WAVE MODE STRUCTURES

The set of model topographies used in this model is the same as in the previous chapter. As Chapter 3 shows, only the fundamental zero mode exists at the semidiurnal frequency, and the other wave modes merge with the continuum of Poincaré waves. The dispersion diagram (Figure 4.1) for the two shelf widths shows the fundamental zero mode for the set of shelf widths used in this model. For L_1 = 150 km, the semidiurnal zero mode resembles a Kelvin wave with a phase speed close to $\sqrt{gh_3}$. Its offshore structure of free surface perturbation extends to more than 2000 km (Figure 4.2a). For L_1 = 300 km, the semidiurnal zero mode becomes an HKEW with a much slower phase speed. Its free surface perturbation is confined within the continental shelf (Figure 4.2a).

Same as the wave structures in Chapter 3, the velocity component u changes sign at the shelf break. For L_1 = 150 km, u is mostly negative on the shelf, while for L_1 = 300 km, u is mostly positive on the shelf (Figure 4.2b). To compare the alongshore energy fluxes, a total energy flux is obtained by integrating the alongshore energy flux over the cross-shore distance and normalizing the energy flux so that the total energy fluxes are equal. The normalized alongshore energy fluxes are shown in Figure 4.2c. For L_1 = 150 km, the energy flux on the shelf is negative, and gradually increases to a positive maximum at the foot of the continental slope. For L_1 = 300 km, the energy flux is mostly confined on the shelf. When the shelf width L_1 changes alongshore, the alongshore energy fluxes on the shelf will change sign and induce strong cross-isobath energy fluxes over the continental slope. For example, when the wave propagates from the narrow shelf (L_1 = 150 km) to the wide shelf (L_1 = 300 km), the wave amplitude near coast is amplified due to the concentrated energy flux on the continental shelf, and a divergence in alongshore energy

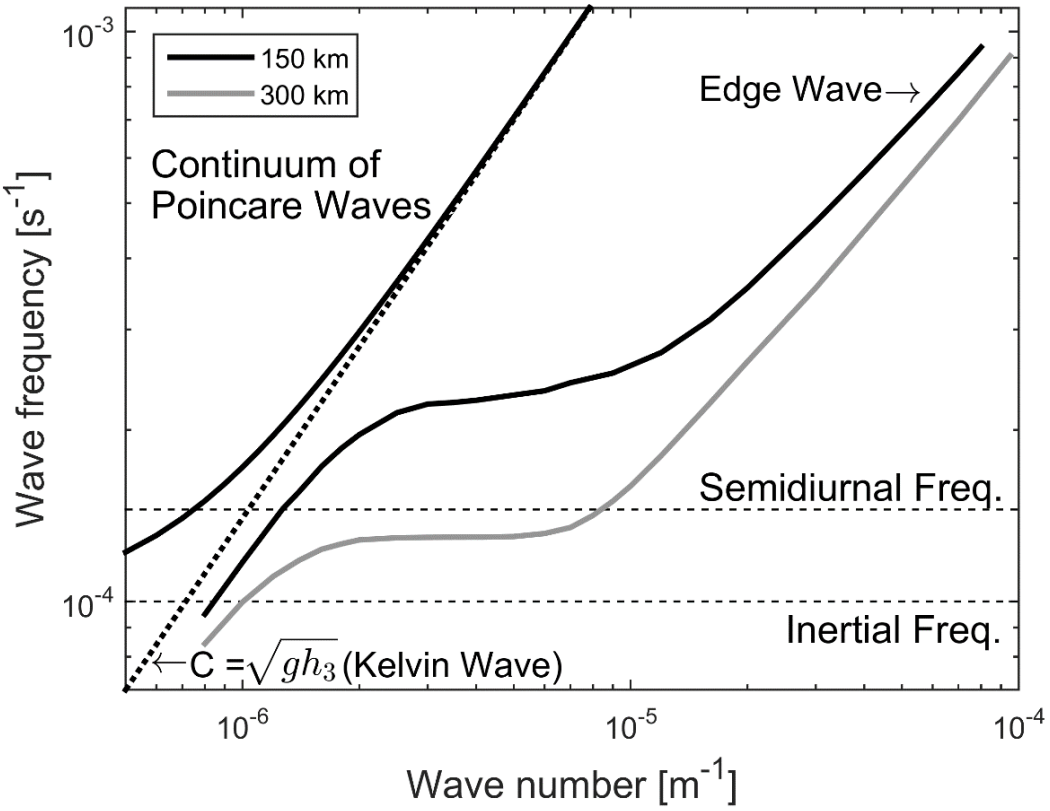

Figure 4.1 Dispersion curves for a zero Kelvin edge wave mode for L_1 = 150 (black) and 300 km (gray).

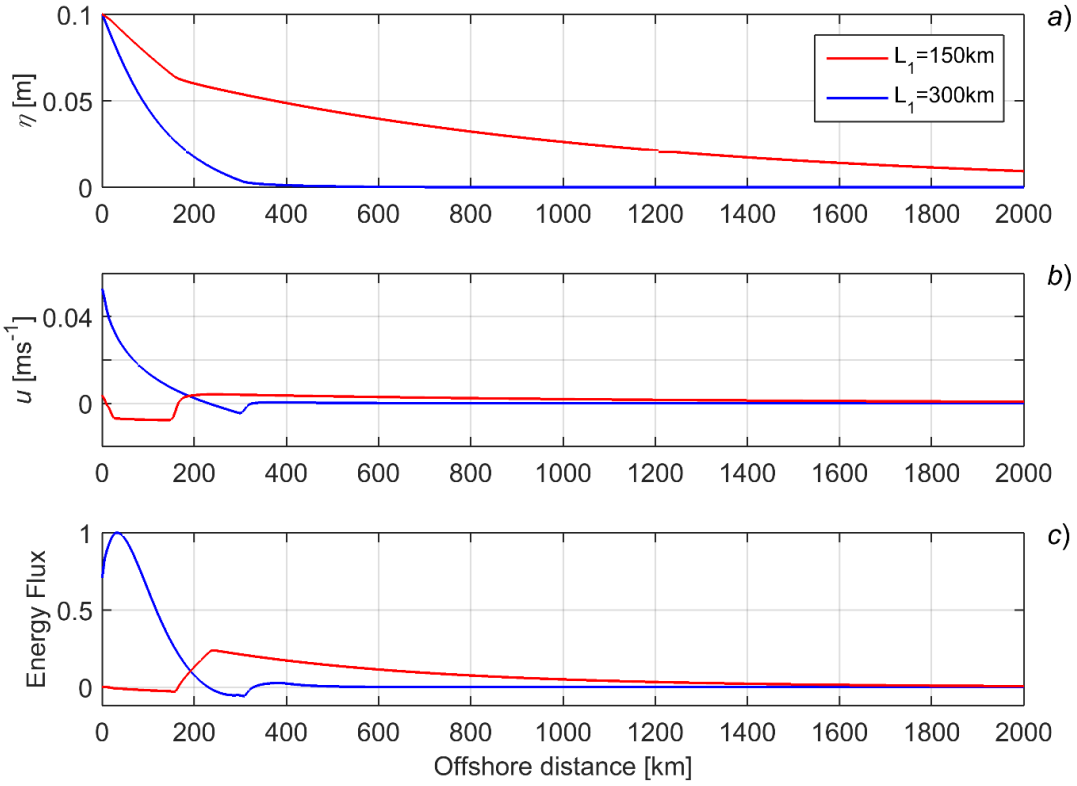

Figure 4.2 Wave structures for h_3 = 2000 m: (a) Cross-shore free surface structure of the semidiurnal wave modes; (b) alongshore velocity of the wave modes; and (c) normalized alongshore energy flux for L_1 = 150 and 300 km.

fluxes will occur, resulting in an onshore energy flux. When the wave propagates from the wide shelf (L_1 = 300 km) to the narrow shelf (L_1 = 150 km), the wave amplitude will decrease, and a convergence in alongshore energy fluxes will occur, resulting in an offshore energy flux.

The free surface structures for cases with h_3 = 4000 m are comparable to h_3 = 2000 m, with a relatively more diverse alongshore energy structure off the continental slope for the 300 km wide shelf (Figure 4.3c). This suggests that when the shelf width changes, the convergence or divergence of alongshore energy fluxes for cases with h_3 = 4000 m should be stronger than for h_3 = 2000 m.

For model runs with h_3 = 2000 m, three types of stratifications are specified: density profiles with linear increase of 2 kg/m^3 and 6 kg/m^3 from top to bottom (*l2* and *l6*), and a surface intensified density profile with a 2 kg/m^3 increase from top to bottom (*s2*). For the h_3 = 4000 m cases, a linear stratification with a 4 kg/m^3 increase (*l4*) and a surface intensified stratification with a 3 kg/m^3 increase (*s3*) are specified. The buoyancy profiles and the structures of the internal wave vertical velocity for all 5 density profiles are shown in Figure 4.4. The linear stratifications (*l2*, *l4*, and *l6*) have uniform buoyancy profiles (Figure 4.4a), hence the maximum of *w* for the first mode occurs in the middle of the water column (Figure 4.4b). For the *s2* stratification (Figure 4.4c), the first mode has a maximum *w* near the top of water column, whereas the second and the third mode have maximums at much deeper depths. For the *s3* stratification however, the pycnocline occur at a relatively small fraction of the entire water depth (Figure 4.4a) compared to the *s2* stratification. Consequently, the surface intensification has a lesser impact over the vertical profile of *w*, and the maximum of *w* for the first mode occurs near the middle of the water column. The

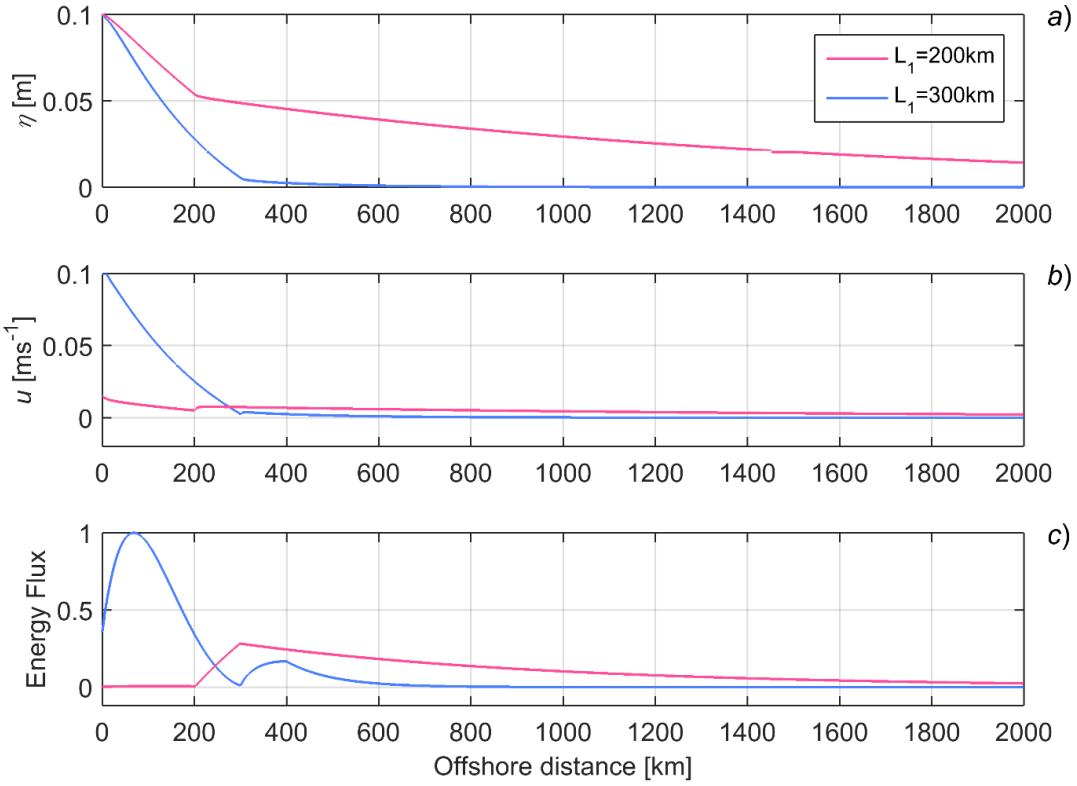

Figure 4.3 Wave structures for h_3 = 4000 m: (a) Cross-shore free surface structure of the semidiurnal wave modes; (b) alongshore velocity of the wave modes; and (c) normalized alongshore energy flux for L_1 = 200 and 300 km.

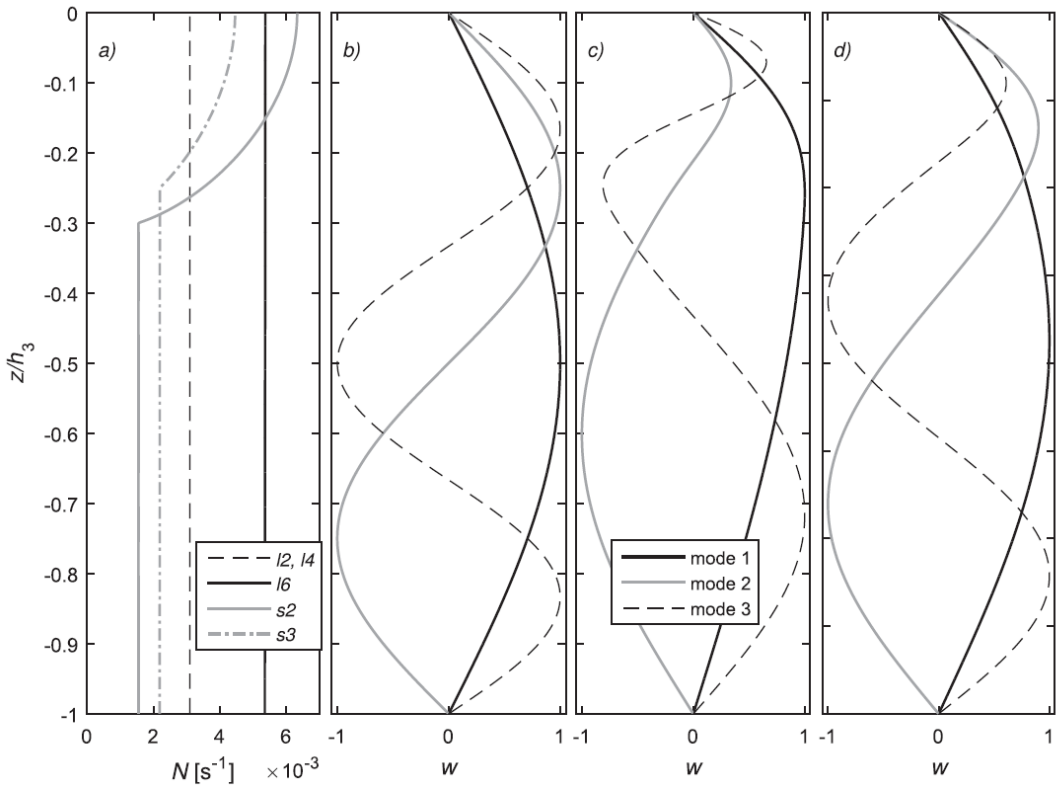

Figure 4.4 Buoyancy frequency (a) and internal wave modes for all density profiles. The vertical velocity mode 1-3 structures are shown for (b) *l2*, *l4*, and *l6*; (c) *s2*; and (d) *s3*.

horizontal velocity structures are calculated from the vertical velocity component *w* as described in Chapter 2 (2.10).

The analytical HKEW structures show that the reversal of alongshore energy fluxes and velocities occur on the shelf. This indicates that the barotropic forcing for internal wave generation is concentrated in the upper part of the continental slope. For the model runs with linear and surface intensified density profiles, different internal wave modes will match the barotropic forcing, depending on whether the first or the higher wave modes have a maximum of *w* at the upper depth near the strongest barotropic forcing.

4.2 BAROTROPIC RESPONSE

The barotropic responses for the stratified model cases are comparable to the barotropic model. For the cases of the continental shelf widening by slope with L_2 = 100 km (model run 1-3), all three stratifications (*l2*, *l6*, and *s2*) produce a similar barotropic solution. Hence, only the *l2* stratification (Figure 4.5) is shown to demonstrate the barotropic response. The phase propagation over the shelf at upstream and downstream segments of topography is in good agreement with the theoretical phase speed (shown as black lines in Figure 4.5a). At the scattering region between 500 km and 1300 km alongshore, the wave amplitude increases, suggesting that the incident wave scatters into other wave modes. The instantaneous wave field η (Figure 4.5b) is in agreement with the theoretical mode structure of the HKEW (Figure 4.2a). The free surface becomes confined on the continental shelf when the shelf widens. The alongshore energy flux also agrees with the theoretical structure in Figure 4.2c. On the continental shelf, the alongshore energy flux is negative upstream and positive downstream of the scattering region, resulting in a

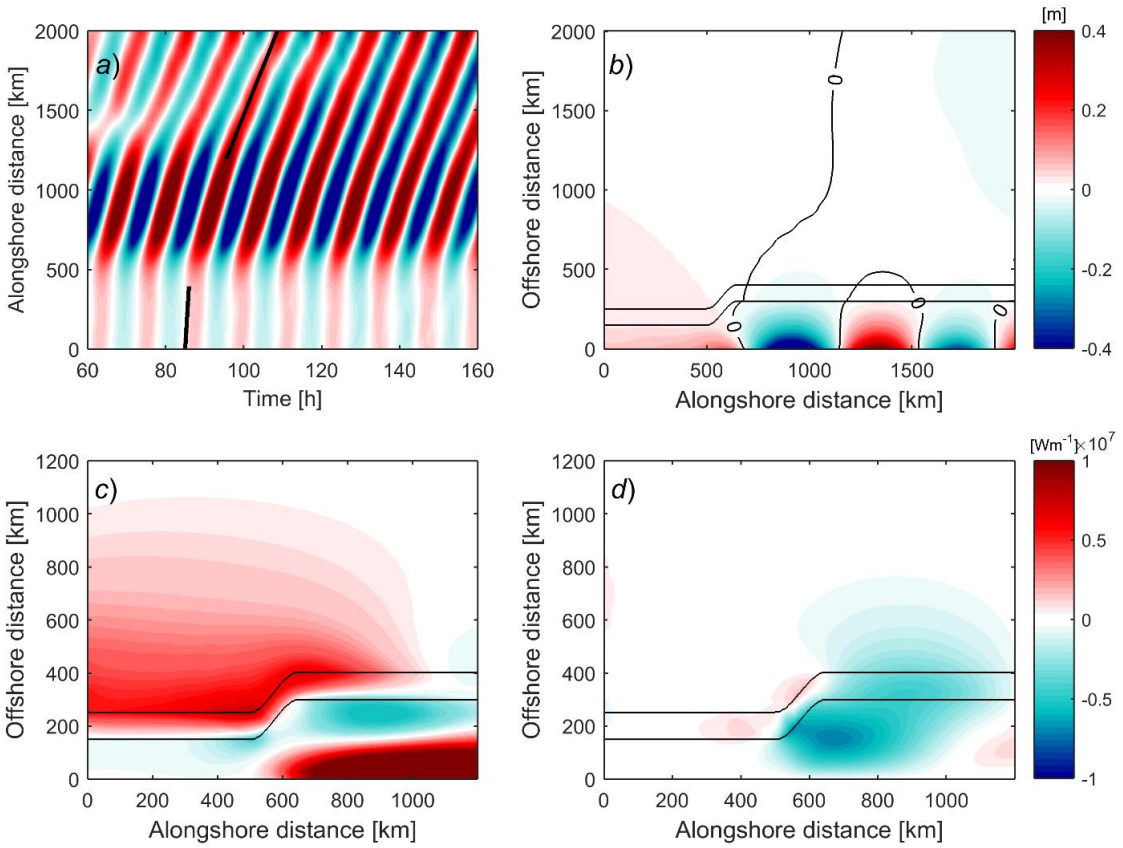

Figure 4.5 Barotropic response of model run 1 (widening by slope with *l2* stratification): (a) free-surface evolution along the coastline, bold black line represents a theoretical phase speed of the semidiurnal zero mode (113.9 ms^{-1} for L_1=150 km and 17.4 ms^{-1} for L_1=300 km); (b) instantaneous wave field η at t = 135 h. (c) alongshore barotropic energy flux; and (d) cross-shore barotropic energy flux.

divergence within the scattering region (Figure 4.5c). This divergence is compensated by a strong inshore energy flux (Figure 4.5d) which magnitude is comparable to the alongshore energy flux.

The *l2* stratification only yields a slightly stronger barotropic energy fluxes than the *l6* and *s2* stratification. For comparison, a barotropic energy flux residual defined by the difference between the other two configurations and the *l2* stratification is shown in Figure 4.6. Since the incident barotropic energy fluxes remain the same for all 3 model runs, we focus on the energy fluxes near the scattering region. When the linear stratification is intensified (*l6*), the total amount of barotropic energy fluxes downstream the scattering region becomes slightly weaker than the *l2* stratification. On the wider shelf, there are less alongshore energy flux propagating downstream (Figure 4.6a), and consequently, the positive residue of the cross-shore barotropic energy fluxes (Figure 4.6b) shows that there are less inshore energy flux near the scattering region. This result indicates a stronger barotropic to baroclinic energy conversion when the stratification is intensified. The barotropic energy fluxes of the model run 3 (*s2* stratification) is closer to model run 1 (*l2*). In this model run, the weakening of the barotropic energy flux on the wider shelf occurs downstream the scattering region at approximately 1000 km (Figures 4.6c and 4.6d). The energy flux residue shows a scattered wave field extend to more than 600 km downstream of the scattering region, indicating the existence of different internal wave modes in these two model runs.

Model runs 4 and 5 (widening by a coastline with *l6* and *s2* stratification) produce a similar barotropic response. The phase propagation and the free surface structure are all

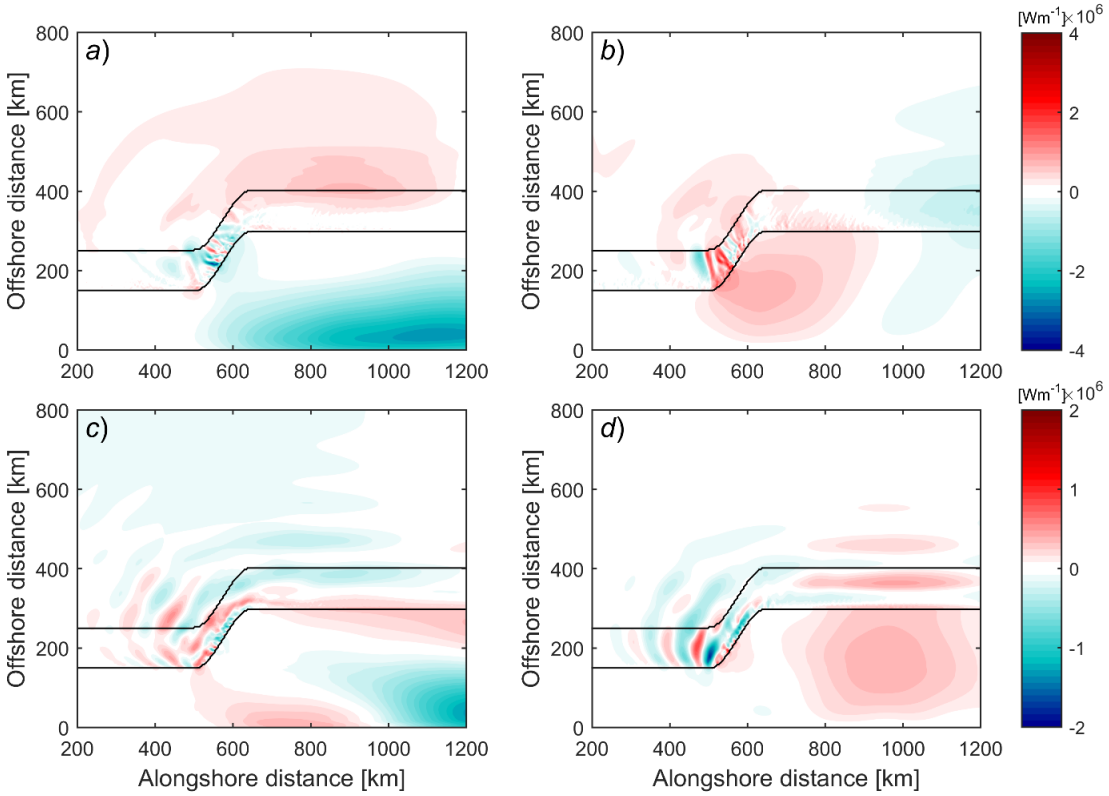

Figure 4.6 Barotropic energy flux residues. The top panels shows the residual of alongshore (a) and cross-shore (b) energy fluxes between *l6* and *l2*. The bottom panels show the residue of alongshore (c) and cross-shore (d) energy fluxes between *s2* and *l2*.

in good agreement with the theoretical structures at upstream and downstream region. As was observed in the barotropic models in Chapter 3, for the widening by coastline cases, the strongest cross-shore barotropic energy flux occurs at the scattering region, and extend downstream for 500 km. The magnitude of this cross-shore barotropic energy flux is comparable to the strongest alongshore energy fluxes confined on the wide shelf. These barotropic results are similar to the previous cases and thus are not shown.

The barotropic responses of model runs with narrowing shelf show a strong convergence of the alongshore energy flux over the shelf at the scattering region (e.g., Figure 4.7). The phase propagation for model run 4 (narrowing by slope with *l6* stratification) along the coastline shows that the free surface η increases upstream of the scattering region, suggesting that other wave modes exist there. The phase speed uptream and downstream of the scattering region is still in good agreement with the theoretical phase speed of the zero mode. The convergence in the alongshore barotropic energy flux leads to an offshore barotropic energy flux at the scattering region. Instead of extending downstream of the scattering region as in widening cases, the offshore energy flux occurs upstream and within the scattering region.

For model run 17 (h_3 = 4000 m with *s3* stratification), the barotropic results show stronger free surface amplification at the scattering region (Figure 4.8a). The phase propagation upstream and downstream the scattering region is in agreement with the theoretical phase speed, but the build up of free surface amplitude at x = 500-1000 km shows that the scattering is stronger in the h_3 = 4000 m cases. The alongshore barotropic energy flux agrees with the theoretical structure of the semidiurnal zero mode, however, the adjustment of wave structure results in a strong upstream energy flux at x = 600-1200

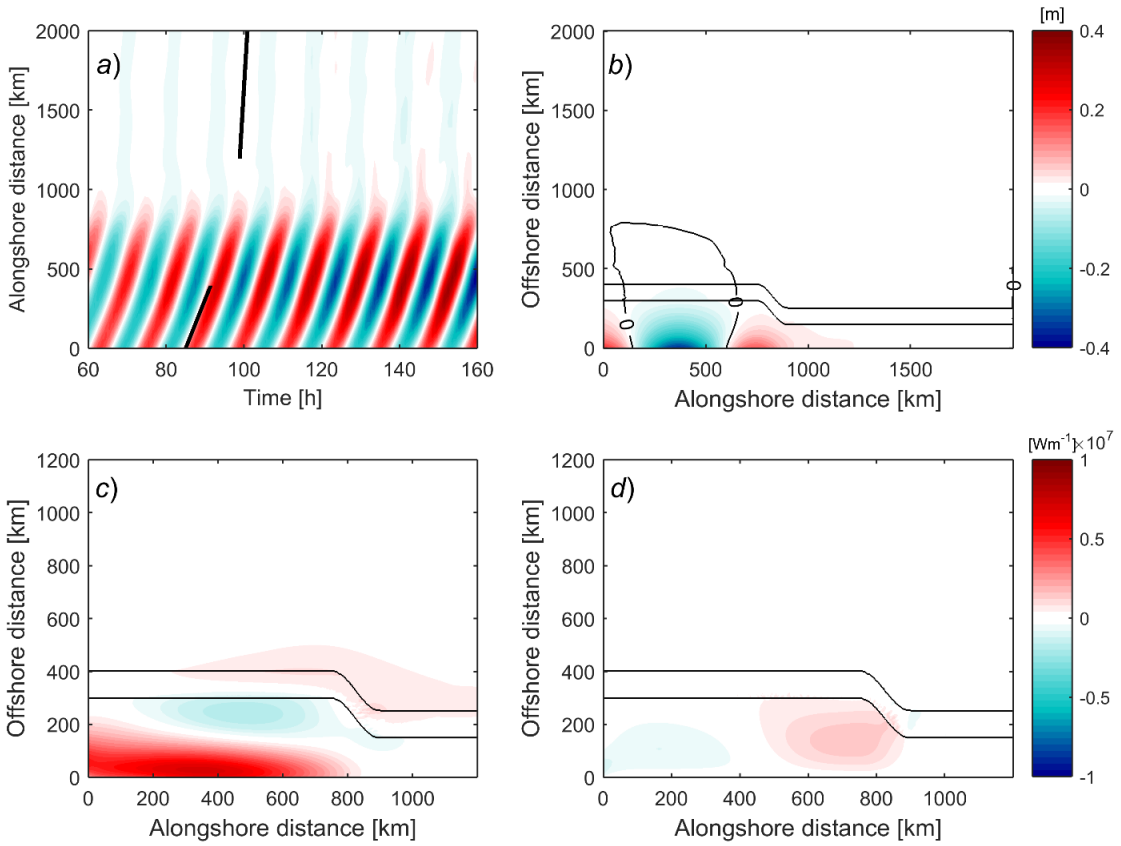

Figure 4.7 Same as in Figure 4.5 but for model run 19 (narrowing by slope with *l6* stratification).

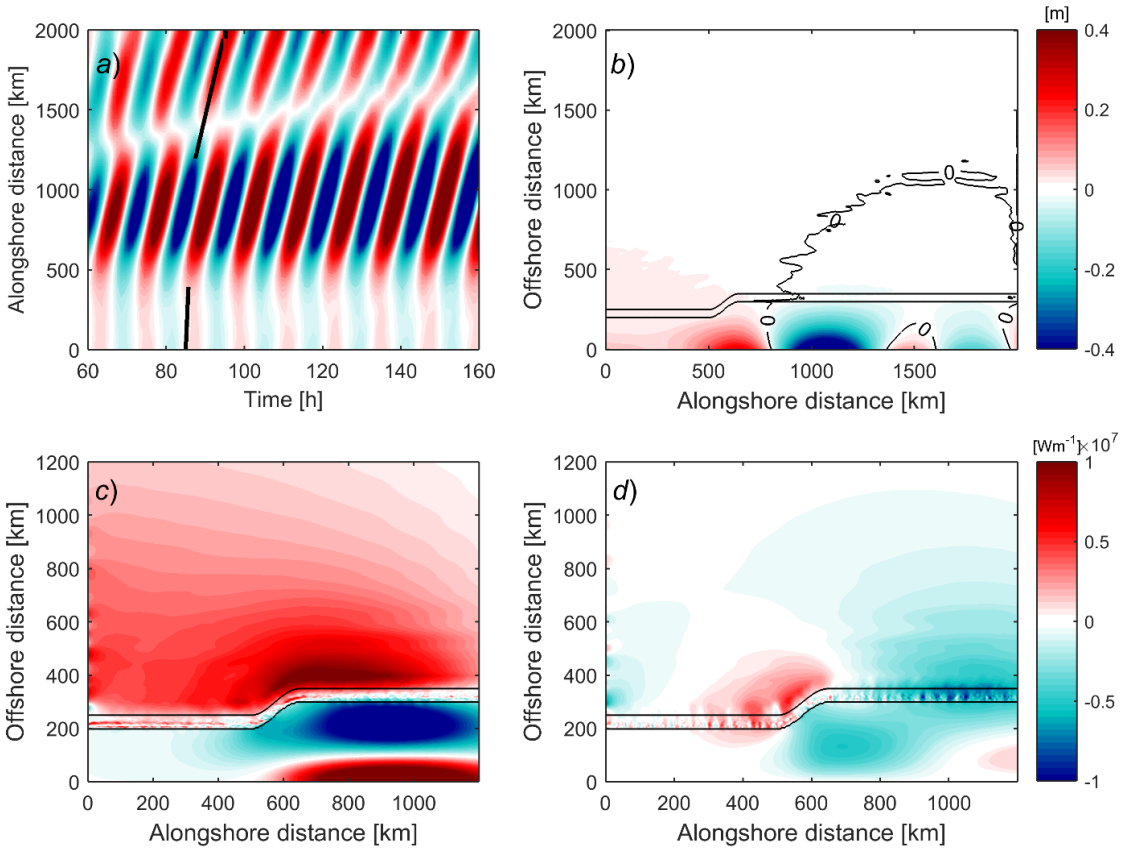

Figure 4.8 Same as in Figure 4.5 but for model run 17 (h_3 = 4000 m with *s3* stratification).

km. This results in a much stronger inshore energy flux and extend further offshore comparing to the h_3 = 2000 m cases.

4.3 BAROCLINIC RESPONSE

The adjustment of the HKEW mode structure results in scattering of the barotropic wave mode into baroclinic wave modes. Since the total energy does not decompose into individual wave modes (Huthnance 1978), we look at the baroclinic energy fluxes as an indicator of the strength of scattering. To examine the evolution of the models' energy fluxes, diagnostics of energy fluxes are calculated as energy fluxes entering and exiting the scattering region. The scattering region is defined by transects A, B, and C in Figure 4.9. For the narrowing shelves, transect A is at x = 600 km; transect B is at x = 1200 km; and transect C is at y = 450 km. For the widening shelves, transect A is at x = 400 km; transect B is at x = 1000 km; and transect C is at y = 450 km. The sampling interval of the energy flux is 1 h, and all energy fluxes are integrated over the corresponding transect and averaged over a wave period.

As an example of the energy fluxes, Figure 4.10 shows the energy fluxes of model run 2 and model run 4 (widening shelves with *l6* stratification). It takes approximately 100 h for the barotropic modes to fully develop and after about 150 h, the effect of boundary conditions start propagating into the model and deteriorate the overall quality of solutions. For this reason, we selected the model time at 150 h for instantaneous internal wave field analysis, and 130-150 h for baroclinic energy analysis in the following discussions. Between the time intervals when the barotropic modes are stabilized, the offshore baroclinic energy fluxes are building up over time. At 150 h, the magnitude of the

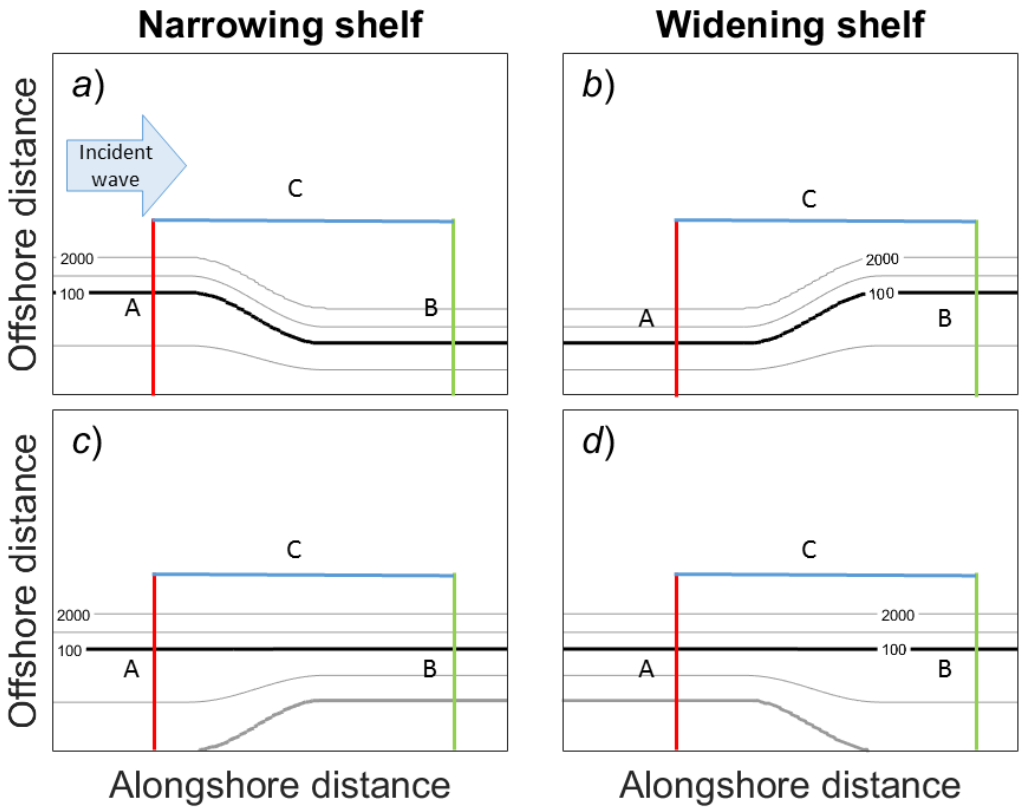

Figure 4.9 A schematics of transects where diagnostic energy fluxes and internal wave scattering are calculated.

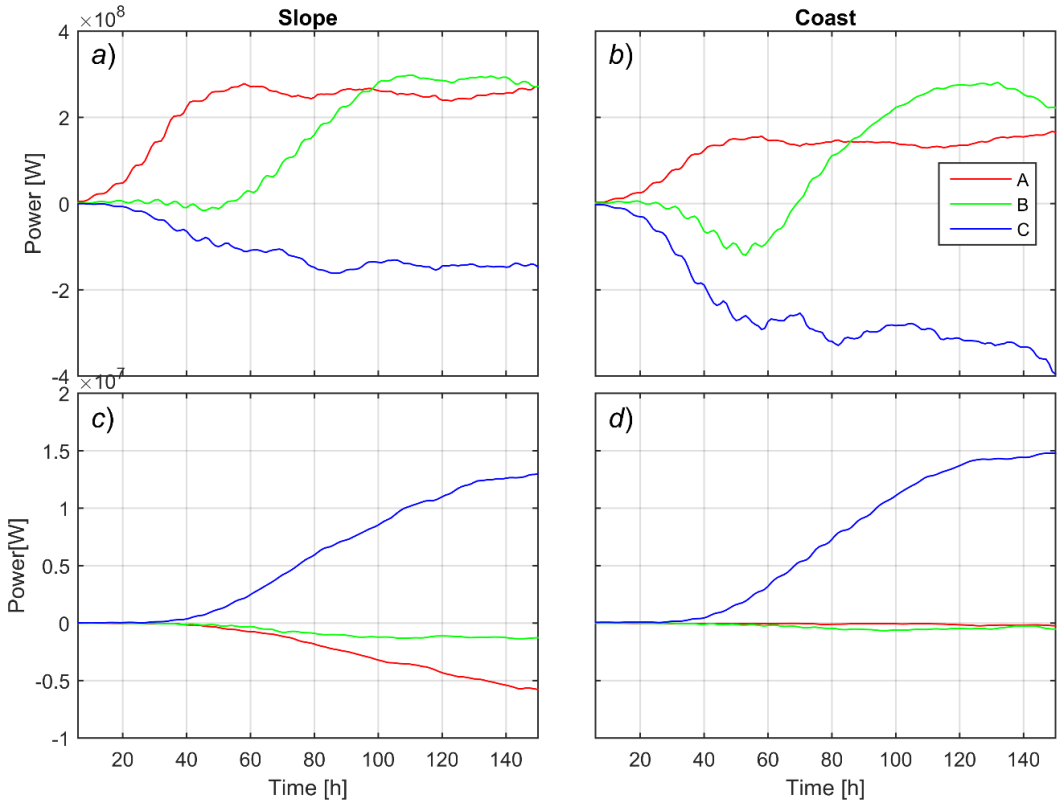

Figure 4.10 Evolution of barotropic and baroclinic energy fluxes over time. The left panels (a and c) show model run 2 (widening by a slope with *l6* stratification). The right panels (b and d) show model run 4 (widening by a coastline). The top panels show the barotropic energy fluxes. The bottom panels show baroclinic energy fluxes.

baroclinic energy fluxes reaches to near 10% of the onshore barotropic energy fluxes. This suggests a substantial internal wave field at the scattering region. For the widening by coastline case (model run 4), the divergence of alongshore barotropic energy fluxes is more intense than in model run 2. This results in a larger amount of inshore barotropic energy fluxes. The offshore baroclinic energy fluxes reach a nearly steady regime at approximately 130 h. The baroclinic energy fluxes alongshore in model run 4 are significantly lower than model run 2 due to the varying continental slope in model run 2. In model run 4, the alongshore barotropic energy flux at transect B builds up overtime and becomes influenced by the boundary effect before fully develop into a periodic regime. Since we look at the scattering effect through the incident energy fluxes and the cross shore energy flux, the energy flux at transect B has relatively small effect on the evaluation of scattering intensity for each model run.

To quantify the strength of scattering, the radiation of baroclinic energy fluxes from the scattering region is defined as:

$$R = \frac{\iint_R \nabla_H F_i'}{F_A} = \frac{-\int_A F_{ix}' dy + \int_B F_{ix}' dy + \int_C F_{iy}' dx}{F_A}, \tag{4.1}$$

where $\boldsymbol{F'_i}$ is the vertically integrated baroclinic energy flux vector defined in Chapter 2, **i** and **j** are the unit vectors in *x* and *y* directions respectively, and subscripts *x* and *y* refer to its *x* and *y* components. The baroclinic energy radiation is normalized by the incident energy flux F_A for each model run. The incident energy flux is defined as the barotropic energy flux term in Chapter 2. For the widening cases, the incident energy flux F_x is integrated in the offshore direction at x = 400 km from coast to the point where the free surface amplitude decays to one tenth of its amplitude at coast. For the narrowing cases, F_x

is integrated in the offshore direction at x = 300 km from coast to y = 600km. Time series of the integrated incident energy is averaged over the time interval from 80 to 140 h for each model runs. For the cases with h_3 = 4000 m, the time interval is 100 to 160 h. The resulting averaged energy is then normalized by the length of the integration transect so that it yields the mean incident energy flux per horizontal distance when the model is in a steady regime. For each model run, the baroclinic energy radiation is averaged over the time interval 130 h to 150 h (160-180 h for h_3 = 4000 m). The averaged radiation R for all model runs are shown in Table 4.1.

The barotropic energy fluxes for widening shelves show that the divergence of alongshore energy fluxes at the scattering region results in a significant amount of cross-isobath energy fluxes. This cross-isobath barotropic energy flux does not necessarily generate an internal wave field with significant intensity. The widening case with a weaker stratification (*l2*, model run 1) has almost an identical amount of divergence in barotropic energy fluxes, but the baroclinic energy fluxes are much weaker (Table 4.1). For the model runs with the standard bottom drag, there is a difference of baroclinic energy radiation between the shelves widening by slopes and coastlines (Figure 4.11). This difference become negligible when the low bottom friction condition is configured for the model (model run 12-15).

The energy fluxes show that there is strong baroclinic energy radiation from the scattering region. Next, we examine the internal wave generation by the barotropic to baroclinic energy conversion E_c defined in (2.17). The internal wave modes in Figure 4.4 show that linear stratifications and surface intensified stratifications have distinctive mode structures. The barotropic to baroclinic conversion reflects this difference. All model runs

Table 4.1 Summary of stratified model runs. L_{2dn} indicates the width of the continental slope; *R* is the baroclinic radiation; the bottom drag coefficient C_d is set to 2×10^{-3} for standard configurations (st), and 5×10^{-4} to represent simulations with low friction (lf).

Model Index	Stratification	L_{1up} (km)	L_{1dn} (km)	Change by	L_{2dn} (km)	Ls (km)	h_3 (m)	C_d	*R* ($\times 10^{-2}$)
1	*l2*	150	300	Slope	100	150	2000	st	0.21
2	*l6*	150	300	Slope	100	150	2000	st	4.16
3	*s2*	150	300	Slope	100	150	2000	st	6.06
4	*l6*	150	300	Coast	100	150	2000	st	3.84
5	*s2*	150	300	Coast	100	150	2000	st	4.95
6	*l2*	150	300	Slope	50	150	2000	st	2.98
7	*l6*	150	300	Slope	75	150	2000	st	9.61
8	*l6*	150	300	Slope	50	150	2000	st	16.45
9	*l6*	150	300	Slope	100	100	2000	st	4.05
10	*s2*	150	300	Slope	75	150	2000	st	8.41
11	*s2*	150	300	Slope	50	150	2000	st	14.73
12	*l6*	150	300	Slope	100	150	2000	lf	4.43
13	*s2*	150	300	Slope	100	150	2000	lf	5.94
14	*l6*	150	300	Coast	100	150	2000	lf	4.19
15	*s2*	150	300	Coast	100	150	2000	lf	5.96
16	*l4*	200	300	Slope	100	150	4000	st	7.35
17	*s3*	200	300	Slope	100	150	4000	st	14.87
18	*l2*	300	150	Slope	100	150	2000	st	0.03
19	*l6*	300	150	Slope	100	150	2000	st	0.57
20	*l6*	300	150	Coast	100	150	2000	st	1.09
21	*s2*	300	150	Slope	100	150	2000	st	0.27

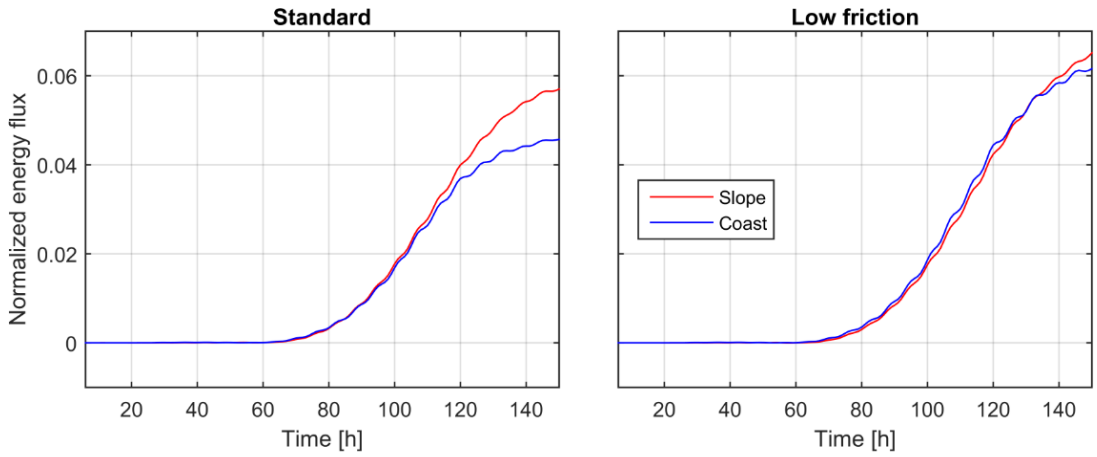

Figure 4.11 Normalized baroclinic radiation of the model runs with *s2* stratification. The left panel show standard configuration (model run 3 and 5). The right panel show model runs with low friction (model run 13 and 15).

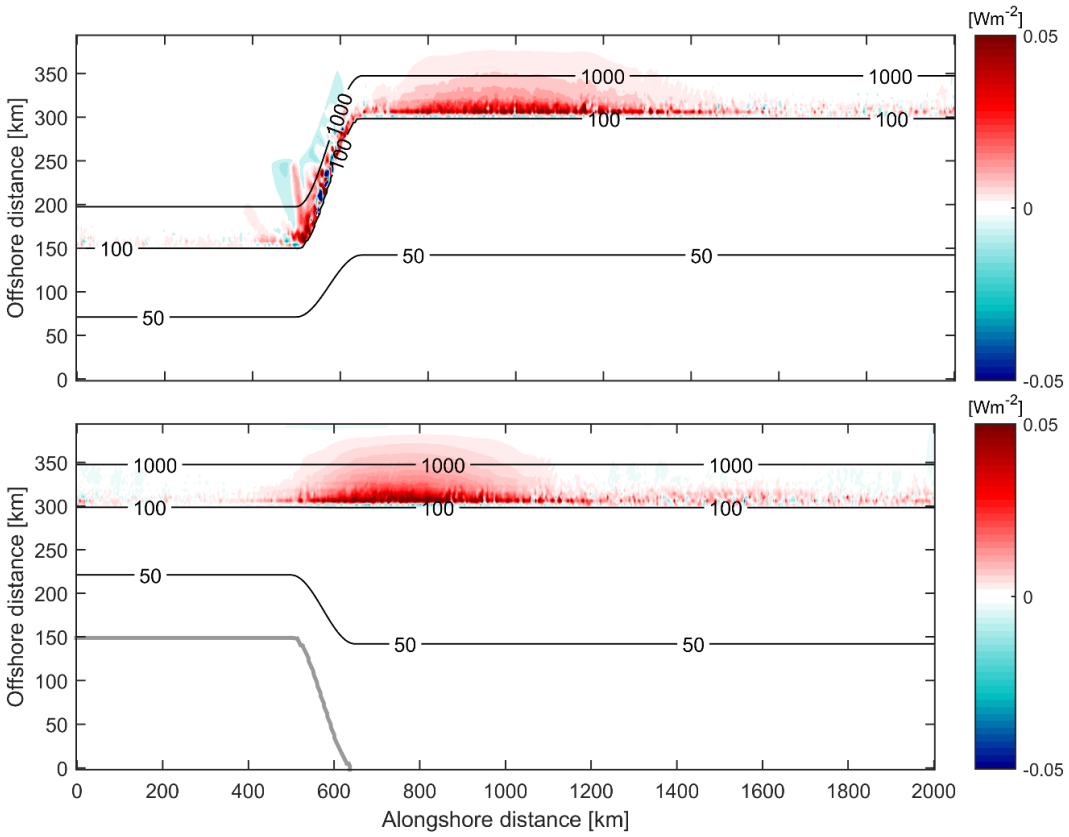

Figure 4.12 Barotropic to baroclinic energy conversion for model run 2 and model run 4.

with linear stratifications (*l2*, *l4*, and *l6*) have a similar barotropic to baroclinic conversion pattern, hence only the standard *l6* case (model run 2 and 4) is shown in Figure 4.12. The conversion is concentrated at the continental slope by the shelf break downstream the scattering region. The conversion region extends over 1000 km from the scattering region. The region with the highest conversion rate is close to the shelf break, where the water depth ranges from approximately 100 m to 500 m. When the shelf width changes by a slope, there is a significant amount of barotropic to baroclinic conversion along the shelf break at the scattering region. This result reflects the difference between the baroclinic energy fluxes in Figures 4.10c and 4.10d. The negative (upstream) baroclinic energy fluxes across transect A (Figure 4.10c) and the barotropic to baroclinic energy conversion at the shelf break of the scattering region suggest an internal wave field radiating off shelf. When the shelf width changes by a coastline, all conversions remain within the straight continental slope. For the model runs with surface intensified stratifications, the conversion region extends from the shelf break all the way to the bottom of the continental slope (Figure 4.13). The sign changes in the conversion region suggest that surface intensified stratification results in a different internal wave field.

To visualize the internal wave field, the offshore radiation of internal waves is shown as density perturbations in Figure 4.14 for model run 2. The internal wave field extends downstream from the scattering region. From the evolution of baroclinic energy fluxes (e.g., Figures 4.12c and 4.12d), the internal wave field enters a quasi-steady regime at 150 h at the transects where energy fluxes are estimated. Therefore, all results shown are selected at t = 150 h. The wave field shown is selected at z = -397 m, close to the maximum of the vertical profile of w for the second and the third internal wave modes (Figure 4.4b).

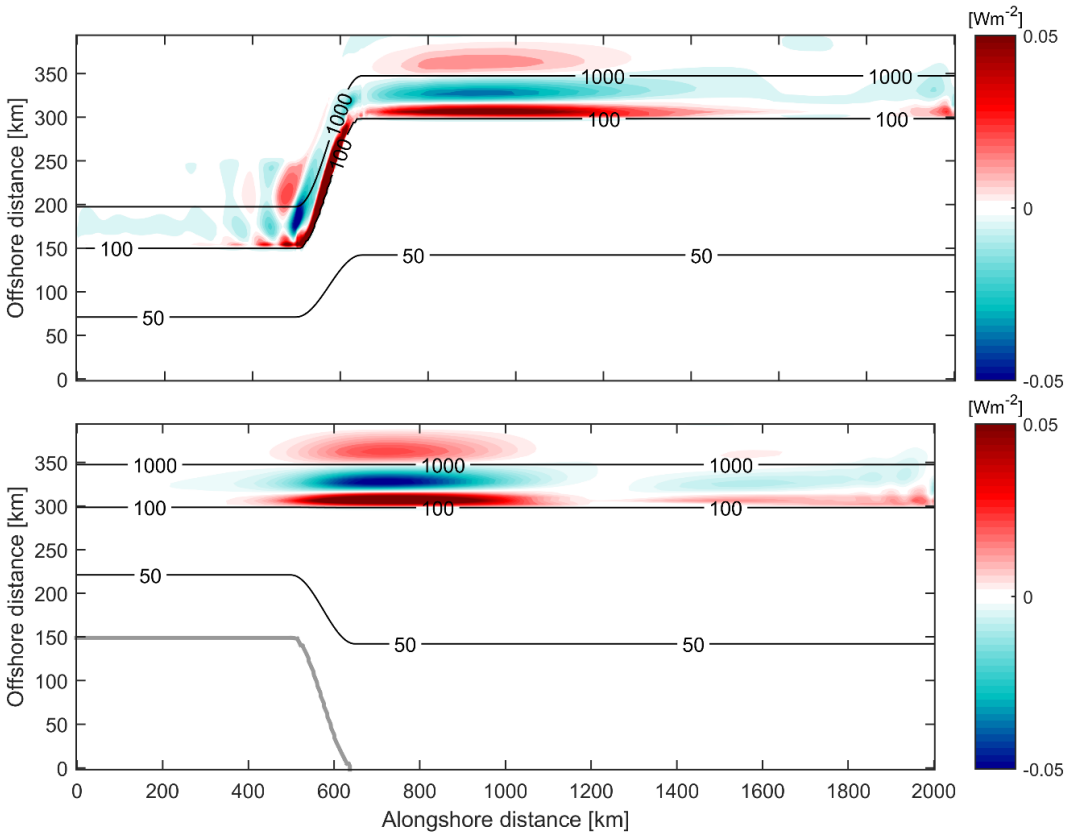

Figure 4.13 Barotropic to baroclinic energy conversion for model run 3 and model run 5.

Table 4.2 Theoretical phase speeds and wavelengths for the internal wave modes in all model runs.

Stratification	Mode 1 C (m/s)	Mode 1 λ (km)	Mode 2 C (m/s)	Mode 2 λ (km)	Mode 3 C (m/s)	Mode 3 λ (km)
l2	2.71	117.2	1.36	58.6	0.9	39
l4	5.42	234.2	2.71	117.1	1.81	78.1
l6	4.7	202.9	2.35	101.4	1.57	67.6
s2	2.2	95.2	1.08	46.6	0.77	33.2
s3	4.08	176.3	2.29	99.1	1.51	65.2

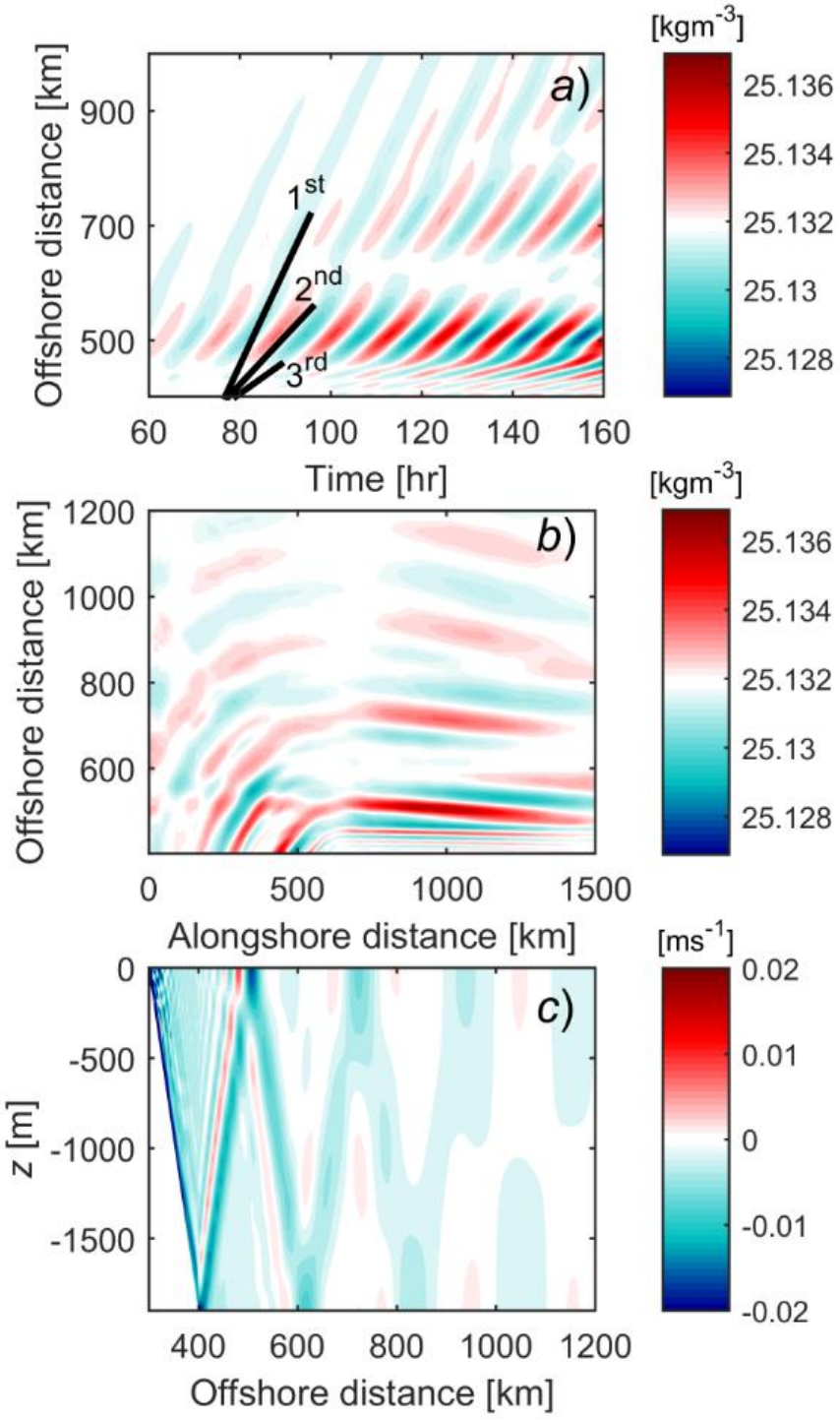

Figure 4.14 The internal wave field in model run 2: (a) density perturbation at z = -397 m and t = 150 h; (b) evolution of density perturbation along the cross-shore direction at x = 900 km and z = -397 m; and (c) vertical structure of cross-shore baroclinic velocity at x = 900 km and t = 150 h. Bold black line represents a theoretical phase speed of the internal wave modes (Table 4.2).

As shown in the phase propagation of density perturbations (Figure 4.14a), the wave field is dominantly the second and the third modes. The phase propagation is in good agreement with the theoretical phase speed of internal wave modes (Table 4.2) The dispersion of internal wave modes can be seen from the vertical structure of the cross-shore velocity (Figure 4.14c). At near shelf region the cross-shore velocity component shows internal wave beam structure extending more than 800 km offshore, suggesting existence of multiple wave modes. At y = 1000 km, the vertical structure of the horizontal velocity has only one node at approximately z = -1000 m, suggesting that only the first internal wave mode which has the highest phase speed reaches the region. Model run 1 with a weaker stratification (*l2*) has a similar internal wave field is shown in Figure 4.15, but the amplitude of the internal wave field is significantly weaker, and the first mode is barely visible.

For the model run with *s2* stratification (model run 3), the dominant wave mode is the first mode (Figure 4.16a). Because of the surface intensified buoyancy profile, the vertical profile of w for the first mode reaches maximum at the upper depth level (Figure 4.4c), where the barotropic forcing is the strongest. This suggests that the first mode internal wave is in a good match with the barotropic forcing. The strongest barotropic to baroclinic conversion (Figure 4.13) is also in a good match with the maximum of w for the first mode structure. Lacking the beam structure in the velocity field (Figure 4.16c), the oscillations of cross-shore velocity over the continental slope (x = 300-400 km) clearly reflect the changing sign of barotropic to baroclinic conversion in Figure 4.13. The internal wave radiation (Figure 4.16b) shows that the wave length of the propagating internal waves is approximately 100 km, in agreement with the theoretical wave length. The selected wave

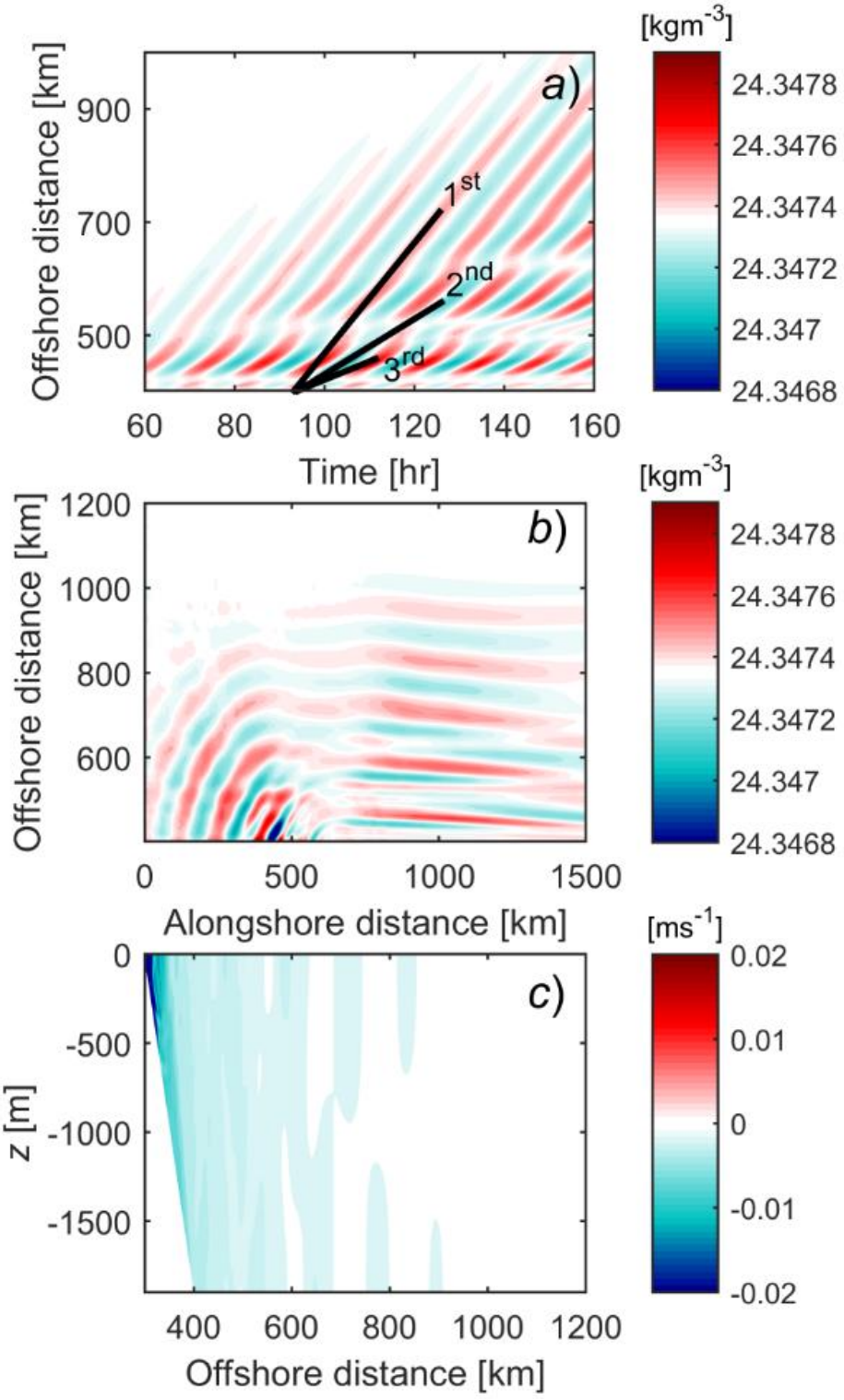

Figure 4.15 Same as in Figure 4.14 but for model run 1.

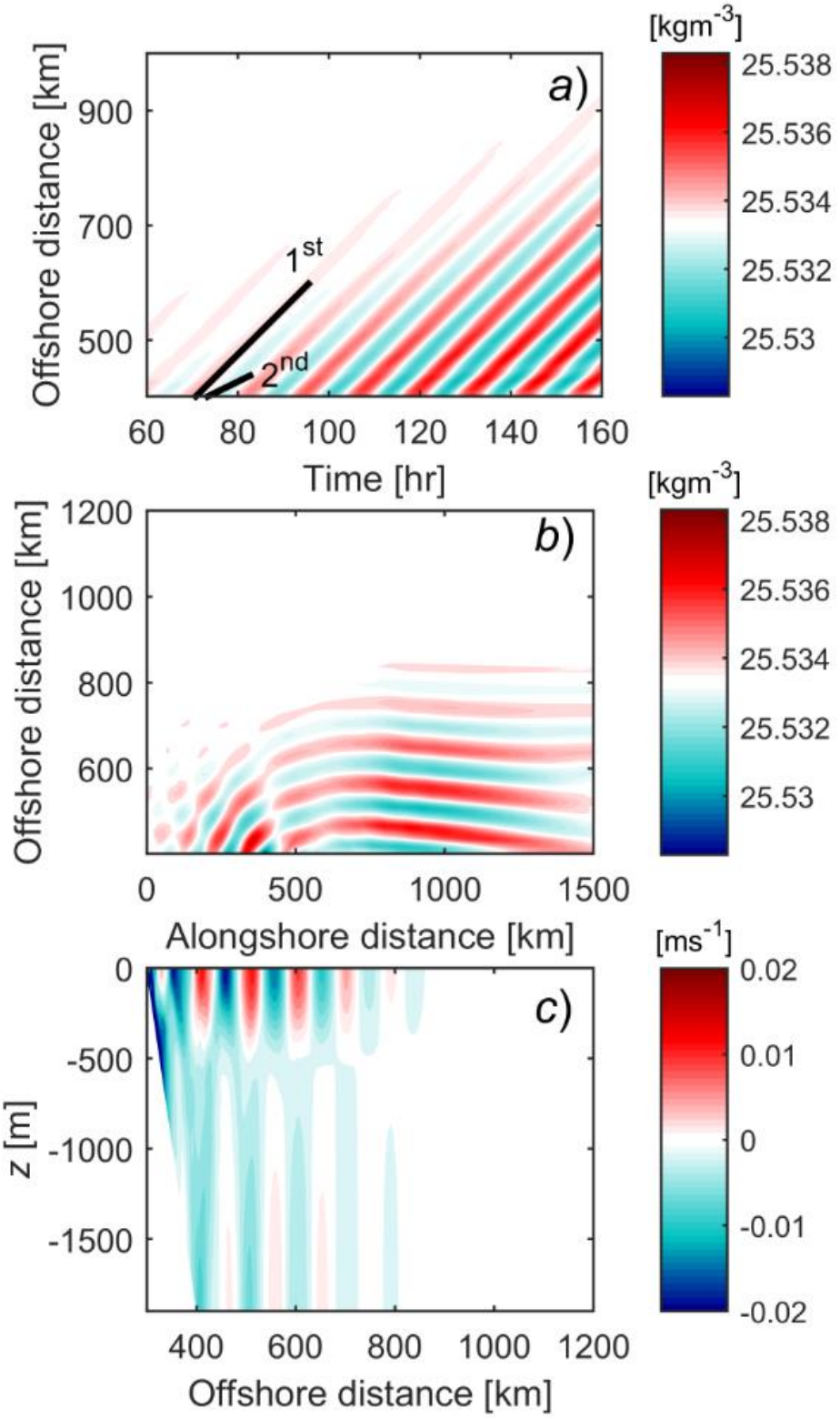

Figure 4.16 Same as in Figure 4.14 but for model run 3; z = -471 m in (a) and (b).

filed is at z = -471 m, close to the maximum of w for the first internal wave mode. At different depth layers, the internal wave fields are similar but less energetic. The vertical structure of cross-shore baroclinic velocity shows that at approximately y = 400 km, a node line of the first mode occur at z = 500 m, in good agreement with the theoretical structure.

For model run 4 and 5, where the shelf width widens by a coastline, the internal wave field resembles the previous cases. The wave field for *l6* stratification (model run 4) is dominantly the second and third modes (Figure 4.17a). The wave field for *s2* stratification (model run 5) is dominantly the first mode (Figure 4.18a). As indicated in the barotropic to baroclinic energy conversion, the internal wave radiation now becomes aligned with the straight continental slope, reflecting the bottom topography.

In the previous cases with widening shelf, the depth increases from 100 m at the continental shelf break to 2000 m over 100 km. This slope is relatively gentle comparing to the real ocean. To expand the range of model scenarios applicable to the real ocean, similar model set up was configured for L_2 = 50 and 75 km downstream of the scattering region. The theoretical wave lengths of the internal wave modes (Table 4.2) show that for the linear stratifications, all the second and the third modes have wave lengths less than or close to 100 km. On a narrower continental slope, the slope becomes steeper and the vertical velocity increases. In result, the baroclinic energy fluxes become much higher after the continental slope turns narrow. For *l2* stratification (model run 6), when L_2 become 50 km, the barotropic energy fluxes at the scattering region have the same magnitude of the previous cases, whereas the offshore baroclinic energy fluxes are now more than 10 times higher than L_2 = 100 km (Table 4.1). Same as what the energy fluxes show, the internal wave fields are much more intense in model run 6-8. The *l2* stratification now can generate

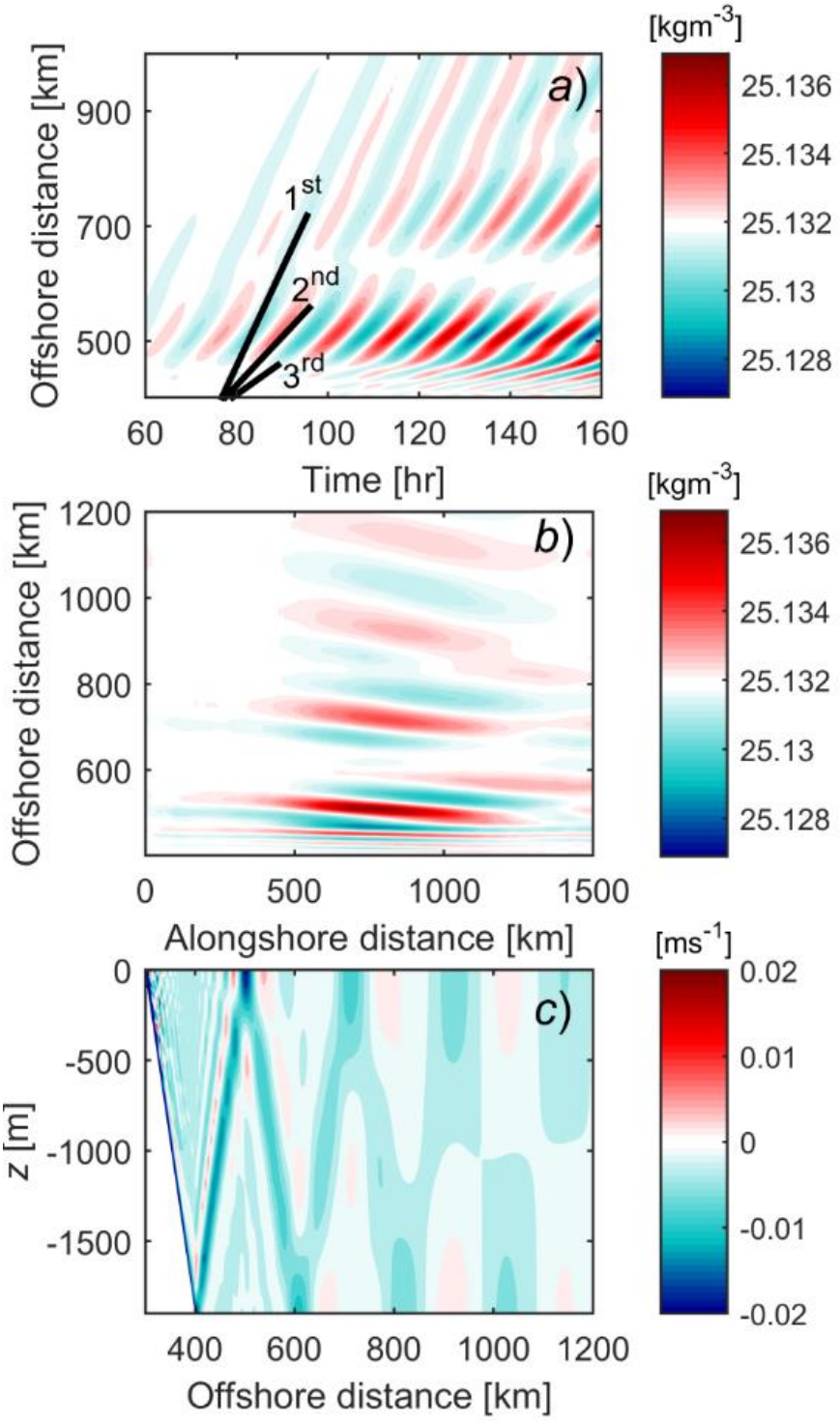

Figure 4.17 Same as in Figure 4.14 but for model run 4.

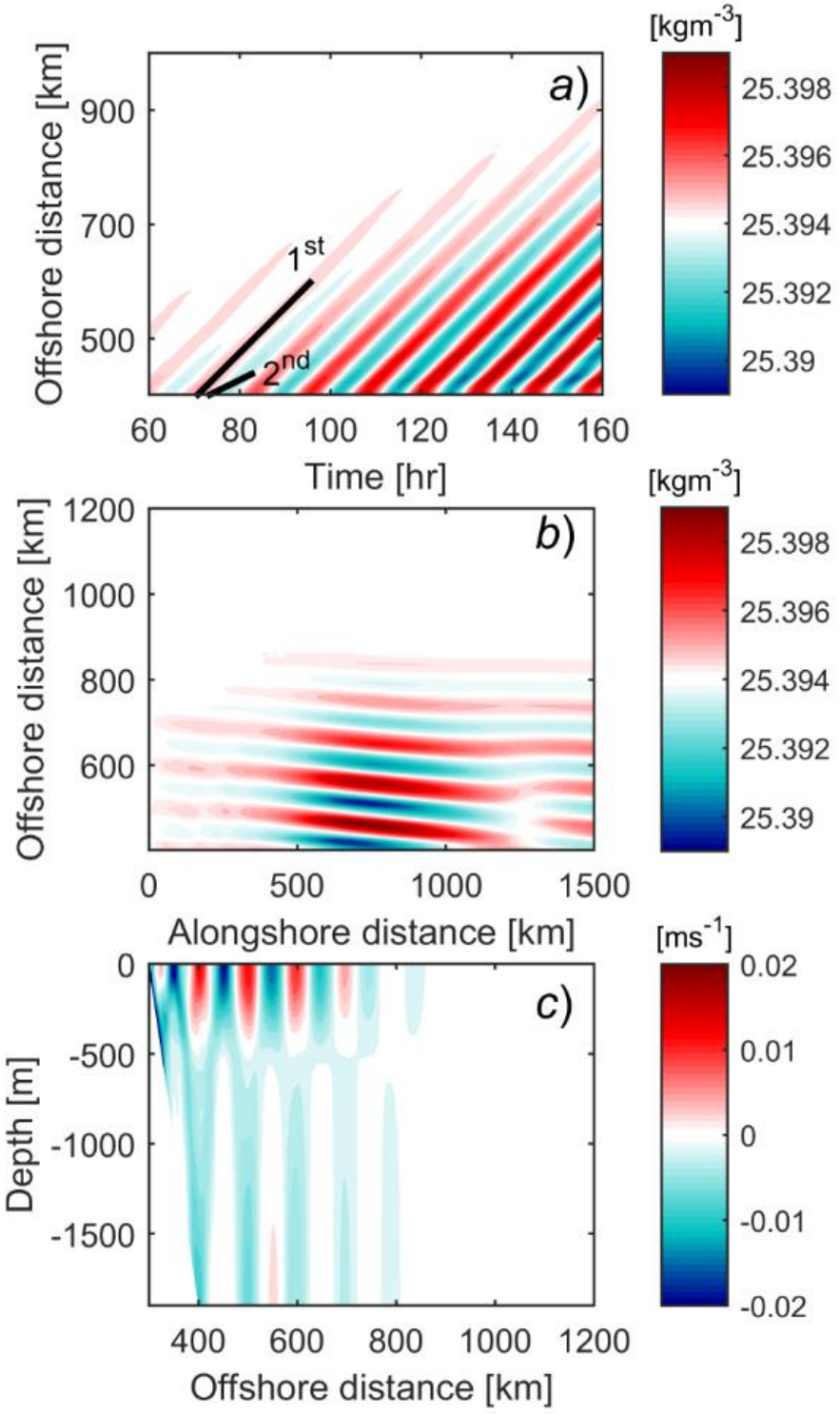

Figure 4.18 Same as in Figure 4.16 but for model run 5.

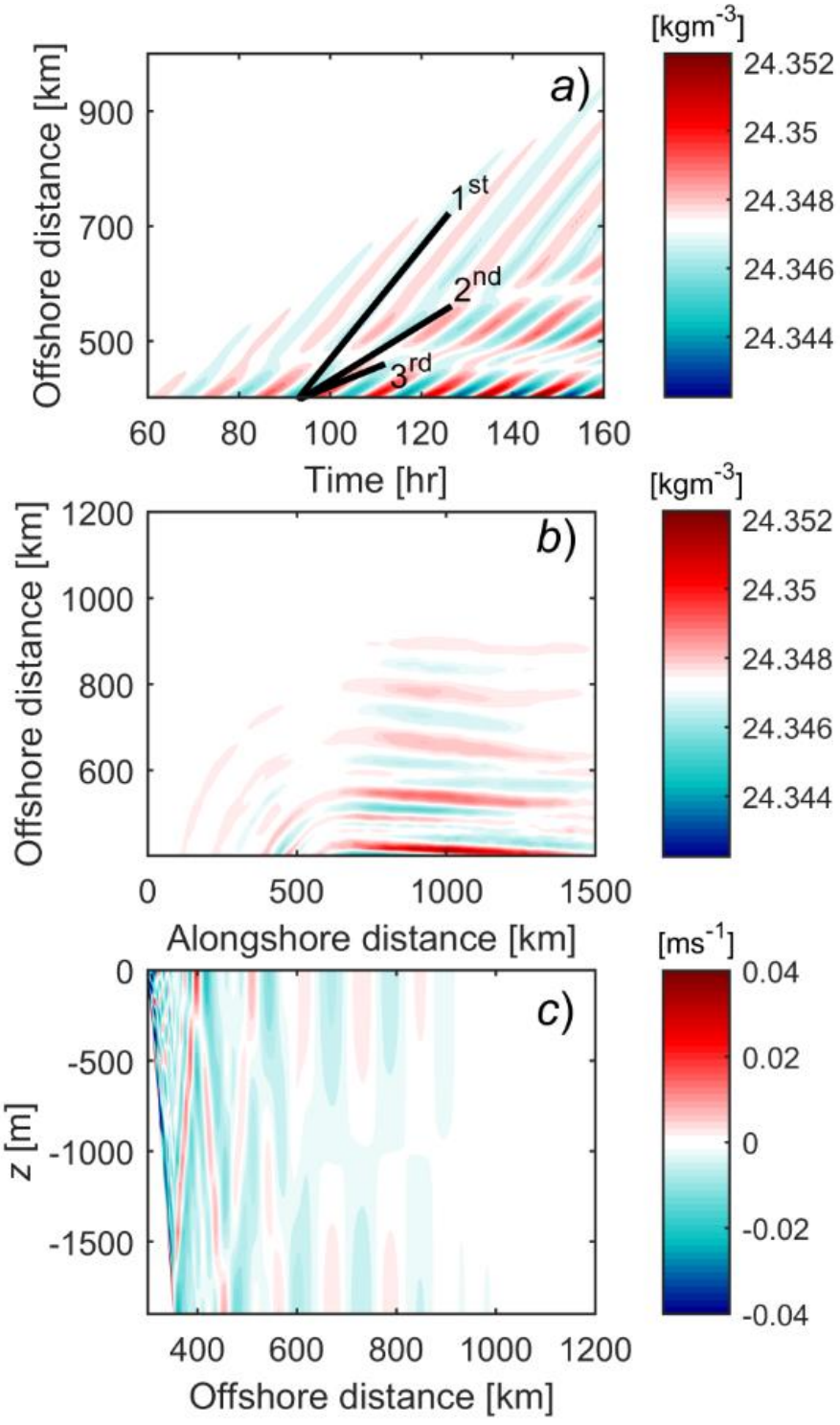

Figure 4.19 Same as in Figure 4.14 but for model run 6. For comparison, the color range used in (a) and (b) is the same as in Figure 4.14.

an internal wave field (Figure 4.19) as strong as the *l6* stratification with the gentler slope topography. For model run 8 (*l6* stratification), the model configuration required a higher spatial resolution of 2 km in horizontal and 40 *s*-coordinate vertical cells due to the presence of higher modes. This model run generates the most energetic internal wave field among all model runs with h_3 = 2000 m. The amplitude of density perturbation and baroclinic cross-shore velocity nearly doubled (Figure 4.20) compared to the standard model run of L_2 = 100 km (model run 2). Comparing to the standard model run, the vertical structure of the horizontal cross-shore velocity has a more compact beam structure.

As for the *s2* stratification (model run 11), the narrower continental slope also has a strengthening effect on the internal wave field (Figure 4.21). The internal wave field is still dominated by the first mode. The vertical structure of the horizontal velocity indicates a presence of higher wave modes at y < 400 km, but their effect is weak. The model runs with L_2 = 75 km have similar internal wave fields and thus is not shown.

For the cases with with h_3 = 4000 m (model run 16 and 17), the model configuration required a higher spatial resolution of 2 km for horizontal grid and 40 s-coordinate points in vertical. The baroclinic response for the case with *l4* stratification is qualitatively similar to the *l6* stratifications (Figure 4.22). For surface intensified stratification (s*3*, model run 17), unlike the *s2* stratification, the maximum of *w* for the first internal wave mode is now near the middle of the water column (Figure 4.4d). For this model run, the presence of first mode is significant (Figure 4.23a), but the internal wave radiation and the vertical structure of the cross-shore velocity show that higher modes are also strong. Comparing the energetics, the theoretical wave structure (Figure 4.3) suggests that the model runs with

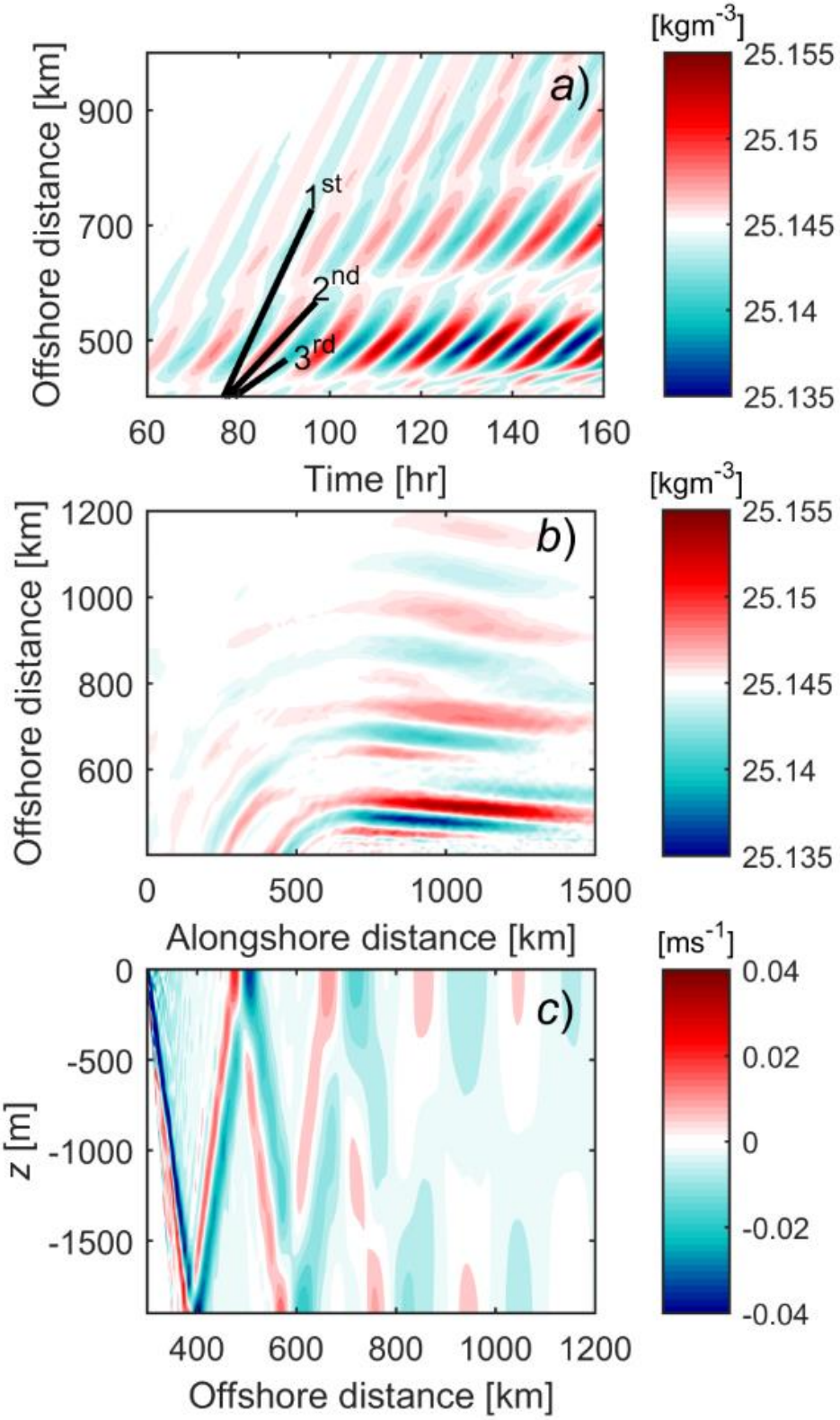

Figure 4.20 Same as in Figure 4.14 but for model run 8; z = -402 m in (a) and (b).

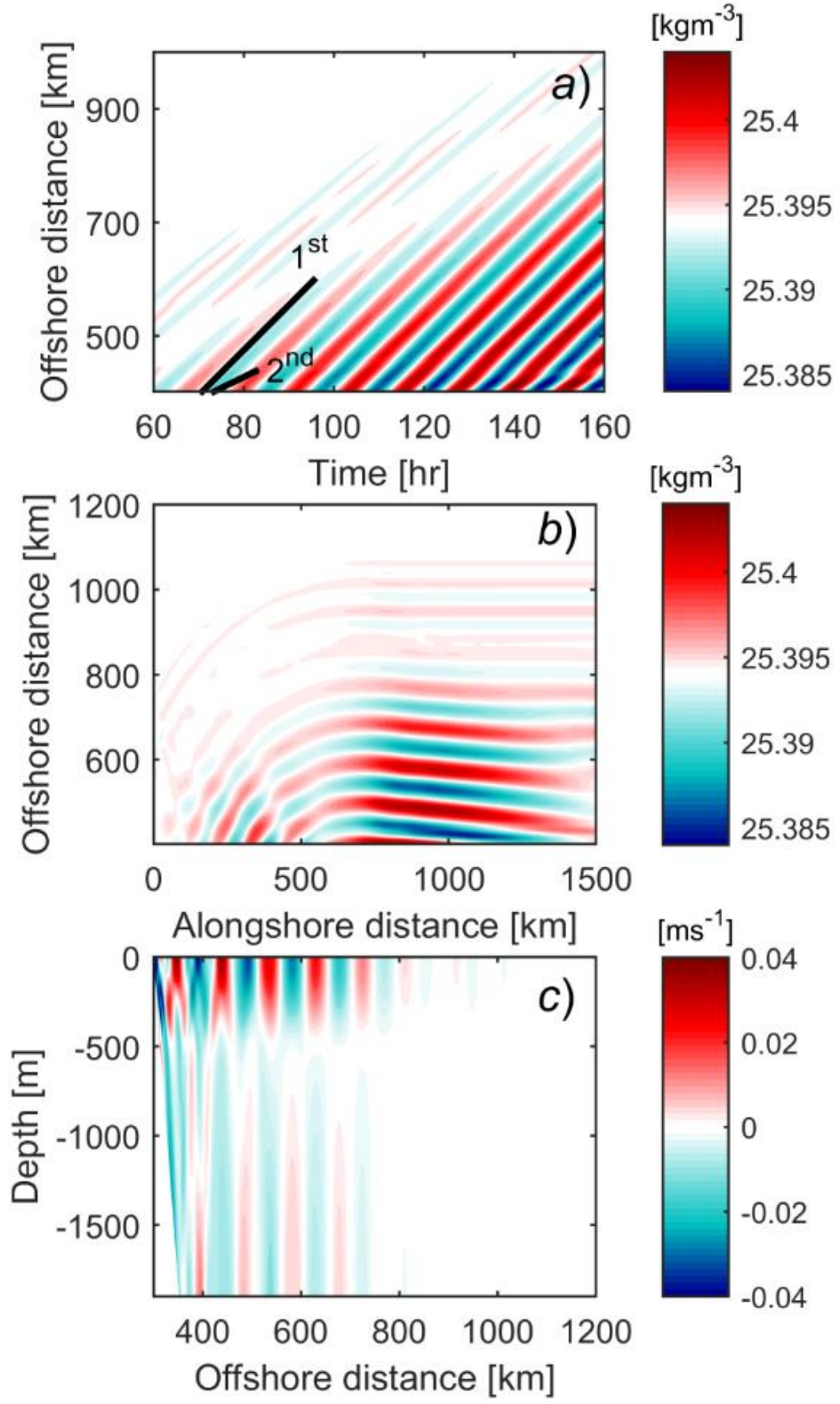

Figure 4.21 Same as Figure 4.16 but for model run 11.

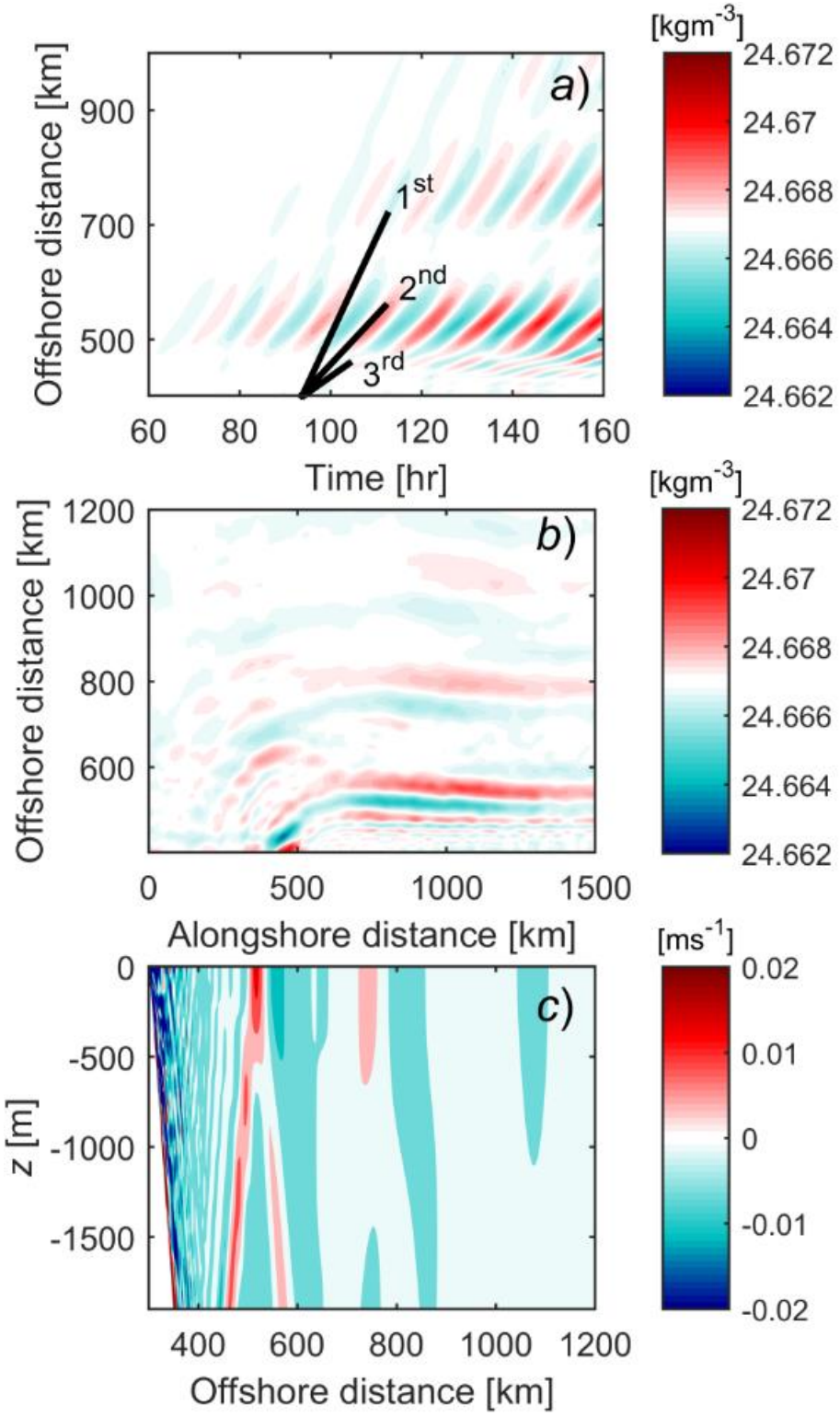

Figure 4.22 Same as in Figure 4.14 but for model run 16; z = -717 m in (a) and (b).

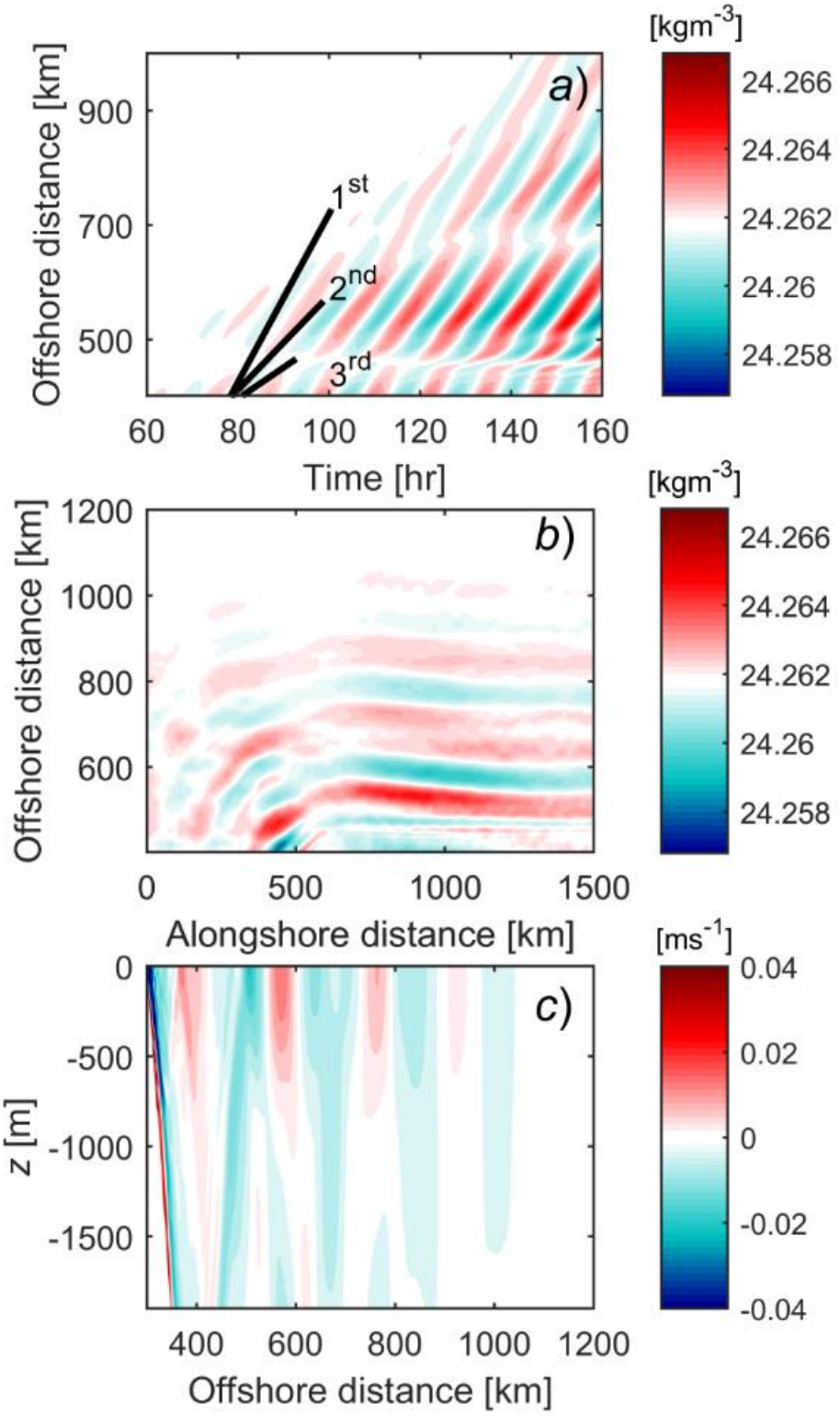

Figure 4.23 Same as in Figure 4.22 but for model run 17.

h_3 = 4000 m can yield a stronger barotropic energy divergence, and the normalized baroclinic energy fluxes also show that the baroclinic radiation is stronger than the previous cases (Table 4.1). Similar to what the energy fluxes show, the internal wave fields in these cases are more intense (Figures 4.22 and 4.23) than the model runs with h_3 = 2000 m.

For model runs with narrowing shelves (model run 18-21), the internal wave generation is weaker (Figures 4.24 and 4.25). Two model runs are shown here to demonstrate the difference: *l6* (model run 19) and *s2* (model run 21). For both model runs, the radiation of internal waves now occurs upstream of the scattering region, aligned with the bottom geometry of narrowing shelves. Since the incident energy is weaker for the narrowing shelves, we use the normalized baroclinic radiation to quantify the internal wave generation. Table 4.1 shows that even the strongest baroclinic radiation R for the narrowing shelves is 1.09×10^{-2}, significantly weaker than for the widening shelves ($\sim 4 \times 10^{-2}$) under the same configuration. This suggests that the strong divergence in the alongshore barotropic energy fluxes are mostly compensated by the barotropic energy radiation offshore, as discussed in the previous chapter.

4.4 DISCUSSION AND CONCLUSIONS

The barotropic models in Chapter 3 showed that semidiurnal Kelvin waves propagating along wide continental shelves can produce a significant amount of cross-isobath barotropic energy fluxes. Under stratified condition, the model produces a similar barotropic response. As the previous chapter shows, the direction of the cross-isobath barotropic energy flux depends on the adjustment of wave structures corresponding to the shelf widths, instead of widening versus narrowing of the ocean topography. The stratified

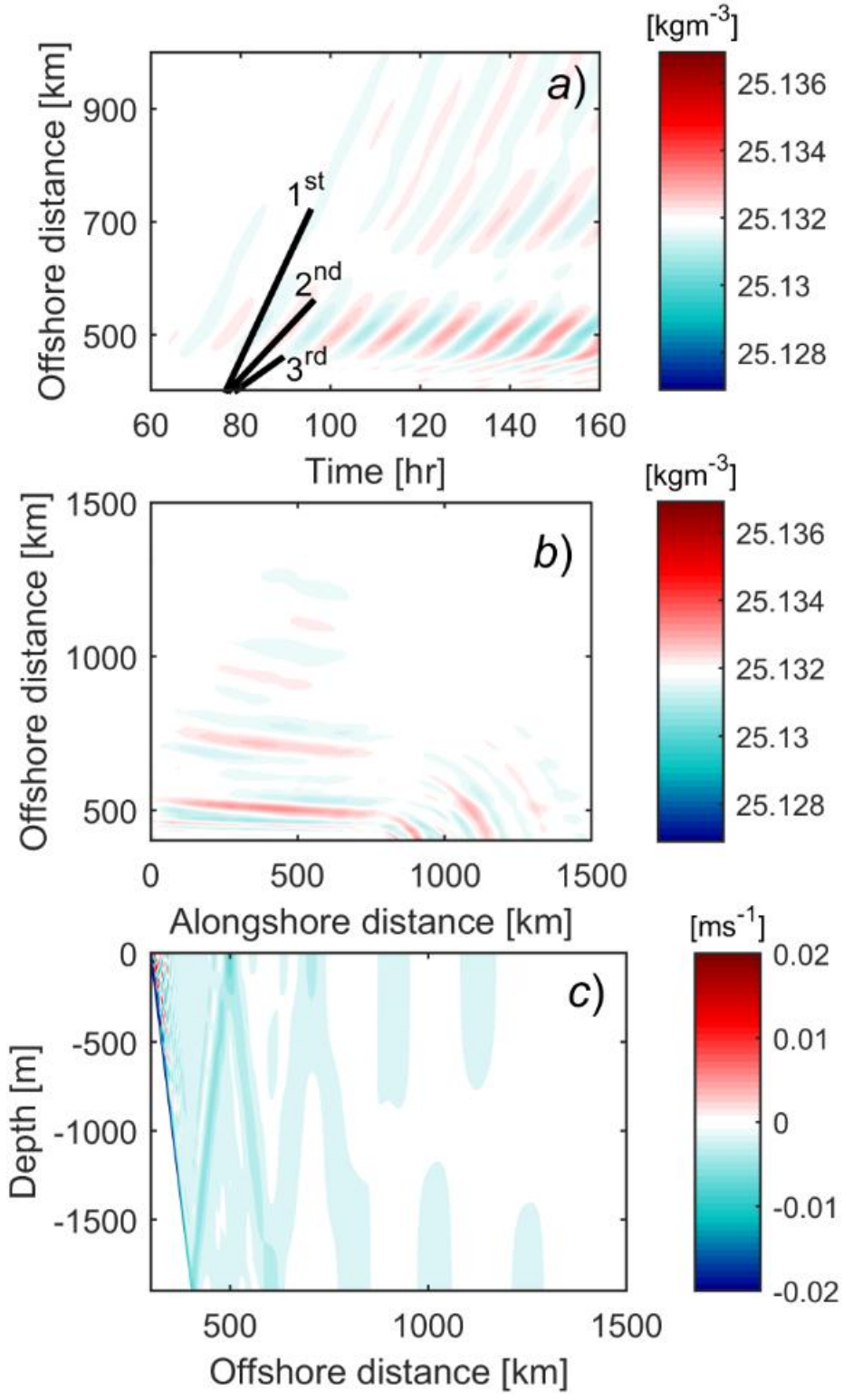

Figure 4.24 Same as in Figure 4.16 but for model run 19, x = 500 km. For comparison, the color range used in the figures is the same as in Figure 4.14.

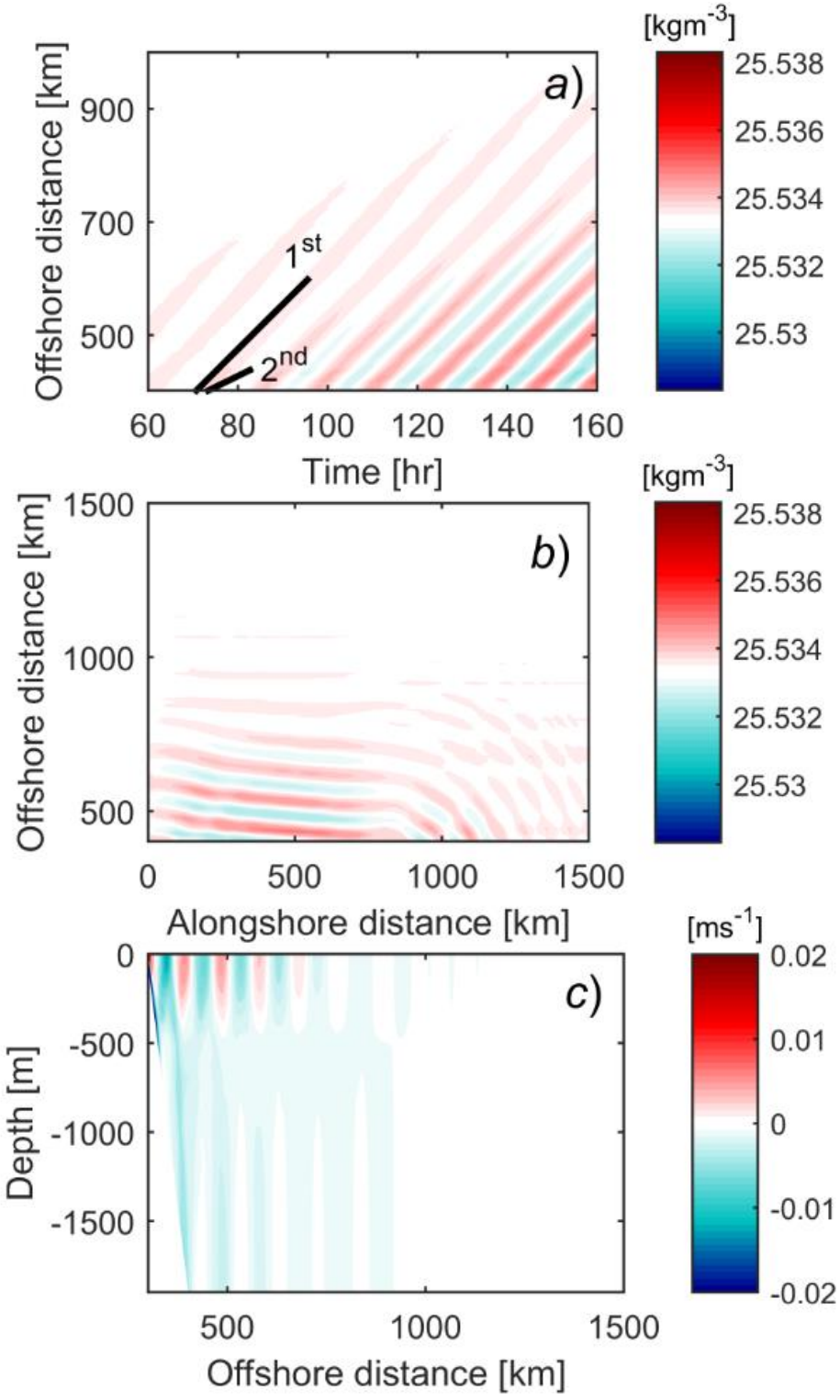

Figure 4.25 Same as in Figure 4.16 but for model run 21; x = 500 km. For comparison, the color range used in the figures is the same as in Figure 4.16.

model in this chapter uses fewer variations of shelf widths (150 km and 300 km), so that the scattering produces onshore barotropic energy fluxes when the shelf width widens and offshore barotropic energy fluxes when the shelf width narrows. As a result of stratification, the semidiurnal Kelvin waves scatter a significant amount of energy into internal waves when encountering alongshore changes of the shelf width.

The adjustment of the incident zero mode causes the propagating HKEW to scatter into both barotropic and baroclinic wave modes. Some wave modes radiate offshore while the others remain trapped along the coast (e.g., Dale et al. 2001). Since the continental slope width in this model ranges from 50 km to 100 km, which is relatively small comparing to the typical barotropic tidal wavelength, internal wave modes with smaller spatial scale can provide a better fit between the incident and transmitted HKEW. The energy partition between each internal wave mode depends on how well the wave modes available for the specific bottom topography fit the barotropic forcing so that a continuity of pressure and velocity fields is maintained during the scattering. The barotropic forcing of internal wave generation in the model is concentrated near the shelf break. For the linear stratification (*l2*, *l4*, and *l6*), the vertical structure of the second and the third internal wave modes provides a better fit to the maximum of barotropic forcing. For the surface stratified models (*s2*), the vertical profile of the first mode fits the baroropic forcing the best. This tendency corresponds to the resulting internal wave fields in the model. As for the surface-intensified stratification in the deeper open ocean (*s3* with h_3 = 4000 m, model run 17), the vertical profiles of the second and the third mode fit better the barotropic forcing, hence there is a presence of higher modes in the internal wave field.

For the widening shelves, the most energetic baroclinic energy flux reaches approximately 15% of the incident barotropic energy. For the narrowing shelves, the internal wave radiation is significantly lower (Table 4.1). In these cases the alongshore barotropic energy fluxes converge and produce a large amount of offshore energy fluxes. As shown in Chapter 3, the alongshore energy flux convergence can lead to more than 50% of the incident energy flux scattering into barotropic Poincaré waves when the divergence parameter D_e become less than -1 (Figure 3.10). Therefore, in these cases, the scattering of the incident HKEW into radiating barotropic modes are more significant than internal wave generation. This suggests that the internal wave generation becomes more energetic when the barotropic radiation is weak. This corresponds to the situation when the divergence parameter D_e is positive, i.e. the alongshore energy fluxes diverges at the scattering region.

The numerical models in this chapter show that internal waves can be generated when semidiurnal tidal species along wide continental shelves encounter a change in shelf width. The internal wave generation mechanism in these simulations relates to many areas in the world ocean characterized by energetic semidiurnal tides and wide continental shelves – the West European shelf, the East China Sea, the East Australian shelf, and the Patagonian shelf. Among these, the Celtic Sea and the Patagonian shelf are particularly relevant to the model. In both cases the propagation of semidiurnal tides has HKEW features. The Celtic Sea is known as one of the locations with the highest barotropic to baroclinic tidal energy conversion (e.g. Baines, 1982; Green et al, 2008; Zhao et al. 2015). Strong semidiurnal tides at Celtic Sea propagate from a relatively narrow shelf at the coast of France to the 400 km wide Celtic Shelf. The most energetic internal waves are located at the steep shelf break of the Celtic Sea, propagating offshore as high internal wave modes.

The Patagonian shelf was also considered as an important tidal conversion site in early models (e.g. Baines 1982). It is characterized by strong semidiurnal tides and a wide continental shelf with a large decrease in shelf width between 50 °S to 40 °S. Although model studies have found strong cross-isobath barotropic energy fluxes on the Patagonian shelf (e.g., Palma et al. 2004), no strong baroclinic radiation is found in the area. Possible reasons for this lack of energy radiations are discussed in the next chapter.

.

CHAPTER 5

OBSERVATIONS OF SEMIDIURNAL INTERNAL TIDES ON THE PATAGONIAN SHELF

The stratified models in Chapter 4 showed that when the semidiurnal tides encounter a variable shelf width, the resulting onshore barotropic energy fluxes can generate an energetic internal wave field. Locations relevant to the numerical study include the Celtic Sea and the Patagonian Shelf, of which, the Celtic Sea is well known for its energetic internal wave field. The Patagonian Shelf is known for strong semidiurnal tides and intense seasonal stratification, but the internal tide generation appears to be weaker. Global tidal model simulations cannot resolve generation at the shelf break due to their relatively coarse resolution (Simmons et al, 2004; Buijsman et al 2016). To understand the lack of observational evidence for strong internal tide generation at the shelf break, we study the generation mechanism and the time variability of semidiurnal low-vertical mode internal waves observed in two mooring records at the Patagonian Shelf. At both mooring sites, the velocity spectra reveal strong baroclinic oscillations at semidiurnal frequency with a vertical structure resembling the first mode. Unlike the barotropic tides with strong cross-isobath polarization, the baroclinic tidal ellipses are less polarized. The internal tide propagation is delineated by estimating a proxy for the baroclinic energy flux, which is a product of the band-passed baroclinic velocity near the bottom and temperature at mid-depth. The proxy vectors show that the internal tide propagation is highly sensitive to the strength of the Malvinas Current propagating over the continental slope. When the mean

current becomes stronger, proxy vector is oriented along the isobaths pointing southward, upstream of the Malvinas Current direction. It is concluded that the presence of energetic western boundary current blocks the offshore radiation of internal tides.

5.1 INTRODUCTION

Semidiurnal tidal waves propagating along continental margins are strongly affected by wide continental shelves (e.g., Ke and Yankovsky, 2010; Zhang and Yankovsky, 2016): the across-shelf wave structure no longer resembles an analytical Kelvin wave solution and concentrates over the variable topography, while both the phase speed and group velocity are substantially reduced compared to long gravity waves in the open ocean. Furthermore, these modified Kelvin waves are very sensitive to alongshore changes of continental shelf topography. When shelf width changes in the alongshore direction, the alongshore energy flux on the shelf becomes divergent and results in compensating cross-isobath energy flux farther offshore, over the continental slope. The combination of cross-isobath barotropic velocities at the shelf break and a stratified water column results in the radiation of internal waves (IWs). Under favorable conditions, 15% or more of the incident barotropic tidal energy flux can radiate as IWs (Yankovsky and Zhang, 2017).

One of the regions in the World Ocean which fits this scenario is the Patagonian Shelf (PS) in the southwestern Atlantic Ocean. The Patagonian continental shelf extends from the southeastern tip of South America (55 ºS) to ~ 40 ºS. North of the Malvinas Islands, the shelf width of the PS is more than 500 km, and gradually narrows along the downstream direction to less than 200 km at 38 ºS. Water depth increases to over 4 km in

the open ocean across the 200 km wide continental slope. The Patagonian Shelf is known for energetic semidiurnal tides propagating along the shelf (e.g., Webb, 1973; Kantha et al., 1995; Glorioso and Flather, 1997). Palma's et al. (2004) numerical study found strong M_2 tidal energy flux along and across the northern part of the PS where the shelf narrows, with associated tidal dissipation concentrated in the region. Water stratification in the PS area is characterized by a seasonal thermocline on the mid- and outer shelf (typical bottom depths of 100 – 200m), which is significantly weaker during the austral winter (e.g., Martos and Piccolo, 1988; Rivas and Piola, 2002; Bianchi et al., 2009). The shelf is bounded offshore by the Malvinas Current (MC), a western boundary current carrying relatively cold sub-Antarctic water along the western margin of the Argentine Basin (e.g., Piola and Gordon 1989). The transition between the shelf and the MC water is characterized by moderate cross-shore temperature and salinity gradients (e.g., Romero et al., 2006; Saraceno et al., 2004; Franco et al., 2008). At the shelf break (typical bottom depth of ~200m) the stratification is somewhat weaker than observed farther onshore (Romero et al., 2006). Nonetheless, temperature and salinity records show the onset of a well-defined pycnocline in early November (Valla and Piola, 2015).

Strong stratification in the warm season and cross-isobath barotropic energy fluxes on the PS provide favorable conditions for internal tide generation. Early theoretical studies of internal tides (e.g., Baines, 1982) considered this region as one of the substantial contributors to global internal tidal energy production. However, due to the lack of observations of internal tides in the region, the barotropic to baroclinic energy conversion was not considered as a major source of barotropic dissipation on the PS. Later studies (e.g. Kantha et al., 1995; Glorioso and Flather, 1997) concluded that most of the tidal energy

dissipates through bottom friction. Global internal tide model simulations (e.g. Simmons et al., 2004; Buijsman et al. 2016) found that primary regions of M_2 conversion into baroclinic modes in the South Atlantic Ocean are the Drake Passage and the Scotia Sea, south of the PS, whereas little conversion occurred at the Patagonian Shelf break.

IWs observed by satellite imaging (Jackson, 2007) suggest that there is possible baroclinic energy radiation over the Patagonian continental slope, but such results cannot be confirmed by global altimetry data (Zhao et al., 2016) because the observations are hindered by mesoscale processes. A comparison between observational and model data (e.g., Buijsman et al., 2015, Buijsman et al., 2016) shows that the global tidal model with parameterized barotropic to baroclinic conversion predicts lower tidal dissipation on the PS than the dissipation inferred from the TPXO8-atlas model. The lower dissipation suggests that the conversion at the Patagonian shelf break in HYCOM may be missing because the model does not resolve the internal tide generation there.

Global internal tide models do not resolve the generation of internal tides at the PS due to insufficient spatial resolution. Palma et al. (2008) used a baroclinic model with a horizontal resolution of 5 km and 25 levels in the vertical to simulate the circulation responses to tides, shelf break fronts, and wind forcing, but the associated IW dynamics response was not reported. A recent study (Magalhães and da Silva, 2017) addresses IWs in the region, but of non-tidal origin. In their study, IWs are identified in high-resolution satellite images, and are suggested to be due to the resonant generation by the MC encountering topographic irregularities over a continental slope. The northward propagating MC has a strong flow of 0.4 - 0.7 m/s between 43.5ºS to 50ºS (Piola et al., 2013; Artana et al., 2016) and is therefore likely to influence the generation of IWs.

This study focuses on the semidiurnal internal tides in the PS region inferred from mooring data collected at the shelf break. The rest of this chapter is organized as follows: Section 5.2 describes the collection and analysis of the data; Section 5.3 presents the results of data analysis; discussion of the possible influence of the MC on internal tides in the study area along with conclusions are presented in Section 5.4.

5.2 DATA COLLECTION AND ANALYSIS

Velocity and temperature time series were obtained from two mooring deployments (Valla and Piola 2015) along the 200-m isobath at the shelf break (Figure 5.1). Mooring data were collected from October 16 through December 5, 2005 at site A (43.820 °S, 59.673 °W), and from September 25, 2006 through March 8, 2007 at site B (40.987 °S, 57.003 °W). Both moorings measured the current velocity at hourly intervals with acoustic Doppler current profilers (ADCP). The current velocities were estimated from 10 m bins and recorded at 7 depth levels (10, 30, 50, 70, 100, 130, and 160 m), spanning nearly the entire water column. Temperature was recorded at 6 depth levels (1, 10, 30, 50, 75, and 100 m) at site A, whereas only near-surface (1 m) temperature was recorded at site B.

Historical CTD data were used to investigate the vertical density structure in the vicinity of the shelf break near the mooring sites. The data are available at the US NODC World Ocean Database 2013 http://www.nodc.noaa.gov/OC5/WOD/pr_wod.html (Boyer et al., 2013). Hydrographic stations were selected within 100 km from each mooring site and within 11 km inshore from the 200-m isobath (Figure 5.1). No data were selected at locations over the continental slope due to strong temperature and salinity gradients associated with the Malvinas Current (e. g., Romero et al., 2006; Piola et al., 2010).

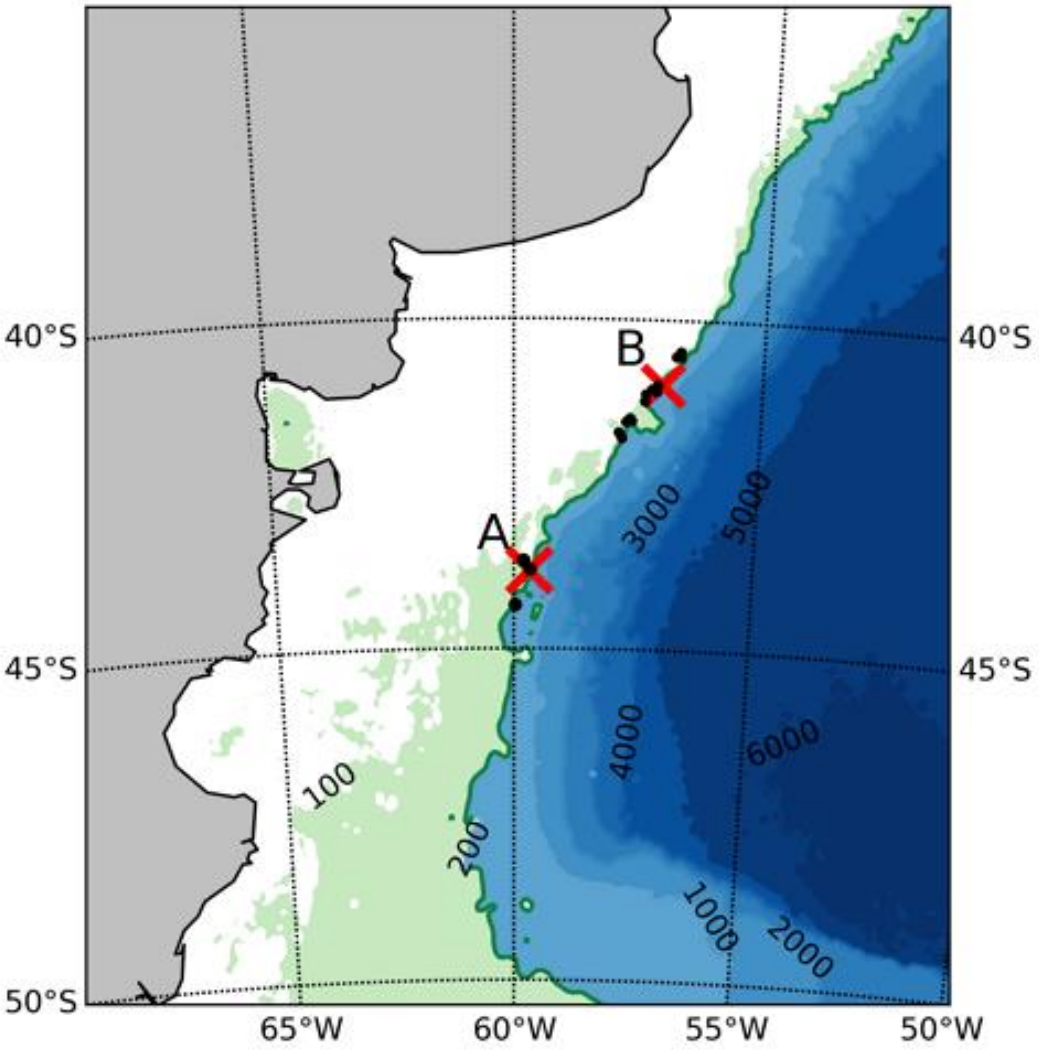

Figure 5.1 Map of the study area showing bathymetry (in meters), locations of mooring sites (red crosses), and hydrographic stations (dots).

Furthermore, CTD profiles were selected for the seasons representing mooring deployments: the austral spring for site A and the austral spring-summer for site B. The selected hydrographic stations are summarized in Table 1 and all density profiles are shown in Figure 5.2.

For site A, one of the three available stations was occupied during the actual mooring deployment as a part of the Global Environment Facility (GEF) Patagonia Project (Charo and Piola 2014). At site B, available stations cluster in two groups, representing early austral spring (September-October) and late summer (February-March) (Figure 5.2). Stations from late austral summer are characterized by a seasonal pycnocline within the uppermost 40 m. Profiles of buoyancy frequency N defined as $N^2 = -\frac{g}{\rho_0}\frac{d\rho_0}{dz}$ were estimated for all density profiles. Here, $\rho_0(z)$ is the density, z is the vertical coordinate (positive upward), and g is the acceleration due to gravity. Both ρ_0 and N profiles were gridded in 1 m vertical bins, and N profiles were further smoothed by applying 10-m running average.

The observed N profiles were used to assess the IW properties. The IW dispersion characteristics and the normal mode vertical profiles were estimated by solving numerically the following boundary value problem (Pedlosky, 2003):

$$\frac{d^2w(z)}{dz^2} + {K_H}^2\frac{(N(z)^2-\omega^2)}{(\omega^2-f^2)}w(z) = 0 \qquad (5.1)$$

$$w = 0, z = 0, -h \qquad (5.2),$$

where ω is the wave frequency, K_H is the horizontal wave number, h is the water depth, f is the inertial frequency, and w is the vertical velocity component. The eigenvalue K_{Hn} and

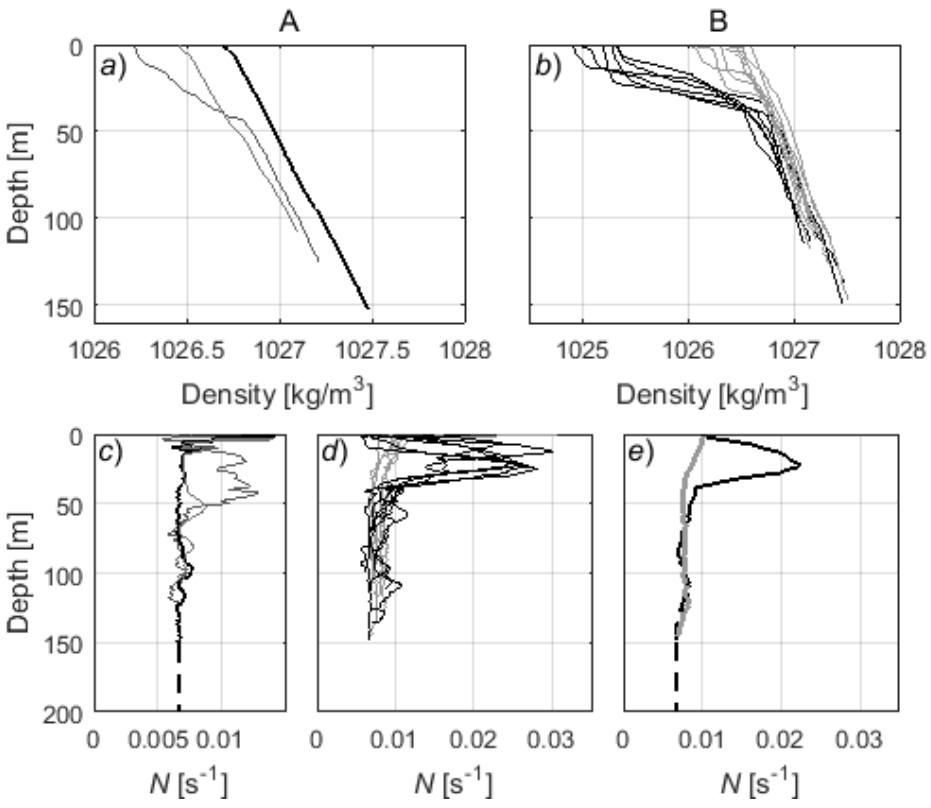

Figure 5.2. Vertical profiles of density (top) and *N* (bottom) at sites A (*a* and *c*) and B (*b* and *d*). At site B, the grey and black lines represent austral early spring and late summer, respectively. Also shown are the averaged spring and late summer profiles of *N* at site B (*e*). The extrapolated constant values of *N* are shown as dashed lines.

Table 5.1. A summary of the locations and dates of hydrographic stations.

Site A	Latitude	Longitude	Date
1	-43.6638	-59.7982	9/9/2006
2	-43.7983	-59.6722	10/15/2005
3	-44.338	-59.974	11/5/1993
Site B	Latitude	Longitude	Date
1	-41.0833	-57.1257	2/8/1990
2	-41.1233	-57.345	3/23/1989
3	-40.47	-56.665	3/9/1994
4	-41.544	-57.725	3/10/1994
5	-40.55	-56.6667	3/22/1989
6	-41.7083	-57.875	3/23/1989
7	-41.4917	-57.645	9/5/1989
8	-41.7932	-57.8097	9/4/1997
9	-41.5292	-57.6095	9/5/1997
10	-41.2292	-57.3588	9/5/1997
11	-41.049	-57.225	10/10/2005
12	-40.9883	-57.1083	10/21/1997
13	-40.55	-56.7517	10/21/1997

the corresponding eigenvector $w_n(z)$ for the n^{th} normal mode were found for specified ω (representing the semidiurnal frequency) and $N(z)$. The derivatives in (1) were approximated with finite differences. The water depth was set at 200 m and the water column was discretized with 199 internal grid points.

Since eigenvectors of IW normal modes are expressed in terms of w (z), they are converted into corresponding eigenvectors of the horizontal velocity component u (so that the comparison with mooring data can be made) through the continuity equation:

$$\nabla \cdot \vec{u} = 0 \qquad (5.3),$$

where $\vec{u}$ is the velocity vector $\vec{u} = \vec{\imath}u + \vec{\jmath}v + \vec{k}w$. Assuming for simplicity that the wave vector $\overrightarrow{K_h}$ is aligned with the x-axis, the nth mode eigenvector of the horizontal velocity component u is:

$$u_n(z) = \frac{1}{K_H}\frac{dw_n(z)}{dz} \qquad (5.4)$$

With this orientation of the wave vector, $u_n(z)$ and $v_n(z)$ have the same vertical profiles, but the ratio of their amplitudes is ω/f. That is, the actual orientation of the horizontal wave vector is immaterial for the identification of IW modes in the observational data.

In the following analysis, we retain a standard decomposition of the horizontal velocity vector into its eastward u and northward v components, and do not refer to frequently used alongshelf and across-shelf components (as was done for instance by Valla and Piola, 2015). The main reason for this is that the IW velocity vectors (a primary focus of our study) do not reveal strong polarization, as will be shown below. The barotropic

velocity component was calculated as depth-averaged of all 7 water layers recorded, from 10 m to 160 m. The baroclinic velocity component in each water layer was calculated as a difference between the observed velocity and the depth-averaged velocity. Spectral energy and cross-spectral coherence of the velocity components were calculated to analyze the signal strength at the semidiurnal frequency. The spectral analysis was performed by applying Fast Fourier Transform. Time series were subdivided into 512 h-long segments overlapping by 50%. Along with velocity components, temperature records at site A were also analyzed by means of the spectral analysis.

The semidiurnal tidal species in the time series were singled out by applying a band-pass Lanczos-cosine filter (Duchon, 1979) with frequency bands of $\Delta f = [f_{c1} = 1.3,\ f_{c2} = 3.3]$ cycles per day, where f_{c1} and f_{c2} are the high-pass and low-pass cut-off frequencies respectively. The Lanczos-cosine filter is defined by

$$\omega_k = \left(\frac{\sin(2\pi k f_{c2})}{k\pi} - \frac{\sin(2\pi k f_{c1})}{k\pi}\right) \frac{\sin(\frac{k\pi}{M})}{k\pi/\mathrm{M}} \qquad (5.5),$$

where $k = 1, 2, \ldots, M$. We used $M = 20$ as the total sum of weights. For chosen parameters, the filter efficiently eliminates the near inertial, as well as high frequency ($\omega > 3.5\text{x}10^{-5}$ Hz) variability.

For band-passed velocity components, principal axis analysis (Freeland et al., 1975) was performed and revealed the tidal ellipses of barotropic and baroclinic velocity components.

The IW propagation can be characterized by the baroclinic energy flux defined in Chapter 2 (2.20). Since the vertical resolution in mooring data was too coarse for an

accurate integration of (2.21), especially in the lower part of the water column, we constructed a proxy for the energy flux as follows. As the water column was primarily thermally stratified at site A (e.g., Bianchi et al., 2005), we used a band-passed temperature record in the middle of the water column at depth z_1 (taken with a minus sign) as a proxy for the density perturbation. Specifically, we selected z_1 corresponding approximately to the maximum of w_n (or, equivalently, the nodal point of u_n) in the first IW mode which, as will be shown below, dominated the IW response at the shelf break. For the horizontal velocity, we selected the depth z_2 below z_1 where the baroclinic velocity signal was strongest (near the bottom as will be subsequently shown). The energy flux proxy is thus defined as

$$\vec{F}' = -\hat{u}_H(z_2)\hat{T}(z_1) \quad , \tag{5.6}$$

where $\hat{T}$ is the temperature and the hat symbol refers to the band-passed time series.

5.3 RESULTS

At site A, all density profiles reveal a near-constant buoyancy frequency ($N \sim 0.007$ s^{-1}) below 70 m depth. Early in the spring season, N remains nearly constant throughout the water column, while later in the spring (November) N increases in the upper 50 m reaching 0.012-0.013 s^{-1} (Figure 5.2c). Similarly, at site B, all profiles have a near-constant N below 50 m (~0.007-0.008 s^{-1}) regardless of the season, and a well-pronounced near surface maximum (~0.02-0.03 s^{-1}) for the late austral summer (Figure 5.2d).

For calculating the IW properties at site A, the N profile sampled during the mooring deployment (heavy line in Figure 5.2c) was utilized. For site B, available N profiles were averaged in two groups, representing austral early spring and late summer

(Figure 5.2e). Since the nominal depth of both mooring buoys was 200 m, *N* profiles were extrapolated to 200 m depth at constant values shown as dashed lines in Figures 5.2c and 5.2e.

Vertical profiles of horizontal velocity for the three lowest IW modes at semidiurnal frequency corresponding to the three *N* profiles (site A, site B early spring, and site B late summer) are shown in Figure 5.3. For both *N* profiles corresponding to the austral spring (Figure 5.3a and b), normal modes closely resemble analytical solutions based on the constant *N* (e. g., Pedlosky, 2003): nodes are uniformly spaced in the vertical, while vertical profiles resemble a cosine function with constant amplitude. For the surface-intensified stratification of the late summer (Figure 5.3c), normal modes exhibit moderate near-surface intensification (especially well pronounced for the first mode), while nodes in the upper 100 m also slightly shift upward. The phase speed $C=\omega/K_H$ for the first (gravest) mode varies from 0.45 m/s (site A) to 0.55 m/s (site B late summer).

The spectral analysis (Figure 5.4) of the zonal and meridional velocity components shows a strong semidiurnal barotropic signal at both sites. The baroclinic signals at the semidiurnal frequency have mixed strengths. Near the bottom (160 m), the spectral energy of both *u* and *v* components at site A are of comparable intensity to the barotropic signal. In particular, the *u* component at A is weaker than the barotropic signal, whereas the *v* component is stronger, suggesting a possible change in the orientation of the tidal ellipse from barotropic to baroclinic modes. At site B, both *u* and *v* components are weaker than the barotropic signal; nonetheless, the spectral energy is still more than 10% of the barotropic signal.

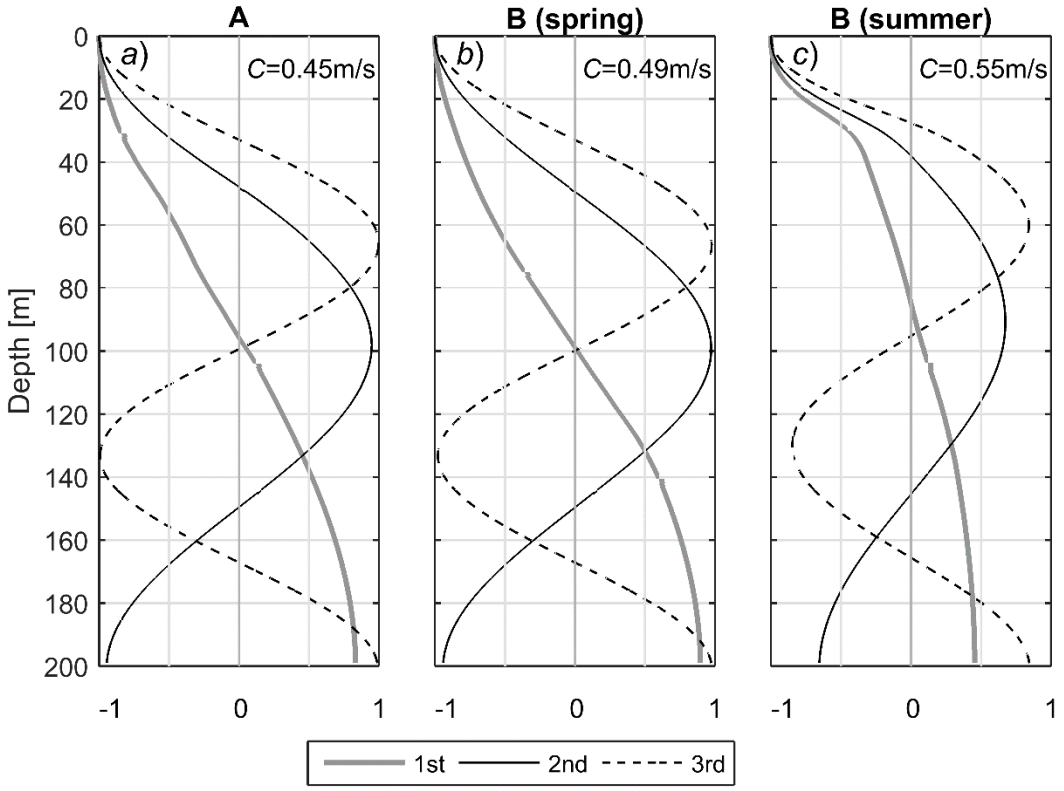

Figure 5.3. Vertical profiles of horizontal velocity of the three lowest IW modes at mooring sites A (*a*) and B (*b*: spring and *c*: late summer).

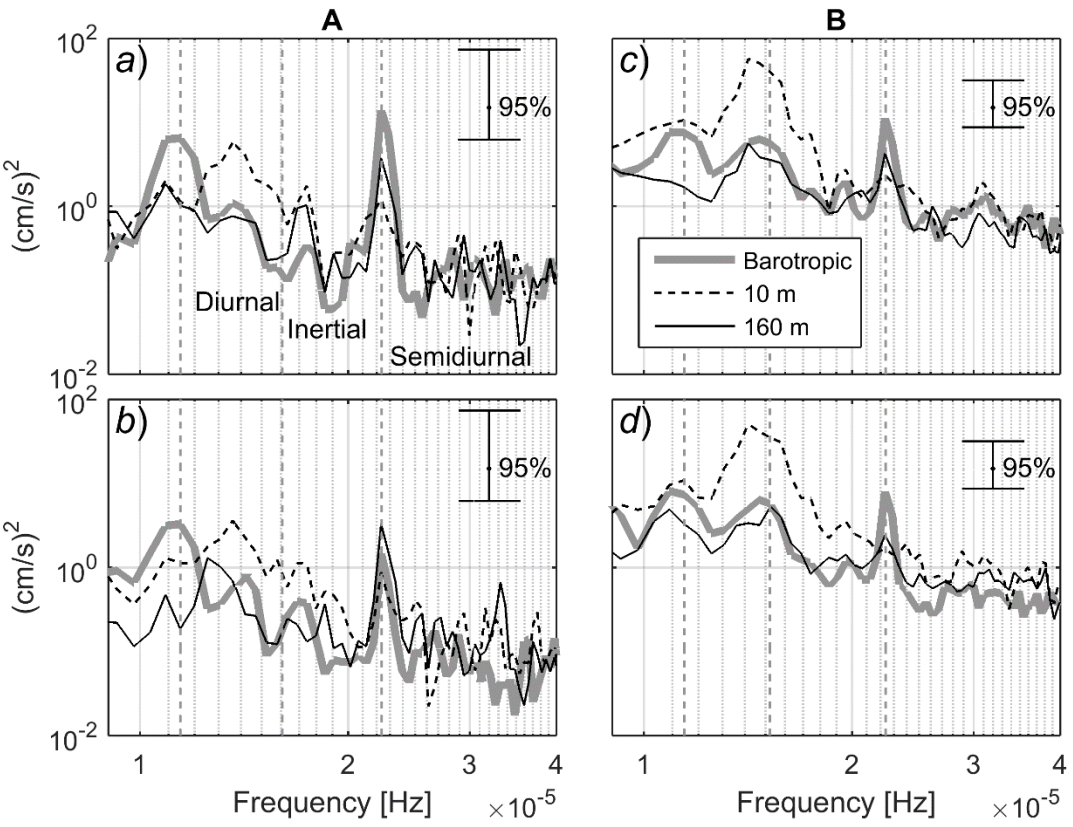

Figure 5.4. Spectral energy of horizontal velocity components at mooring A (left column) and B (right column): *u*-component at A (*a*), *v*-component at A (*b*), *u*-component at B (*c*), and *v*-component at B (*d*).

At the near-surface level (10 m), the spectral energy of the baroclinic velocity exhibits very strong inertial signals, especially at site A, but somewhat weaker semidiurnal signals. Surface intensification of near-inertial oscillations suggests their wind-driven origin. All baroclinic semidiurnal signals at mid-depths are weaker than both surface and bottom signals and thus are not shown in Figure 5.3. The relatively stronger velocity near the top and bottom of the water column at the semidiurnal frequency is in agreement with the theoretical structure of the first IW mode.

The spectral analysis reveals strong baroclinic components in velocity oscillations at diurnal, inertial and semidiurnal frequencies at both locations, likely associated with wave dynamics. While at diurnal and semidiurnal frequencies these oscillations are of tidal origin, the near inertial oscillations are wind-driven, their energy radiates downward and decays with depth (e.g., Rivas and Piola, 2005). At all three frequencies, the coherence (Figure 5.5) between baroclinic velocities at 10 m and deeper layers is high, suggesting the presence of the lowest vertical modes. Among these three frequency bands, the semidiurnal oscillations have the highest coherence. At site A, the coherence is higher overall than at site B, but the structure is similar and hence is not shown.

Phase differences between the baroclinic velocity components at 10 m depth and deeper layers delineate the vertical structure of semidiurnal baroclinic oscillations (Figure 5.6). At location A, the near-surface and near-bottom oscillations have approximately opposite phase (~180° phase difference), and the sign reversal occurs in the middle of the water column (Figure 5.6a and b), where the phase difference exceeds 90°. This observed structure compares favorably with the first IW mode profile inferred from the CTD profiles (Figure 5.3a). At site B, the *u* component resembles the structure in Figure 5.6a, but the

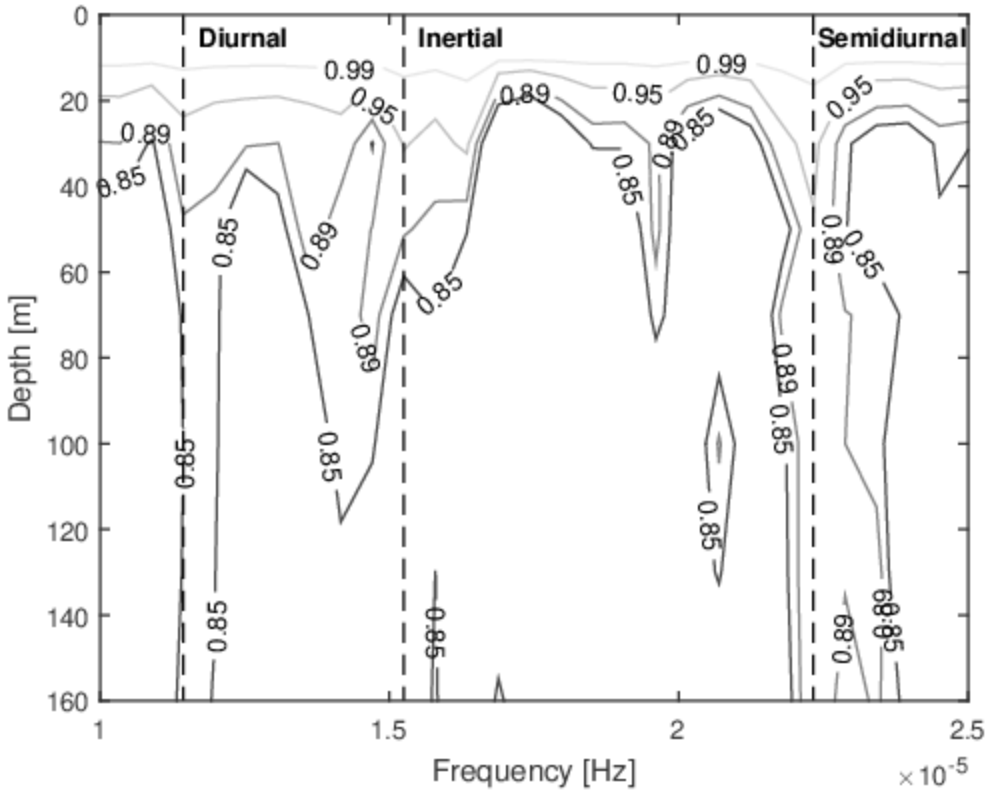

Figure 5.5. Mooring B, coherence of baroclinic velocity component *u* at 10 m and 30, 50, 70, 100, 130 and 160 m bins. The 95% confidence interval of zero coherence is 0.28.

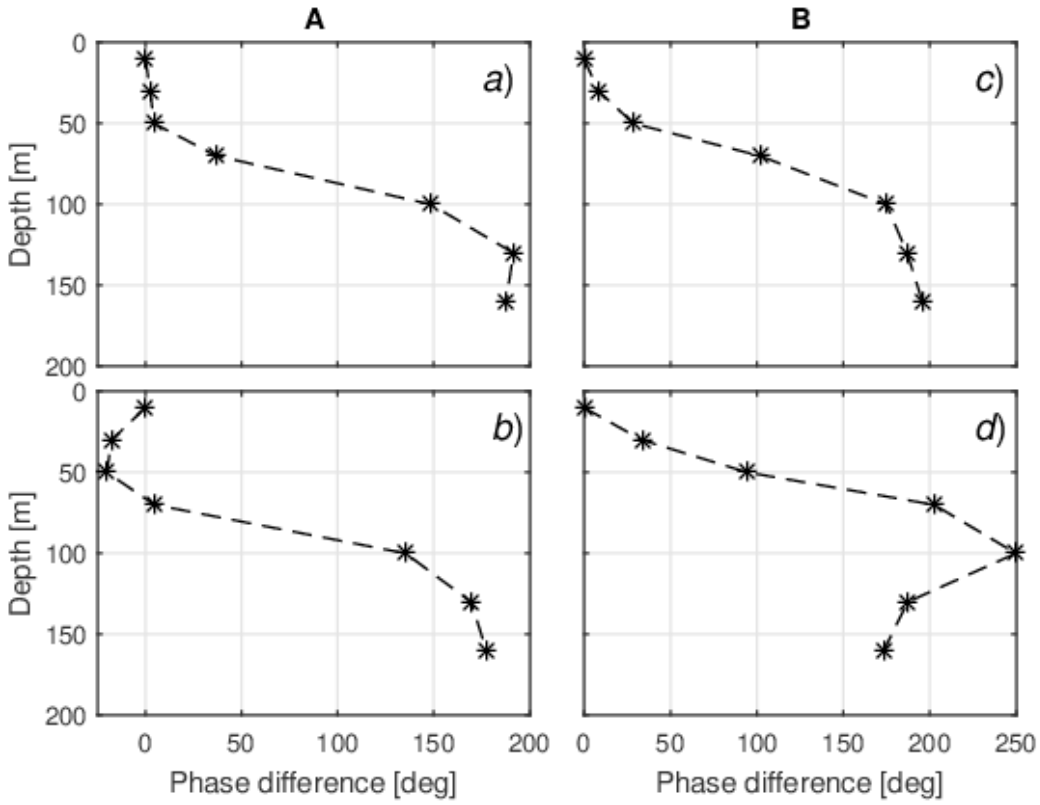

Figure 5.6. Phase differences at the semidiurnal frequency between the near-surface and deeper bins for baroclinic velocity at mooring A (left column) and B (right column): *u*-component at A (*a*), *v*-component at A (*b*), *u*-component at B (*c*), and *v*-component at B (*d*).

irregularity of phase difference (Figure 5.6d) observed in the *v* component suggests that higher modes are present in the IW field. For both velocity components at site B, the phase reversal occurs at a shallower depth than at site A.

We further investigate the IW structure at sites A and B by estimating the spectral amplitudes of the baroclinic velocity components *u* and *v* at the semidiurnal frequency and normalizing them by the spectral amplitude of the barotropic velocity magnitude at the corresponding location (Figure 5.7). The sign of the velocity components is determined from the phase difference shown in Figure 5.6: the positive sign is assigned at the bottom and it is reversed to negative where the phase difference exceeds 90°. For comparison, we also plot the theoretical profile of the first IW mode at location A: at this site, the spectral amplitudes of the baroclinic velocities intensify in the upper and lower layers, and diminish at mid-depth. For site B, the velocity amplitudes do not show a clear decrease in the middle of the water column (especially for the *u*-component) indicating the presence of higher modes. The maximum baroclinic velocity components at both locations reach approximately 40-50% of the barotropic velocity magnitude at the semidiurnal frequency. A difference between the theoretical and observed distribution of velocity amplitude with depth is that the observed semidiurnal oscillations have a higher amplitude near the bottom, while for the predicted first mode the maximum velocity is at the surface. This discrepancy can be explained by the IW generation at the shelf break (near the bottom) and the contribution of higher modes. Overall, semidiurnal IWs at location B appear to have higher amplitude expressed as a fraction of the barotropic velocity amplitude compared to location A. This can be due to the different period of observations, which includes the summer season at site B.

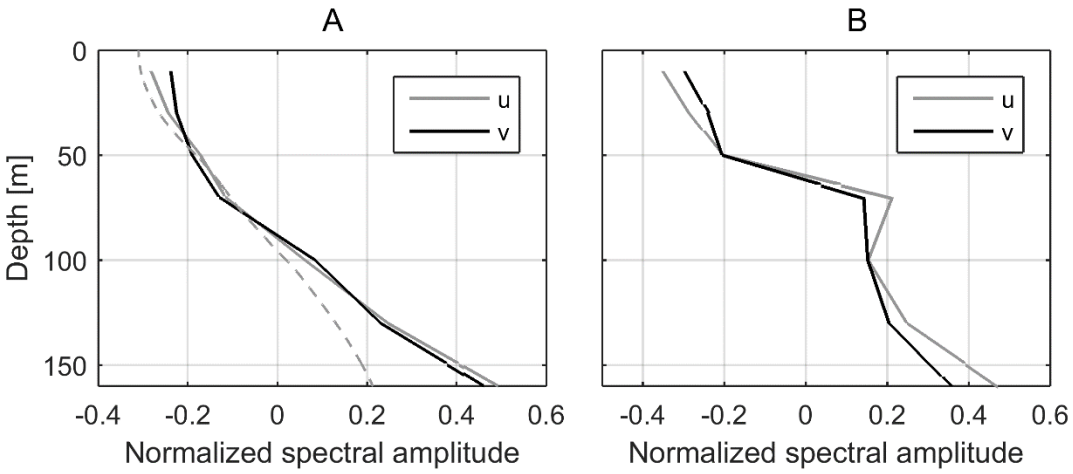

Figure 5.7. Spectral amplitudes of *u* (grey) and *v* (black) baroclinic velocity components at the semidiurnal frequency, mooring A (left column) and B (right column). The amplitudes are normalized by the semidiurnal spectral amplitude of barotropic velocity magnitude from the corresponding mooring. The corresponding theoretical first mode profile for A is shown for comparison as a dashed line.

Spectral analysis of temperature records at site A shows that semidiurnal oscillations are the most energetic in the superinertial frequency band indicating significant IW activity (Figure 5.8). Overall, strong semidiurnal temperature signals are observed at mid-depth (50-100 m), consistent with the first mode structure. The maximum spectral energy is at 50 m and decreases at 100 m, which might be related to the development of a seasonal thermocline during the later stage of mooring deployment.

Further analysis is performed on band-passed time series of temperature, as well as barotropic and baroclinic velocity components, which retain only a semidiurnal frequency band (semidiurnal tidal species). The principal axis analysis of barotropic band-passed currents demonstrates that semidiurnal tidal ellipses are polarized in the cross-isobath direction (Figure 5.9a and d). This result is consistent with regional numerical models of tidal dynamics (e.g., Glorioso and Flather, 1997). Baroclinic tidal currents are less polarized; near the surface (10 m depth), their principal axes are still oriented in a cross-isobath direction, but tidal ellipses are less elongated than in barotropic currents (Figure 5.9b and e). The polarization of baroclinic tidal ellipses becomes even weaker in the near-bottom layer (Figure 5.9c and f), and the principal axes are no longer oriented in the cross-isobath direction (especially at location B).

Lack of clear polarization of baroclinic tidal ellipses implies that there is no predominant direction for the internal tide propagation. We assess variations in the IW energy flux direction based on mooring records at location A (where the temperature data are available) by estimating the energy flux proxy (5.6). For z_1, we select 100 m depth (rather than 50 m) in order to minimize the influence of the atmospheric forcing on the temperature record. In addition, this depth corresponds to the maximum vertical velocity

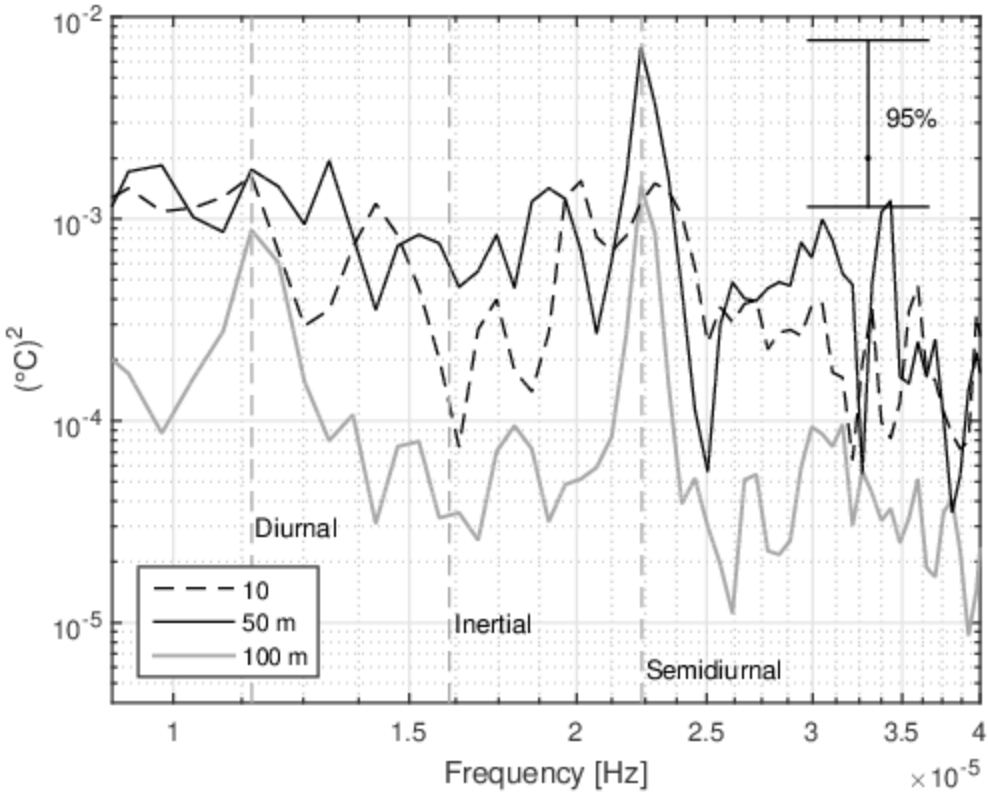

Figure 5.8. Spectral energy of temperature at site A at 10, 50 and 100 m.

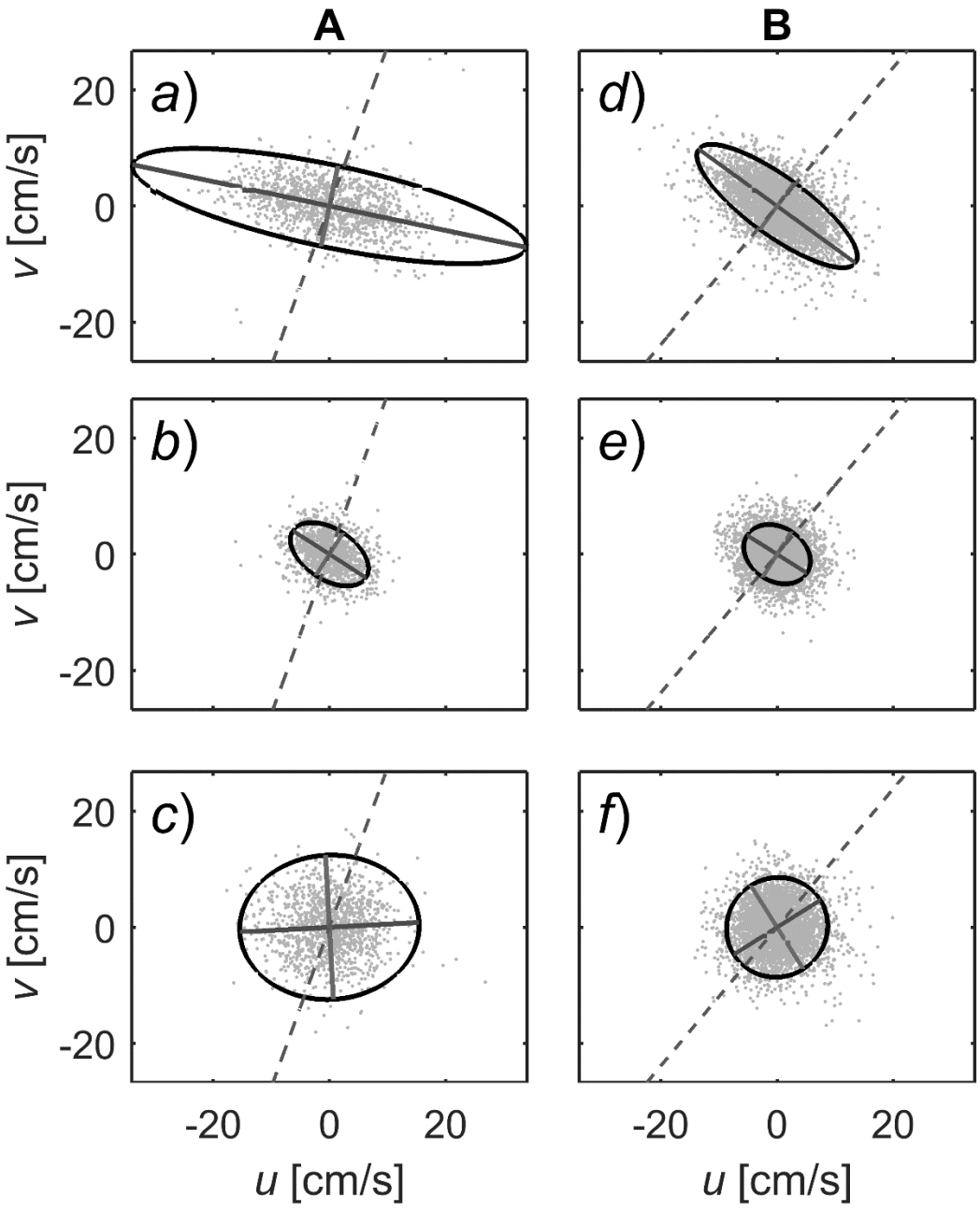

Figure 5.9. Principal axis analysis of band-passed velocity records at mooring A (left column) and B (right column): barotropic velocity (*a*, *d*); baroclinic velocity at 10 m (*b*, *e*) and 160 m (*c*, *f*). Grey dots are velocity data; principal/minor axis is shown in black/grey. Dashed line indicates the shelf break orientation at the corresponding mooring site.

and isopycnal displacement in the first IW mode. For z_2, we select 160 m depth, where semidiurnal baroclinic currents are strongest. Proxy vectors are averaged over 12 h and sampled at a 1 h time interval; in addition, the original barotropic velocity (not band-passed) is averaged over the same 12 h intervals and is referred to as the mean current. The resulting mean current velocity magnitude values are binned in four equal groups separated by three quartiles. Proxy vectors in Figure 5.10 are color-coded depending on the particular mean current group, which visualizes the mean current influence on the internal tide propagation. In addition, proxy vectors with *x* and *y* components both smaller than their corresponding standard deviations are discarded, which leaves only relatively strong signals depicted in Figure 5.10.

Relatively few proxy vectors (and of a smaller magnitude) are oriented in the direction normal to local isobaths, pointing either inshore or offshore. This would be a preferential direction based on the theory of the IW generation by barotropic tides at the shelf break (e.g., Baines, 1982). A majority of proxy vectors have significant upstream (southward) component, against the MC direction. This tendency is especially obvious for proxy vectors with larger magnitudes (longer vectors in Figure 5.10) and those corresponding to stronger mean current (magenta and red vectors). There are some proxy vectors pointing downstream (northeastward) but they are all of small magnitude falling below the screening threshold mentioned in the previous paragraph, and as such are not shown in Figure 5.10. We conclude that the presence of the MC strongly affects the direction of the IW radiation from the Patagonian shelf break by deflecting IWs upstream relative to the MC direction.

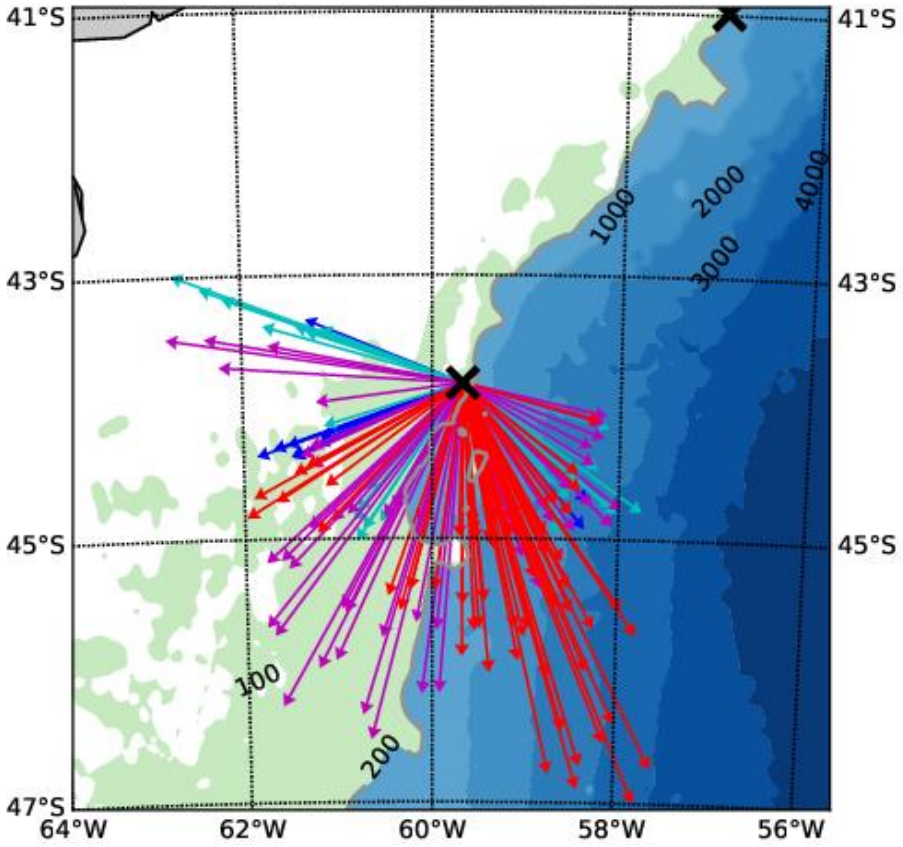

Figure 5.10. Proxy vectors of the baroclinic energy fluxes at site A. Vector colors represent four groups of the mean current speed in the order of its increase: blue, cyan, magenta, and red.

We illustrate this conclusion by plotting the meridional component of proxy vectors against the mean current velocity magnitude (Figure 5.11). The mean current velocity ranges from ~20 cm/s to over 70 cm/s so that during certain time intervals the mean current becomes supercritical relative to the IW phase speed. The proxy vector meridional component increases with the mean current speed, but the trend is not linear. The highest values of the southward proxy vector component correspond to the mean current speed ranging from 40 to 60 cm/s, when the mean current speed is comparable with the IW phase speed and the mean flow is in near-critical condition. Also, it should be noted that the proxy vector indicates the energy flux direction in the frame moving with the mean current. This implies that the actual direction of the IW propagation under supercritical conditions is to the north.

5.4 DISCUSSION AND CONCLUSIONS

The Patagonian Shelf region is characterized by semidiurnal tides with both tidal amplitudes and dissipation rates being among the highest in the World Ocean, as shown by the satellite altimetry data analysis (e.g., Egbert and Ray, 2001). While barotropic semidiurnal tidal species in this region generally propagate northward, in the direction of Kelvin wave phase propagation, high resolution numerical models also reveal a strong onshore energy flux in the zonal band from 44°S to 41°S (e.g., Palma et al., 2004). Energetic cross-isobath tidal currents combined with a relatively strong seasonal stratification should lead to IW generation along the Patagonian shelf break (e.g., Baines, 1982), at least in its northern part, which is the study area for this paper. On the other hand, there is no evidence for internal tide radiation from this region into the open ocean in

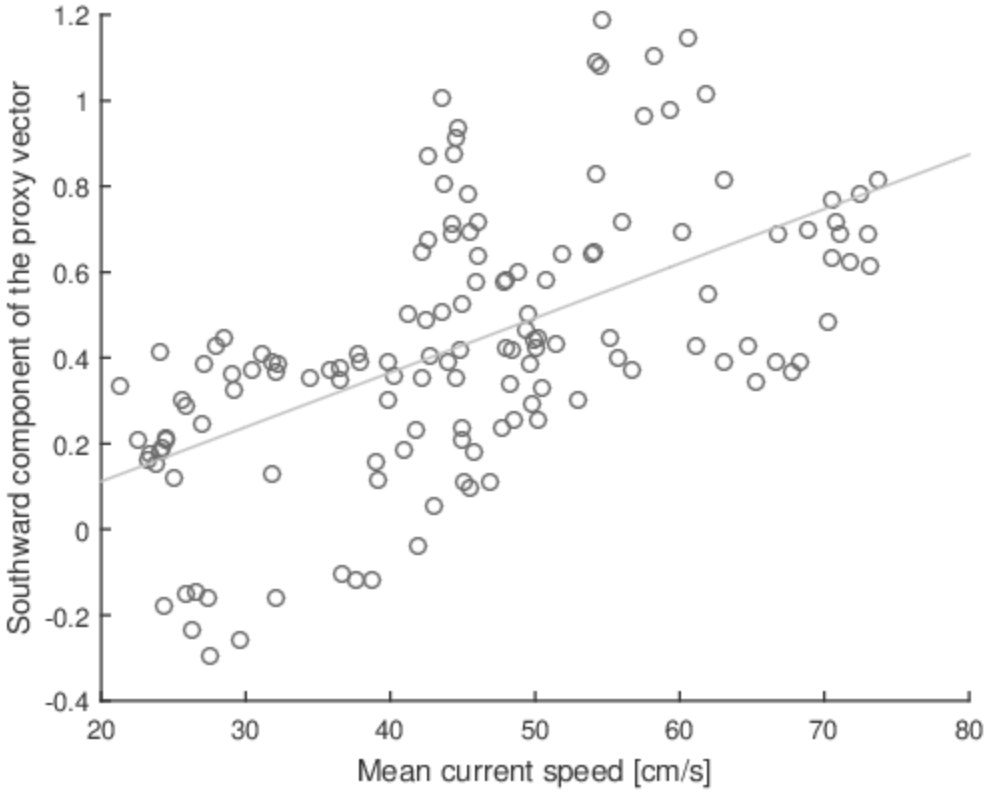

Figure 5.11. Meridional component (positive southward) of the proxy vector versus the barotropic mean current speed. Linear regression is shown as a grey line.

remotely-sensed data (Zhao et al., 2016) and in numerical simulations (e.g., Simmons et al., 2004).

Our analysis of the current velocity and temperature time series from two moorings deployed along the 200-m isobath confirms the presence of strong semidiurnal internal tides. The spectral amplitude of the baroclinic velocity at the semidiurnal frequency near the bottom exceeds 40% of the corresponding barotropic velocity amplitude at both locations. The vertical profiles of the velocity spectra and phase difference suggest that internal tides at the shelf break are predominantly the first IW mode. However, unlike the theoretical first mode structure, the observed vertical structure of the baroclinic velocity at semidiurnal frequency is bottom-intensified, likely due to the contribution of higher modes.

The observed barotropic tidal currents are strongly polarized in the across-isobath direction. The baroclinic semidiurnal currents do not follow this pattern: the eccentricity of baroclinic tidal ellipses is smaller than in barotropic currents, especially near the bottom. Since the principal axis of baroclinic oscillations should be aligned with the horizontal wave vector when the wave frequency is higher than f (e.g., Pedlosky, 2003), the lack of polarization implies that there is no dominant direction for the semidiurnal IW radiation. By defining a proxy for the IW energy flux, we found that IW deflection from radiation across the isobaths is related to the mean current velocity magnitude: a stronger mean current causes IW energy to propagate southward, along the continental slope and upstream relative to the mean current direction. This pattern can result from the IW refraction on the mean current, when the wave vector turns in the direction of the minimal propagation speed, southward in our case.

Mean circulation in the study area is primarily associated with the Malvinas Current. Recent studies based on the analysis of shipboard surveys, satellite-tracked drifters, and remotely-sensed data (Piola et al., 2013), as well as on numerical modeling (e.g., Combes and Matano, 2014) revealed a rather complex structure of the MC, comprising multiple jets and hydrographic fronts (Franco et al., 2008). On average, two major jets can be identified; one is associated with the shelf break (~200 m isobath), and the other is at the continental slope plateau, where bottom slope has a local minimum (~1400-m isobath). Multiple jets tend to merge north of 45°S in averaged data with the MC core at the surface reaching 0.8-1 m/s between 1000- and 2000-m isobaths (Combes and Matano, 2014). However, instantaneous snapshots of the MC structure do show the presence of multiple jets and otherwise rich variability of the MC in our study area.

Barotropic tidally-averaged current speeds in the study area (site A) varied from ~0.2 to over 0.7 m/s, while the first IW mode phase speed ranged from ~0.45 m/s in the beginning of seasonal warming to ~0.55 m/s under the maximum seasonal stratification. Clearly, the mean current frequently reached a supercritical regime, exceeding the IW phase speed. As waves refract in the direction roughly parallel to the mean current, the existence of critical layers (where the mean current matches the IW phase speed) can in general inhibit IW propagation and lead to IW dissipation, turbulent mixing and homogenizing of the stratified water column (e.g., Baines, 1995). Even if IWs initially escape the deflecting effect of the mean current and radiate offshore when the mean current at the shelf break is weak, they are likely to refract and encounter a critical layer farther offshore, as they approach the maximum MC velocity. It also should be noted that the MC advects cold Antarctic water and thus the thermal stratification at its core is reduced (e.g.,

Piola et al., 2010), affecting the IW phase speed. We conclude that the overall impact of the MC on the internal tides generated at the shelf break in the study area is that their predominant propagation is in the along-shelf direction, which can lead to enhanced local dissipation.

The MC can directly generate IWs by interacting with along-shelf topographic irregularities, when the wavelength matches the length scale of the topographic feature. Such IWs were the subject of a recent study by Magalhães and da Silva (2017) and were evident in satellite images as trains of steep IWs propagating against the MC. Magalhães and da Silva (2017) argued that the observed waves were in a near-critical (transcritical in their terminology) regime. However, our analysis reveals that semidiurnal internal tides also propagate against the MC and their phase speed on many occasions nearly matches the mean current velocity. Hence, semidiurnal internal tides can also disintegrate into high-amplitude internal wave trains as they approach a near-critical regime and the two mechanisms for internal wave generation can be undistinguishable in the remotely sensed images reported by Magalhães and da Silva (2017). Unfortunately, in this study we could not analyze high frequency IWs and their possible link to the barotropic tidal forcing due to 1-hour sampling interval of mooring records.

With a phase speed of ~0.5 m/s, semidiurnal IWs in the study area should have a wavelength of ~25 km. Their adequate resolution as they propagate along the shelf break will require a horizontal resolution of less than 5 km. Furthermore, the IW overturning and dissipation in the presence of a critical layer can be better represented in a non-hydrostatic model. It appears that global tidal models in their present configuration do not adequately resolve these dynamics. Nevertheless, these IWs can be important both in terms of

barotropic tidal energy dissipation and turbulent mixing in the MC, as well as in other western boundary currents adjacent to broad continental shelves. Parameterization of these effects in numerical models merits future investigation.

.

CHAPTER 6

CONCLUSION AND DISCUSSIONS

Tidal waves propagate along the continental shelves as Kelvin waves. At semidiurnal frequency, only a fundamental zero wave mode exists among trapped wave modes, while higher modes merge with the continuum of radiating Poincaré waves. When the semidiurnal Kelvin wave mode propagates along a wide continental shelf, the wide shelf topography modifies the Kelvin wave into a hybrid Kelvin-edge wave. At low wave numbers, the wave mode resembles a Kelvin wave, with its free surface structure decaying offshore over a Rossby radius of the open ocean. At high wave numbers, the wave mode resembles an edge wave, with its free surface structure confined on the shelf. When the propagating zero mode encounters a variation in shelf width, its wave structure adjusts according to the shelf width. This wave structure adjustment can result in a reversal of the alongshore energy flux over the continental shelf. At the region where the shelf width changes, the propagating zero wave mode can scatter into other wave modes, including barotropic and baroclinic Poincaré waves radiating offshore. This process is simulated under both barotropic and stratified conditions.

In the barotropic model, the adjustment leads to a divergence in the alongshore energy fluxes over the continental shelf with compensating cross-isobath energy fluxes. The direction of the cross-isobath energy flux depends on the HKEW's cross-shelf energy flux structures. A divergence in the alongshore energy flux leads to the generation of

onshore energy fluxes, and reversely, a convergence in the alongshore energy flux leads to the generation of offshore energy fluxes. The magnitude of the cross-isobath energy fluxes is affected by the magnitude of change in alongshore energy structures and the scattering of the incident wave mode into Poincaré waves. For example, the strongest cross-isobath energy flux in the barotropic model occurs when the shelf width narrows from 300 km to 250 km. In this case the strong convergence of alongshore energy fluxes generates an offshore energy flux with a comparable magnitude.

In the stratified model, the incident zero mode can scatter into baroclinic wave modes. The scattering can generate a significant baroclinic radiation extending from the scattering region to several hundred kilometers downstream. The strength of the baroclinic radiation depends not only on the potential intensity of barotropic energy flux divergence, but also on how well the vertical structure of the internal wave modes matches the barotropic forcing over the shelf break, as well as the number of available internal wave modes with structures that fit the incident wave structure to maintain the continuity of pressure and velocity fields. The strongest baroclinic radiation in the stratified model shows that the incident wave can scattering approximately 15% of the barotropic energy flux into baroclinic radiation. Model runs with an offshore barotropic energy flux do not generate as much baroclinic radiation as the model runs with an onshore barotropic energy flux. In these cases, the scattering of the incident energy into barotropic Poincaré waves is more significant than baroclinic Poincaré waves. The internal wave generation is more significant when the alongshore energy flux diverges at the scattering region.

The model simulations in this study are particularly relevant to areas in the world ocean characterized by energetic semidiurnal tides and wide continental shelves, such as

the Celtic Sea and the Patagonian shelf. The Celtic Sea is known for its intense internal wave field at the Celtic Sea Shelf. The Patagonian shelf break to the contrary, has not been regarded as an area with strong internal tide generation. The analysis of the CTD and ADCP data from the locations at the Patagonian shelf break demonstrates the existence of semidiurnal internal waves. The spectral amplitude of the baroclinic velocity at the semidiurnal frequency near the bottom exceeds 40% of the barotropic velocity. The analysis of energy fluxes shows that the internal waves deflects from radiating across isobath and propagate predominantly along isobaths. This refraction is related to the mean current velocity magnitude. A stronger mean current causes IW energy to propagate southward, along the continental slope and upstream with respect to the mean current direction. This suggest that the MC has a significant impact on the internal wave field. The current speed of the MC in the study area on many occasions is higher than the IW phase speed. The presence of critical layers can inhibit the IW propagation and enhance the IW dissipation.

This study has demonstrated that semidiurnal tides can generate a substantial amount of baroclinic energy radiation on wide continental shelves. This internal wave generation mechanism prompts a new approach to tidal dissipation schemes on wide continental shelves. Based on the observation on the Patagonian shelf, a future research direction is to model the baroclinic radiation in the presence of fast western boundary currents. The effect of mean currents on the IW generation and propagation can be simulated and parameterized in numerical models. The parameterization of the scattering intensity can lead to a re-evaluation of global conversion into baroclinic modes off the

continental shelf break. This model can be applied to the areas such the Patagonian Shelf and provide new insights for the significance of tidal mixing in the ocean interior.

.

REFERENCES

Artana, C., R. Ferrari, Z. Koenig, M. Saraceno, A. R. Piola, and C. Provost, 2016: Malvinas Current variability from Argo floats and satellite altimetry. *J. Geophys. Res. Oceans*, **121**, 4854–4872, doi:10.1002/2016JC011889.

Baines, P. G., 1973: The generation of internal tides by flat-bump topography. *Deep Sea Research and Oceanographic Abstracts*, **20**, 179–205, doi:10.1016/0011-7471(73)90050-8.

——, 1982: On internal tide generation models. *Deep Sea Research Part A. Oceanographic Research Papers*, **29**, 307–338, doi:10.1016/0198-0149(82)90098-X.

Baines, P. G., 1995: *Topographic Effects in Stratified Flows*. Cambridge University Press, 508 pp.

Bell, T. H., 1975: Topographically generated internal waves in the open ocean. *J. Geophys. Res.*, **80**, 320–327, doi:10.1029/JC080i003p00320.

Bianchi, A. A., L. Bianucci, A. R. Piola, D. R. Pino, I. Schloss, A. Poisson, and C. F. Balestrini, 2005: Vertical stratification and air-sea CO2 fluxes in the Patagonian shelf. *J. Geophys. Res.*, **110**, C07003, doi:10.1029/2004JC002488.

——, and Coauthors, 2009: Annual balance and seasonal variability of sea-air CO2 fluxes in the Patagonia Sea: Their relationship with fronts and chlorophyll distribution. *J. Geophys. Res.*, **114**, C03018, doi:10.1029/2008JC004854.

Breiman, L., 2001: Random Forests. *Machine Learning*, **45**, 5–32, doi:10.1023/A:1010933404324.

Brink, K. H., and D. C. Chapman, 1985: *Programs for computing properties of coastal-trapped waves and wind-driven motions over the continental shelf and slope*. Woods Hole Oceanographic Institution, http://darchive.mblwhoilibrary.org/handle/1912/5363 (Accessed February 25, 2018).

Briscoe, M. G., 1975: Preliminary results from the trimoored internal wave experiment (IWEX). *J. Geophys. Res.*, **80**, 3872–3884, doi:10.1029/JC080i027p03872.

Buijsman, M. C., Y. Uchiyama, J. C. McWilliams, and C. R. Hill-Lindsay, 2011: Modeling Semidiurnal Internal Tide Variability in the Southern California Bight. *J. Phys.*

Oceanogr., **42**, 62–77, doi:10.1175/2011JPO4597.1.

——, B. K. Arbic, J. A. M. Green, R. W. Helber, J. G. Richman, J. F. Shriver, P. G. Timko, and A. Wallcraft, 2015: Optimizing internal wave drag in a forward barotropic model with semidiurnal tides. *Ocean Modelling*, **85**, 42–55, doi:10.1016/j.ocemod.2014.11.003.

Buijsman, M. C., and Coauthors, 2016: Impact of Parameterized Internal Wave Drag on the Semidiurnal Energy Balance in a Global Ocean Circulation Model. *J. Phys. Oceanogr.*, **46**, 1399–1419, doi:10.1175/JPO-D-15-0074.1.

Carter, G. S., M. C. Gregg, and R.-C. Lien, 2005: Internal waves, solitary-like waves, and mixing on the Monterey Bay shelf. *Continental Shelf Research*, **25**, 1499–1520, doi:10.1016/j.csr.2005.04.011.

Cartwright, D. E., and R. D. Ray, 1991: Energetics of global ocean tides from Geosat altimetry. *J. Geophys. Res.*, **96**, 16897–16912, doi:10.1029/91JC01059.

Chapman, D. C., 1985: Numerical Treatment of Cross-Shelf Open Boundaries in a Barotropic Coastal Ocean Model. *J. Phys. Oceanogr.*, **15**, 1060–1075, doi:10.1175/1520-0485(1985)015<1060:NTOCSO>2.0.CO;2.

Charo, M., and A. R. Piola, 2014: Hydrographic data from the GEF Patagonia cruises. *Earth System Science Data*, **6**, 265.

Combes, V., and R. P. Matano, 2014: A two-way nested simulation of the oceanic circulation in the Southwestern Atlantic. *J. Geophys. Res. Oceans*, **119**, 731–756, doi:10.1002/2013JC009498.

Dale, A. C., J. M. Huthnance, and T. J. Sherwin, 2001: Coastal-Trapped Waves and Tides at Near-Inertial Frequencies. *J. Phys. Oceanogr.*, **31**, 2958–2970, doi:10.1175/1520-0485(2001)031<2958:CTWATA>2.0.CO;2.

Di Lorenzo, E., W. R. Young, and S. L. Smith, 2006: Numerical and Analytical Estimates of M2 Tidal Conversion at Steep Oceanic Ridges. *J. Phys. Oceanogr.*, **36**, 1072–1084, doi:10.1175/JPO2880.1.

Duchon, C. E., 1979: Lanczos Filtering in One and Two Dimensions. *J. Appl. Meteor.*, 1016–1022, doi:https://doi.org/10.1175/1520-0450(1979)018<1016:LFIOAT>2.0.CO;2.

Egbert, G. D., and R. D. Ray, 2001: Estimates of M2 tidal energy dissipation from TOPEX/Poseidon altimeter data. *J. Geophys. Res.*, **106**, 22475–22502, doi:10.1029/2000JC000699.

——, and ——, 2003: Semi-diurnal and diurnal tidal dissipation from TOPEX/Poseidon altimetry. *Geophys. Res. Lett.*, **30**, 1907, doi:10.1029/2003GL017676.

Franco, B. C., A. R. Piola, A. L. Rivas, A. Baldoni, and J. P. Pisoni, 2008: Multiple thermal fronts near the Patagonian shelf break. *Geophys. Res. Lett.*, **35**, L02607, doi:10.1029/2007GL032066.

Freeland, H., P. Rhines, and T. Rossby, 1975: Statistical observations of trajectories of neutrally buoyant floats in North-Atlantic. *Journal of Marine Research*, **33**, 383–404.

Garrett, C., and W. Munk, 1972: Space-Time scales of internal waves. *Geophysical Fluid Dynamics*, **3**, 225–264, doi:10.1080/03091927208236082.

Garrett, C., and E. Kunze, 2007: Internal Tide Generation in the Deep Ocean. *Annual Review of Fluid Mechanics*, **39**, 57–87, doi:10.1146/annurev.fluid.39.050905.110227.

Gerkema, T., F. A. Lam, and L. R. M. Maas, 2004: Internal tides in the Bay of Biscay: conversion rates and seasonal effects. *Deep Sea Research Part II: Topical Studies in Oceanography*, **51**, 2995–3008, doi:10.1016/j.dsr2.2004.09.012.

Glorioso, P. D., and R. A. Flather, 1997: The Patagonian Shelf tides. *Progress in Oceanography*, **40**, 263–283, doi:10.1016/S0079-6611(98)00004-4.

Green, J. A. M., J. H. Simpson, S. A. Thorpe, and T. P. Rippeth, 2010: Observations of internal tidal waves in the isolated seasonally stratified region of the western Irish Sea. *Continental Shelf Research*, **30**, 214–225, doi:10.1016/j.csr.2009.11.004.

Haidvogel, D. B., and A. Beckmann, 1999: Numerical Ocean Circulation Modeling. *Numerical Ocean Circulation Modeling*, Vol. Volume 2 of *Series on Environmental Science and Management*, IMPERIAL COLLEGE PRESS, 283–286 http://www.worldscientific.com/doi/abs/10.1142/9781860943935_0008 (Accessed February 23, 2018).

Hansen, K. S., 1982: Secular effects of oceanic tidal dissipation on the Moon's orbit and the Earth's rotation. *Rev. Geophys.*, **20**, 457–480, doi:10.1029/RG020i003p00457.

Huthnance, J. M., 1975: On trapped waves over a continental shelf. *Journal of Fluid Mechanics*, **69**, 689–704, doi:10.1017/S0022112075001632.

Jackson, C., 2007: Internal wave detection using the Moderate Resolution Imaging Spectroradiometer (MODIS). *J. Geophys. Res.*, **112**, C11012, doi:10.1029/2007JC004220.

Jayne, S. R., and L. C. St. Laurent, 2001: Parameterizing tidal dissipation over rough topography. *Geophys. Res. Lett.*, **28**, 811–814, doi:10.1029/2000GL012044.

Jeffreys, H., 1921: Tidal Friction in Shallow Seas. *Philosophical Transactions of the Royal Society of London. Series A, Containing Papers of a Mathematical or Physical Character*, **221**, 239–264.

Kantha, L. H., and C. C. Tierney, 1997: Global baroclinic tides. *Progress in Oceanography*, **40**, 163–178, doi:10.1016/S0079-6611(97)00028-1.

——, C. Tierney, J. W. Lopez, S. D. Desai, M. E. Parke, and L. Drexler, 1995: Barotropic tides in the global oceans from a nonlinear tidal model assimilating altimetric tides: 2. Altimetric and geophysical implications. *J. Geophys. Res.*, **100**, 25309–25317, doi:10.1029/95JC02577.

Ke, Z., and A. E. Yankovsky, 2010: The Hybrid Kelvin–Edge Wave and Its Role in Tidal Dynamics. *J. Phys. Oceanogr.*, **40**, 2757–2767, doi:10.1175/2010JPO4430.1.

Kunze, E., and J. M. Toole, 1997: Tidally Driven Vorticity, Diurnal Shear, and Turbulence atop Fieberling Seamount. *J. Phys. Oceanogr.*, **27**, 2663–2693, doi:10.1175/1520-0485(1997)027<2663:TDVDSA>2.0.CO;2.

——, L. K. Rosenfeld, G. S. Carter, and M. C. Gregg, 2002: Internal Waves in Monterey Submarine Canyon. *J. Phys. Oceanogr.*, **32**, 1890–1913, doi:10.1175/1520-0485(2002)032<1890:IWIMSC>2.0.CO;2.

Lastras, G., J. Acosta, A. Muñoz, and M. Canals, 2011: Submarine canyon formation and evolution in the Argentine Continental Margin between 44°30'S and 48°S. *Geomorphology*, **128**, 116–136, doi:10.1016/j.geomorph.2010.12.027.

Laurent, L. S., C. Garrett, L. S. Laurent, and C. Garrett, 2002: The Role of Internal Tides in Mixing the Deep Ocean. *http://dx.doi.org/10.1175/1520-0485(2002)032<2882:TROITI>2.0.CO;2*,. https://journals.ametsoc.org/doi/abs/10.1175/1520-0485(2002)032%3C2882:TROITI%3E2.0.CO%3B2 (Accessed January 26, 2018).

Lozovatsky, I., P. Jinadasa, J.-H. Lee, and H. J. Fernando, 2015: Internal waves in a summer pycnocline of the East China Sea. *Ocean Dynamics*, **65**, 1051–1061, doi:10.1007/s10236-015-0858-2.

Magalhães, J., and J. da Silva, 2017: Internal Waves Along the Malvinas Current: Evidence of Transcritical Generation in Satellite Imagery. *Oceanography*, **30**, doi:10.5670/oceanog.2017.319. https://tos.org/oceanography/article/internal-waves-along-the-malvinas-current (Accessed September 24, 2017).

Marshall, J., C. Hill, L. Perelman, and A. Adcroft, 1997: Hydrostatic, quasi-hydrostatic, and nonhydrostatic ocean modeling. *J. Geophys. Res.*, **102**, 5733–5752, doi:10.1029/96JC02776.

Martos, P., and M. C. Piccolo, 1988: Hydrography of the Argentine continental shelf between 38° and 42°S. *Continental Shelf Research*, **8**, 1043–1056, doi:10.1016/0278-4343(88)90038-6.

Mattias Green, J. A., J. H. Simpson, S. Legg, and M. R. Palmer, 2008: Internal waves, baroclinic energy fluxes and mixing at the European shelf edge. *Continental Shelf*

Research, **28**, 937–950, doi:10.1016/j.csr.2008.01.014.

Mellor, G. L., and T. Yamada, 1982: Development of a turbulence closure model for geophysical fluid problems. *Rev. Geophys.*, **20**, 851–875, doi:10.1029/RG020i004p00851.

Moore, A. M., H. G. Arango, E. Di Lorenzo, B. D. Cornuelle, A. J. Miller, and D. J. Neilson, 2004: A comprehensive ocean prediction and analysis system based on the tangent linear and adjoint of a regional ocean model. *Ocean Modelling*, **7**, 227–258, doi:10.1016/j.ocemod.2003.11.001.

Morozov, E. G., 1995: Semidiurnal internal wave global field. *Deep Sea Research Part I: Oceanographic Research Papers*, **42**, 135–148, doi:10.1016/0967-0637(95)92886-C.

Munk, W., 1997: Once again: once again—tidal friction. *Progress in Oceanography*, **40**, 7–35, doi:10.1016/S0079-6611(97)00021-9.

——, and C. Wunsch, 1998: Abyssal recipes II: energetics of tidal and wind mixing. *Deep Sea Research Part I: Oceanographic Research Papers*, **45**, 1977–2010, doi:10.1016/S0967-0637(98)00070-3.

——, F. Snodgrass, and G. Carrier, 1956: Edge Waves on the Continental Shelf. *Science*, **123**, 127–132.

Munk, W. H., and G. J. F. MacDonald, 1975: *The rotation of the earth: a geophysical discussion.* http://adsabs.harvard.edu/abs/1975regd.book.....M (Accessed January 23, 2018).

Mysak, L. A., 1980: Topographically Trapped Waves. *Annual Review of Fluid Mechanics*, **12**, 45–76, doi:10.1146/annurev.fl.12.010180.000401.

Orlanski, I., 1976: A simple boundary condition for unbounded hyperbolic flows. *Journal of Computational Physics*, **21**, 251–269, doi:10.1016/0021-9991(76)90023-1.

Osborne, J. J., A. L. Kurapov, G. D. Egbert, and P. M. Kosro, 2011: Spatial and Temporal Variability of the M2 Internal Tide Generation and Propagation on the Oregon Shelf. *J. Phys. Oceanogr.*, **41**, 2037–2062, doi:10.1175/JPO-D-11-02.1.

Palma, E. D., R. P. Matano, and A. R. Piola, 2004: A numerical study of the Southwestern Atlantic Shelf circulation: Barotropic response to tidal and wind forcing. *J. Geophys. Res.*, **109**, C08014, doi:10.1029/2004JC002315.

——, ——, and ——, 2008: A numerical study of the Southwestern Atlantic Shelf circulation: Stratified ocean response to local and offshore forcing. *J. Geophys. Res.*, **113**, C11010, doi:10.1029/2007JC004720.

Pedlosky, J., 2003: *Waves in the Ocean and Atmosphere: Introduction to Wave Dynamics*.

2003 edition. Springer, Berlin ; New York, 264 pp.

Pingree, R. D., and A. L. New, 1989: Downward propagation of internal tidal energy into the Bay of Biscay. *Deep Sea Research Part A. Oceanographic Research Papers*, **36**, 735–758, doi:10.1016/0198-0149(89)90148-9.

——, and ——, 1995: Structure, seasonal development and sunglint spatial coherence of the internal tide on the Celtic and Armorican shelves and in the Bay of Biscay. *Deep Sea Research Part I: Oceanographic Research Papers*, **42**, 245–284, doi:10.1016/0967-0637(94)00041-P.

Pinsent, H. G., 1972: Kelvin wave attenuation along nearly straight boundaries. *Journal of Fluid Mechanics*, **53**, 273–286, doi:10.1017/S0022112072000151.

Piola, A. R., and A. L. Gordon, 1989: Intermediate waters in the southwest South Atlantic. *Deep Sea Research Part A. Oceanographic Research Papers*, **36**, 1–16, doi:10.1016/0198-0149(89)90015-0.

——, B. C. Franco, E. D. Palma, and M. Saraceno, 2013: Multiple jets in the Malvinas Current. *J. Geophys. Res. Oceans*, **118**, 2107–2117, doi:10.1002/jgrc.20170.

Ray, R. D., R. J. Eanes, and B. F. Chao, 1996: Detection of tidal dissipation in the solid Earth by satellite tracking and altimetry. *Nature*, **381**, 595, doi:10.1038/381595a0.

Rivas, A. L., and A. R. Piola, 2002: Vertical stratification at the shelf off northern Patagonia. *Continental Shelf Research*, **22**, 1549–1558, doi:10.1016/S0278-4343(02)00011-0.

——, and ——, 2011: Near inertial oscillations at the shelf off northern Patagonia. *Atlântica, Rio Grande ISSN 0102-1656, Rio Grande, Brasil*, **27**, 75–86, doi:10.5088/atlântica.v27i2.2172.

Romero, S. I., A. R. Piola, M. Charo, and C. A. E. Garcia, 2006: Chlorophyll-a variability off Patagonia based on SeaWiFS data. *J. Geophys. Res.*, **111**, C05021, doi:10.1029/2005JC003244.

Saraceno, M., C. Provost, A. R. Piola, J. Bava, and A. Gagliardini, 2004: Brazil Malvinas Frontal System as seen from 9 years of advanced very high resolution radiometer data. *J. Geophys. Res.*, **109**, C05027, doi:10.1029/2003JC002127.

Schölkopf, B., K. Tsuda, and J.-P. Vert, 2004: *Kernel Methods in Computational Biology*. MIT Press, 428 pp.

Schrama, E. J. O., and R. D. Ray, 1994: A preliminary tidal analysis of TOPEX/POSEIDON altimetry. *J. Geophys. Res.*, **99**, 24799–24808, doi:10.1029/94JC01432.

Shchepetkin, A. F., and J. C. McWilliams, 2003: A method for computing horizontal

pressure-gradient force in an oceanic model with a nonaligned vertical coordinate. *J. Geophys. Res.*, **108**, 3090, doi:10.1029/2001JC001047.

——, and ——, 2005: The regional oceanic modeling system (ROMS): a split-explicit, free-surface, topography-following-coordinate oceanic model. *Ocean Modelling*, **9**, 347–404, doi:10.1016/j.ocemod.2004.08.002.

Simmons, H. L., R. W. Hallberg, and B. K. Arbic, 2004: Internal wave generation in a global baroclinic tide model. *Deep Sea Research Part II: Topical Studies in Oceanography*, **51**, 3043–3068, doi:10.1016/j.dsr2.2004.09.015.

Sjöberg, B., and A. Stigebrandt, 1992: Computations of the geographical distribution of the energy flux to mixing processes via internal tides and the associated vertical circulation in the ocean. *Deep Sea Research Part A. Oceanographic Research Papers*, **39**, 269–291, doi:10.1016/0198-0149(92)90109-7.

Song, Y. T., and D. G. Wright, 1998: A General Pressure Gradient Formulation for Ocean Models. Part II: Energy, Momentum, and Bottom Torque Consistency. *Mon. Wea. Rev.*, **126**, 3231–3247, doi:10.1175/1520-0493(1998)126<3231:AGPGFF>2.0.CO;2.

Valla, D., and A. R. Piola, 2015: Evidence of upwelling events at the northern Patagonian shelf break. *J. Geophys. Res. Oceans*, **120**, 7635–7656, doi:10.1002/2015JC011002.

Vlasenko, V., and N. Stashchuk, 2015: Internal tides near the Celtic Sea shelf break: A new look at a well known problem. *Deep Sea Research Part I: Oceanographic Research Papers*, **103**, 24–36, doi:10.1016/j.dsr.2015.05.003.

Wang, D.-P., 1980: Diffraction of Continental Shelf Waves by Irregular Alongshore Geometry. *J. Phys. Oceanogr.*, **10**, 1187–1199, doi:10.1175/1520-0485(1980)010<1187:DOCSWB>2.0.CO;2.

Webb, D. J., 1973: On the age of the semi-diurnal tide. *Deep Sea Research and Oceanographic Abstracts*, **20**, 847–852, doi:10.1016/0011-7471(73)90006-5.

Yankovsky, A. E., 2009: Large-scale edge waves generated by hurricane landfall. *J. Geophys. Res.*, **114**, C03014, doi:10.1029/2008JC005113.

——, and T. Zhang, 2017: Scattering of a Semidiurnal Barotropic Kelvin Wave into Internal Waves over Wide Continental Shelves. *J. Phys. Oceanogr.*, **47**, 2545–2562, doi:10.1175/JPO-D-16-0284.1.

Zhang, T., and A. E. Yankovsky, 2016: On the nature of cross-isobath energy fluxes in topographically modified barotropic semidiurnal Kelvin waves. *J. Geophys. Res. Oceans*, **121**, 3058–3074, doi:10.1002/2015JC011617.

Zhao, Z., M. H. Alford, J. B. Girton, L. Rainville, and H. L. Simmons, 2016: Global

Observations of Open-Ocean Mode-1 M2 Internal Tides. *J. Phys. Oceanogr.*, **46**, 1657–1684, doi:10.1175/JPO-D-15-0105.1.

Zhao Zhongxiang, 2016: Internal tide oceanic tomography. *Geophysical Research Letters*, **43**, 9157–9164, doi:10.1002/2016GL070567.

APPENDIX A

COPYRIGHT LICENSE

JOHN WILEY AND SONS LICENSE TERMS AND CONDITIONS

Jun 27, 2018

This Agreement between University of South Carolina -- Tianyi Zhang ("You") and John Wiley and Sons ("John Wiley and Sons") consists of your license details and the terms and conditions provided by John Wiley and Sons and Copyright Clearance Center.

License Number	4353780517674
License date	May 21, 2018
Licensed Content Publisher	John Wiley and Sons
Licensed Content Publication	Journal of Geophysical Research: Oceans
Licensed Content Title	On the nature of cross-isobath energy fluxes in topographically modified barotropic semidiurnal Kelvin waves
Licensed Content Author	Tianyi Zhang, Alexander E Yankovsky
Licensed Content Date	May 13, 2016
Licensed Content Volume	121
Licensed Content Issue	5
Licensed Content Pages	17
Type of Use	Dissertation/Thesis
Requestor type	Author of this Wiley article
Format	Electronic
Portion	Full article
Will you be translating?	No
Title of your thesis / dissertation	On the Scattering of Topographically Modified Semidiurnal Kelvin Waves into Internal Waves
Expected completion date	Jun 2018
Expected size (number of pages)	150
Requestor Location	University of South Carolina 701 Sumter Street EWS 312 UNIVERSITY, SC 29208 United States Attn: University of South Carolina
Publisher Tax ID	EU826007151
Total	**0.00 USD**